Universidade de São Paulo

Instituto de Física

Nanofolhas do tipo diamante 2D funcionalizadas: propriedades físicas e potencial de aplicação em baterias de íons de metais alcalinos (Li, Na, K)

Bruno Bueno Ipaves Nascimento

Orientadora: Profa. Dra. Lucy Vitória Credidio Assali

Tese de doutorado apresentada ao Instituto de Física como requisito parcial para a obtenção do título de Doutor em Ciências

Banca Examinadora:
Profa. Dra. Lucy Vitória Credidio Assali (Orientadora) - IFSUP
Prof. Dr. Filipe Camargo Dalmatti Alves Lima - IFSP
Prof. Dr. Gustavo Martini Dalpian - UFABC
Profa. Dra. Lara Kühl Teles - ITA
Prof. Dr. Luiz Tadeu Fernandes Eleno - EEL USP

São Paulo
2023

University of São Paulo

Physics Institute

2D diamond-like functionalized nanosheets: physical properties and potential applications in alkali metal (Li, Na, K) ion batteries

Bruno Bueno Ipaves Nascimento

Supervisor: Prof. Dr. Lucy Vitória Credidio Assali

Thesis submitted to the Physics Institute of the University of São Paulo in partial fulfillment of the requirements for the degree of Doctor of Science

Examining Committee:
Prof. Dr. Lucy Vitória Credidio Assali (supervisor) - IFUSP
Prof. Dr. Filipe Camargo Dalmatti Alves Lima - IFSP
Prof. Dr. Gustavo Martini Dalpian - UFABC
Prof. Dr. Lara Kühl Teles - ITA
Prof. Dr. Luiz Tadeu Fernandes Eleno - EEL USP

São Paulo
2023

Dedicated to my mom Gislene and my dad Celso.
Dedicada à minha mãe Gislene e ao meu pai Celso.

Acknowledgements

It was not easy to finish this thesis. During my Ph.D., we faced a pandemic, I underwent a surgical procedure to treat cancer, and I also lost my father to cancer. Accordingly, firstly, I would like to say that I wrote this thesis for my mother Gislene and in memory of my father Celso, who have always been there and supported me. I have no words to thank all the love I received. Mom, I love you. Dad, I will always love you. Now, I would like to thank the people who also helped me in my Ph.D., making this thesis possible, so I would like to thank:

To my advisor Prof. Dr. Lucy Vitória Credidio Assali, for everything she taught me, for being my friend, and for helping me through the most arduous moments of my Ph.D.;

To Prof. Dr. João Francisco Justo Filho, for his collaboration, discussions, and motivation in disclosing our results, and for his friendship;

To Prof. Dr. Biplab Sanyal, for having me as a student for six months at Uppsala University, for collaboration and discussions, and to the friends I made during my stay in Sweden;

To the staff of the Department of Physics of Materials and Mechanics, especially Sandra and Rosana, and the employees of the Graduate Commission, for their support in the administrative area;

To my friends reading this thesis, from IFUSP, Cherateria, baterias universitárias, carnival, Muay Thai, Boxing, school, childhood... You were fundamental in my development and made these years of undergraduate, master, and Ph.D. more fun and unforgettable;

Agradecimentos

Não foi fácil terminar esta tese. Durante meu doutorado, enfrentamos uma pandemia, passei por uma cirurgia para tratar um câncer e também perdi meu pai para o câncer. Assim, em primeiro lugar, gostaria de dizer que escrevi esta tese para minha mãe Gislene e em memória de meu pai Celso, que sempre estiveram ao meu lado e me apoiaram. Não tenho palavras para agradecer todo o carinho que recebi. Mãe, eu te amo. Pai, eu sempre vou te amar. Agora, gostaria de agradecer às pessoas que também me ajudaram no meu doutorado, tornando esta tese possível, então gostaria de agradecer:

À minha orientadora Profa. Dra. Lucy Vitória Credidio Assali, por tudo que me ensinou, por ser minha amiga e me ajudar nos momentos mais difíceis do doutorado;

Ao Prof. Dr. João Francisco Justo Filho, pela colaboração, discussões e motivação em divulgar nossos resultados, e pela amizade;

Ao Prof. Dr. Biplab Sanyal, por me receber como aluno durante 6 meses na Universidade de Uppsala, pela colaboração e discussões, e aos amigos que fiz durante a minha estada na Suécia;

Aos funcionários do Departamento de Física dos Materiais e Mecânica, em especial à Sandra e à Rosana, e ao pessoal da Comissão de Pós-Graduação, pelo suporte na área administrativa;

Aos meus amigos e amigas que estão lendo esta tese, do IFUSP, da Cherateria, das baterias universitárias, do carnaval, do Muay Thai, do Boxe, de escola, de infância... Vocês foram fundamentais no meu desenvolvimento e fizeram esses anos de graduação, mestrado, e doutorado mais divertidos e inesquecíveis;

"Not explaining science seems to me perverse. When
you're in love, you want to tell the world"
CARL SAGAN

Abstract

In the context of the climate crisis due to human activities and the rapid increase of greenhouse gas emissions, renewable energy sources, such as solar and wind power systems, are promising solutions. Therefore, efficient technologies for storing electricity produced from these sources are essential. Among the various energy-storage devices, the lithium-ion battery (LIB) has been a leading option since entering the market in 1991. Nevertheless, it is crucial to develop rechargeable batteries beyond LIBs to meet the world's increasing demand for renewable energies. In this sense, two-dimensional (2D) materials have emerged as excellent candidates for applications in batteries. Therefore, this thesis presents an *ab-initio* investigation on the physical properties of 2D diamond-like functionalized nanosheets, performed in the framework of density functional theory. Herein, we explored the physical properties of diamond-like graphene nanosheets functionalized with nitrogen and boron atoms. Moreover, we investigated the diamond-like silicene nanosheets surface-doped with boron, nitrogen, aluminum, and phosphorus atoms. We predicted nanosheets with interesting physical properties that could possibly be applied in alkali metal ion batteries (AMIBs), van der Waals heterostructures, and ultraviolet light or thermoelectric devices. In particular, we studied and demonstrated the aluminum-functionalized silicene nanosheet is a promising candidate for AMIBs anodes, mainly for sodium and potassium ion batteries. This material remains stable up to about 600K and presents properties, such as surface diffusion barriers and specific capacity, similar to commercial anode graphite.

Keywords: DFT; 2D materials; 2D diamond-like materials; Functionalization; Battery.

Resumo

No contexto da crise climática devido às atividades humanas e ao rápido aumento das emissões de gases de efeito estufa, as fontes de energia renováveis, como os sistemas de energia solar e eólica, são soluções promissoras. Portanto, tecnologias eficientes para armazenamento da eletricidade produzida a partir dessas fontes são essenciais. Entre os vários dispositivos de armazenamento de energia, a bateria de íons de lítio (LIB) tem sido uma opção líder, desde que entrou no mercado em 1991. No entanto, é crucial desenvolver baterias recarregáveis além das LIBs para atender à crescente demanda mundial por energias renováveis. Nesse sentido, materiais bidimensionais (2D) surgiram como excelentes candidatos para aplicações em baterias. Portanto, esta tese apresenta uma investigação *ab-initio* das propriedades físicas de nanofolhas do tipo diamante 2D funcionalizadas, realizada no âmbito da teoria do funcional da densidade. Aqui, exploramos as propriedades de nanofolhas de grafeno do tipo diamante funcionalizadas com átomos de nitrogênio e boro. Além disso, investigamos as nanofolhas de siliceno do tipo diamante dopadas com átomos de boro, nitrogênio, alumínio e fósforo. Notavelmente, previmos nanofolhas com propriedades físicas interessantes e possíveis aplicações em baterias de íons de metal alcalino (AMIBs), heteroestruturas de van der Waals e dispositivos de luz UV ou termoelétricos. Em particular, estudamos e demonstramos que a nanofolha de siliceno funcionalizada com alumínio é uma promissora candidata para ânodos de AMIBs, principalmente para baterias de íons de sódio e potássio. Este material mantém-se estável até cerca de 600K e apresenta propriedades, tais como barreiras de difusão superficial e capacidade específica, semelhantes ao grafite anódico comercial.

Palavras-chave: DFT; Materiais 2D; Materiais do tipo diamante 2D; Funcionalização; Bateria.

List of papers

This thesis is based on the following papers:

I Carbon-related bilayers: nanoscale building blocks for self-assembly nanomanufacturing

Bruno Ipaves, João F Justo, and Lucy V C Assali.

The Journal of Physical Chemistry C, 123(37), 23195-23204, 2019.

DOI: 10.1021/acs.jpcc.9b05446

II Physical properties of functionalized 2D diamond

Bruno Ipaves, João F Justo, Biplab Sanyal, and Lucy V C Assali.

Manuscript in the writing stage

III Functionalized few-layer silicene nanosheets: stability, elastic, structural, and electronic properties

Bruno Ipaves, João F Justo, and Lucy V C Assali.

Physical Chemistry Chemical Physics, 24(15), 8705-8715, 2022.

DOI: 10.1039/D1CP05867C

IV Aluminum functionalized few-layer silicene as anode material for alkali metal ion batteries

Bruno Ipaves, João F Justo, and Lucy V C Assali.

Molecular Systems Design and Engineering, 8(3), 379-387, 2023.

DOI: 10.1039/D2ME00172A

List of events

The results of this thesis were presented in the following events:

1 **Theoretical investigation of graphene-like nanostructures for application in lithium ion batteries**

Bruno Ipaves, João F Justo, and Lucy V C Assali.

Work presented by **Bruno Ipaves** (Poster)

XVII Brazilian MRS Meeting (2018).

2 **Carbon-related bilayers: nanoscale building blocks for self-assembly nanomanufacturing**

Bruno Ipaves, João F Justo, and Lucy V C Assali.

Work presented by **Bruno Ipaves** (Poster)

XVIII Brazilian MRS Meeting (2019).

3 **Graphene-like structures: nanoscale building blocks for lithium-ion battery applications**

Bruno Ipaves, João F Justo, Biplab Sanyal, and Lucy V C Assali.

Work presented by **Bruno Ipaves** (Poster)

XIX Brazilian MRS Meeting (2021).

4 **Functionalized few-layer silicene nanosheets: physical properties and potential application in alkali metal ion batteries**

Bruno Ipaves, João F Justo, and Lucy V C Assali.

Work presented by **Bruno Ipaves** (Oral)

XX Brazilian MRS Meeting (2022).

Contents

1. Introduction

> I am among those who think that science
> has great beauty.

<div align="right">Marie Curie</div>

The scientific consensus is that human activities, such as deforestation, fossil fuel use, agriculture, and industry, are the primary cause of climate change [1–3]. Those activities increase the concentration of greenhouse gases in the atmosphere, notably CO_2 and CH_4, causing adverse effects on Earth, including global temperature increases, sea level rise, loss of sea ice, and melting glaciers [4]. Although there is no simple solution to tackle climate change, one possibility is to invest in energy transition toward renewable sources, such as solar and wind power systems. Nevertheless, we must search for efficient technologies for energy storage, considering those energies collected in the electrical form. In this regard, the most used energy storage device is the lithium-ion battery (LIB) [5].

The LIBs have been integrated into portable electronic devices since they entered the market in 1991 [6]. For the development of LIBs, John B. Goodenough, M. Stanley Whittingham and Akira Yoshino were awarded the Nobel Prize in Chemistry in 2019. In figure 1.1, we present the working principle of a commercial LIB in the charged state, composed of two electrodes (anode and cathode), each connected to an electric circuit and separated by an electrolyte, which transports Li-ions between the electrodes [5]. In the charging process, the electrons move from the cathode to the anode through the electric circuit. As a result, the Li-ions are transported from the cathode to the anode through the electrolyte. Upon cycling, the electrodes'
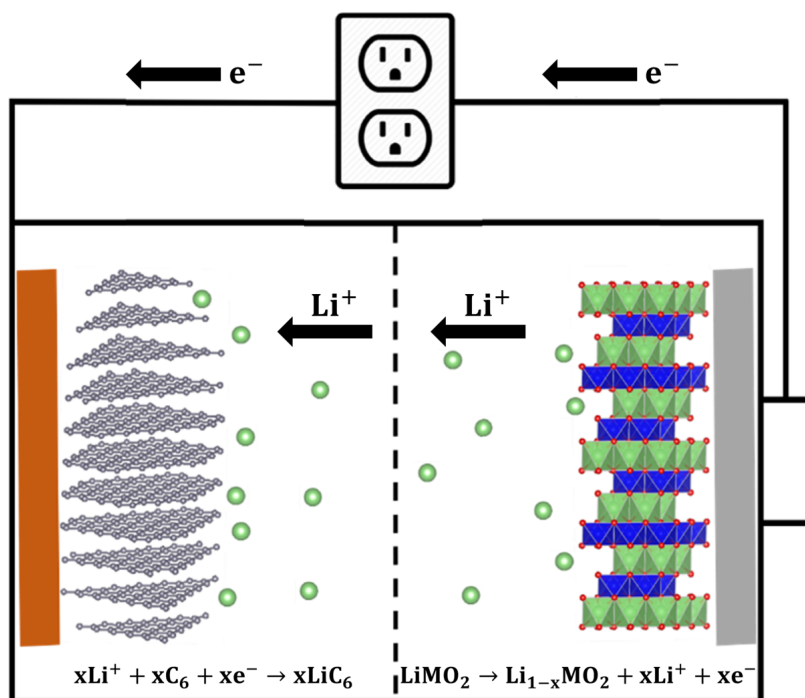
Figure 1.1: Lithium-ion battery schematic representation, composed by a graphite negative electrode (anode) with a copper current collector, a layered transition metal oxide positive electrode (cathode) with an aluminum current collector, and an organic liquid solvent with a lithium conducting salt, that is used as an electrolyte to transport Li-ions between the electrodes. During the charging process, as shown in the illustration, the Li-ions flow from the cathode to the anode, while the reversed process is the discharging. Reproduced from reference [5].

volume changes (expand and contract), and the capacity and lifetime of batteries decrease due to the reversible intercalation of ions [5, 7].

Regardless, it is essential to investigate alternative materials for batteries in order to meet the world's increasing demand for renewable energies since lithium is not an abundant chemical element on Earth and LIB presents slow charging and degradation after only a few hundred cycles when applied to large-scale systems [7, 8]. In this sense, sodium-ion (SIBs) and potassium-ion (KIBs) batteries, which present working principles similar to LIBs, are potential alternatives since the sodium (Na) and potassium (K) chemical elements are more abundant and less expensive than Li [9, 10]. The major challenge for the SIBs and KIBs, using graphite as anode

material, arises from the larger Na and K ions, as compared to Li, leading to higher diffusion barriers, higher lattice strain, and irreversible structural degradation [5]. Additionally, graphite can rarely be used as an anode material in SIBs due to a thermodynamic instability in intercalating Na-ions, and in KIBs the K-ion capacity value of 279 mAh/g by forming KC_8 is lower than the Li one of 372 mAh/g (LiC_6) in LIBs [8, 10–12]. To improve the performance of alkali metal ion batteries (AMIBs), two-dimensional (2D) materials have emerged as potential electrode candidates due to their singular properties, such as high surface activity, large surface-to-volume ratio, and elasticity [13–15].

2D materials have been widely investigated, for most diverse purposes, since the identification and manipulation of exfoliated graphene [16]. Graphene, a single layer of graphite, is the most popular two-dimensional material, which is a zero bandgap semimetal with a honeycomb carbon structure and sp^2 hybridization. It exhibits remarkable physical properties, such as high electrical conductivity, tensile strength, and optical transparency. In particular, several other nanomaterials can be built from graphene, such as fullerenes, nanotubes, graphite, and single-layer diamond (2D diamond) [16–18]. Furthermore, the 2D materials can be functionalized with several atoms and/or combined, serving as building blocks to produce 2D/3D systems [19–22]. Those systems are promising applications in several fields, including quantum computing, tunneling transistors, light-emitting diodes, and energy storage devices [7, 23, 24]. Considering developments in the synthesis and characterization of 2D materials over the last few years, showing their exciting physical phenomena and possible applications, it is of great interest to investigate and understand the properties of functionalized 2D structures.

Regarding 2D materials for application in AMIBs, silicene has emerged as a promising candidate. Silicene is a 2D hexagonal silicon monolayer similar to graphene, with a honeycomb structure and Dirac cone at the high-symmetry K-point in the first Brillouin zone [25–28]. The silicon atom is one of the most abundant on Earth, environmentally friendly, and compatible with current microelectronics devices [29, 30]. Moreover, single-layer silicene was theoretically investigated as an anode for LIBs

21

and SIBs, presenting a capacity of 954 mAh/g, which is much larger than that of graphite anode [31, 32]. Nonetheless, the application of single-layer silicene is challenging since its synthesis requires a metal substrate. On the other hand, the free-standing few-layer silicene nanosheets presented storage capacities of 721 mAh/g and 180 mAh/g for LIBs and KIBs, respectively [33, 34]. Additionally, to improve the performance of AMIB electrodes, several strategies have been investigated, such as chemical doping [35, 36].

Within the introduced context, in this work we present first-principles investigations, performed within the density functional theory (DFT) framework, of the physical properties of 2D diamond-like functionalized nanosheets and one potential application in alkali metal (Li, Na, K) ion batteries. The DFT is a successful method to describe the properties of a system composed of many electrons and nuclei. Moreover, it can be used to investigate battery materials and estimate some properties, such as open-circuit voltage and theoretical capacity. The theory and methods employed in this study are presented in Chapter 2.

Chapter 3 is dedicated to reporting the analyses of the results of the physical properties of 2D diamond-like graphene nanosheets doped with N and/or B atoms. In section 3.1, we present results reported in Paper I [21], exploring the functionalized systems made of single-layer and two-layers of graphene and discussing their potential use as nanoscale two-dimensional building blocks for the self-assembly of macroscopic structures. In section 3.2, we describe the study of systems consisting of three graphene sheets, with one non-doped graphene layer between two 50% doped ones, providing the structural, thermodynamic, mechanical, and electronic properties. At the present moment, we are investigating the potential application of those systems and the preliminary results are being reported in a writing stage manuscript (Paper II), to be published soon.

In Chapter 4, we describe the physical properties of diamond-like silicene nanosheets functionalized with boron, nitrogen, aluminum, and phosphorus atoms, explored by us in the published Paper III [28]. We explore their dynamic stability, enthalpy of formation and elastic constants, discussing possible applications. In

section 4.2, in which the results published in Paper IV [30] are reported, we carry out a theoretical investigation of aluminum functionalized silicene nanosheet and its potential application in AMIBs. Accordingly, we study the thermodynamic stability of this system as a function of temperature and calculate the average adsorption energies of Li, Na, and K atoms in several sites of the aluminum functionalized silicene nanosheet, as well as their diffusion barriers along several high-symmetry pathways. Moreover, we estimate the average open-circuit voltage and the specific theoretical capacity of the system as a possible anode material for AMIBs.

2. Theory and methods

> We should be on our guard not to
> overestimate science and scientific methods
> when it is a question of human problems.
>
> *Albert Einstein*

The materials are composed of many electrons and nuclei, and the number of interacting particles in a solid can be huge ($\geq 10^{23}$). Accordingly, to determine the properties of a system, it is essential to know the energy of the atoms and how it changes as they move around. However, due to the interaction of multiple electrons with multiple nuclei, solving the equation that describes the systems' electronic structure could be impossible [37]. One alternative is to use the density functional theory (DFT), one of the most successful methods to solve a many-body problem. Therefore, this chapter includes an overview of the DFT and the fundamental tools used in this thesis.

2.1 The many-body problem

In quantum systems, the description of atomic nuclei and electrons can be made by the non-relativistic and time-independent Schrödinger equation

$$H\Psi = E\Psi, \tag{2.1}$$

in which E is the ground-state energy of the system, Ψ is it wavefunction, and the

Hamiltonian H is represented as

$$H = - \sum_i \frac{\hbar^2}{2m_i} \nabla_i^2 - \sum_I \frac{\hbar^2}{2M_I} \nabla_I^2 +$$

$$+ \frac{e^2}{4\pi\epsilon_0} \left[\frac{1}{2} \sum_{j \neq i} \frac{1}{|\mathbf{r}_i - \mathbf{r}_j|} + \frac{1}{2} \sum_{J \neq I} \frac{Z_I Z_J}{|\mathbf{R}_I - \mathbf{R}_J|} - \sum_I \sum_i \frac{Z_I}{|\mathbf{r}_i - \mathbf{R}_I|} \right], \quad (2.2)$$

where, respectively, m_i and $\mathbf{r}_i$ denote the mass and spatial coordinates of the ith electron, while M_I and $\mathbf{R}_I$ denote the mass and spatial coordinates of the Ith nucleus. The first two terms in equation (2.2) are the kinetic energies of the electrons and ions, the third and the fourth terms represent the electron-electron and ion-ion interactions, and the last one is the Coulomb interaction between electrons and ions.

The Schrödinger equation (2.1) is a many-body problem of multiple electrons and several nuclei interacting to each other, where the complete solution is unknown even for single systems. Accordingly, we should make a first approximation, which is based on the well-known fact that atomic nuclei are much heavier than electrons and, consequently, their movements are much slower than electrons. Furthermore, considering that the ions are static and contribute by generating an external potential to the electrons, the problem of solving Schrödinger equation can be divided in a solution representing the movement of the electrons in the field of fixed nuclei and a solution representing the movement of nuclei in the potential generated by the presence of the electrons. This approach is called **Born-Oppenheimer** approximation [38] and the simplified electronic Hamiltonian is given by

$$H_{BO} = - \sum_i \frac{\hbar^2}{2m_i} \nabla_i^2 + \frac{e^2}{4\pi\epsilon_0} \frac{1}{2} \sum_{j \neq i} \frac{1}{|\mathbf{r}_i - \mathbf{r}_j|} +$$

$$- \frac{e^2}{4\pi\epsilon_0} \sum_{I \neq i} \frac{Z_I}{|\mathbf{r}_i - \mathbf{R}_I|} + \frac{e^2}{4\pi\epsilon_0} \frac{1}{2} \sum_{J \neq I} \frac{Z_I Z_J}{|\mathbf{R}_I - \mathbf{R}_J|}, \quad (2.3)$$

which does not contain the kinetic energy term of atomic nuclei, when compared to equation (2.2), and the last term is a constant for a given static position of the nuclei. Therefore, we can write this electronic Hamiltonian in atomic units (energy

in Hartree) as

$$H_e = -\frac{1}{2}\sum_i \nabla_i^2 + \frac{1}{2}\sum_{j\neq i}\frac{1}{|\mathbf{r}_i - \mathbf{r}_j|} - \sum_i\sum_I \frac{Z_I}{|\mathbf{r}_i - \mathbf{R}_I|}. \qquad (2.4)$$

Although the Born-Oppenheimer approximation simplifies the Hamiltonian H, the many-body problem remains with the electronic wavefunction containing $3N$ variables, N being the number of electrons in the system. There are approximate wavefunction-based methods for solving the electronic many-body Schrödinger equation, such as Hartree, Hartree-Fock, and post-Hartree-Fock approachs [37]. However, these methods use the wavefunction to calculate the observables, which makes their application to more complex systems difficult, mainly due to the enormous computational effort required. Therefore, we utilize the widely used density functional theory, described in the next section of this thesis.

2.2 Density functional theory (DFT)

The DFT, formally established in the mid-1960s, is based on two theorems formulated by Hohenberg and Kohn (HK) [39], as well as a set of equations developed by Kohn and Sham (KS) [40]. The DFT is a charge density-based method, i.e., the key variable is the electron density $n(\mathbf{r})$, at a particular position in space. The $n(\mathbf{r})$, unlike the traditional description based on wavefunctions with $3N$ independent variables, is a function of only three spatial coordinates and contains a great amount of information. The two HK theorems are:

1. *The ground-state energy from Schrödinger's equation is uniquely determined by the electron density.*

2. *The exact ground state electron density is the one that minimizes the total energy functional.*

According to the theorems, there is a one-to-one correspondence between the ground-state wavefunction and the ground-state electron density. In other words,

the external potential $V(\mathbf{r})$ and other properties of a system of interacting electrons is determined by the ground state electron density $n(\mathbf{r})$. Moreover, the total energy of the electronic system can be written as a functional of the exact ground state electron density, whereas the energy functional can be written

$$E[n(\mathbf{r})] = F[n(\mathbf{r})] + \int n(\mathbf{r})V(\mathbf{r})\, d\mathbf{r}, \tag{2.5}$$

where the universal functional $F[n(\mathbf{r})]$ includes the electronic kinetic energy and electron-electron repulsion terms, and it is independent of the external potential acting on the electrons.

The minimization of the $E[n(\mathbf{r})]$ depends on knowing the universal functional $F[n(\mathbf{r})]$ and the correct $n(\mathbf{r})$, restricted to the condition that the integral of $n(\mathbf{r})$ equals the total number of electrons. Although HK prove that a functional of the electron density exists and that the fundamental properties can be obtained, the form of the universal functional $F[n(\mathbf{r})]$ is unknown. KS solved this difficulty in 1965, which we describe in the next subsection.

2.2.1 The Kohn-Sham equations

KS proposed to map the problem of a system of interacting electrons onto an equivalent non-interacting problem [40]. Accordingly, the universal functional $F[n]$ has the form

$$F[n] = T[n_0] + \frac{1}{2}\int \frac{n(\mathbf{r})n(\mathbf{r'})}{|\mathbf{r} - \mathbf{r'}|} d\mathbf{r}d\mathbf{r'} + E_{XC}[n], \tag{2.6}$$

where $T[n_0]$ is the ground-state kinetic energy functional of a system of non-interacting electrons, the second term describes the Coulomb interactions between pairs of electrons, and $E_{XC}[n]$ is the *exchange-correlation energy functional*, which incorporates all the quantum mechanical effects that are not included in the other two terms of equation (2.6).

The minimization of the total energy functional with respect to the density, for this auxiliary non-interacting electrons system, leads to the one-electron KS

equations

$$\left(-\frac{1}{2}\nabla^2 + V(\mathbf{r}) + V_H(\mathbf{r}) + V_{XC}(\mathbf{r}) \right) \psi_n(\mathbf{r}) = \epsilon_n \psi_n(\mathbf{r}), \tag{2.7}$$

where $\psi_n(\mathbf{r})$ are electronic single-electron wavefunctions that depend on only three spatial variables, $V(\mathbf{r})$ is the external potential, $V_H(\mathbf{r})$ is the Hartree potential, and V_{XC} is the exchange-correlation potential. The Hartree potential is the classical electrostatic interaction (Coulomb repulsion) from the electron charge-density distribution and is defined by

$$V_H(\mathbf{r}) = \int \frac{n(\mathbf{r}')}{|\mathbf{r} - \mathbf{r}'|} d\mathbf{r}', \tag{2.8}$$

while V_{XC} is the functional derivative of the exchange-correlation energy

$$V_{XC}(\mathbf{r}) = \frac{\delta E_{XC}}{\delta n(\mathbf{r})}, \tag{2.9}$$

and the ground-state charge-density distribution is given by

$$n(\mathbf{r}) = \sum_{n=1}^{N} |\psi_n(\mathbf{r})|^2. \tag{2.10}$$

The KS equations (2.7) can be solved in a self-consistent way in the following algorithm: 1. Define an initial electron density $n(\mathbf{r})$; 2. Solve the KS equations and find the single-particle wavefunctions $\psi_n(\mathbf{r})$; 3. Calculate the new electron density $n_{KS}(\mathbf{r})$; 4. Compare $n_{KS}(\mathbf{r})$ with the initial $n(\mathbf{r})$. If $n_{KS}(\mathbf{r}) = n(\mathbf{r})$, within a pre-established criterion, this is the ground-state electron density. If $n_{KS}(\mathbf{r}) \neq n(\mathbf{r})$, within the same pre-established criterion, then the initial electron density must be updated and the process must start again from step 2.

2.2.2 Exchange-correlation functionals

We aim to find the ground-state total energy of the Schrödinger equation, which can be achieved by finding a self-consistent solution to a set of single-particle equations. However, the accuracy of the ground-state properties depends on the choice

of the exchange-correlation functional, where the explicit form is unknown, and hence we must make approximations. There are several approaches to the exchange-correlation functional, such as the Local Density Approximation (LDA) [40], the Generalized Gradient Approximation (GGA) [41], the van der Waals approximation (vdW) [42, 43], and the hybrid Heyd-Scuseria-Ernzerhof (HSE) functional [44].

Local density approximations (LDA)

In general, LDA is written as the exchange-correlation contribution of an infinitesimal volume depending only on the local density $n(\mathbf{r})$ of that volume. In other words, the $n(\mathbf{r})$ can be locally treated as the electronic density of a homogeneous electron gas

$$E_{XC}^{LDA}\left[n(\mathbf{r})\right] = \int n(\mathbf{r})\epsilon_{xc}^{hom}(n(\mathbf{r}))d\mathbf{r}, \tag{2.11}$$

where $\epsilon_{xc}^{hom}(n(\mathbf{r}))$ is a local function and is the exchange-correlation energy per particle of a uniform electron gas with density n.

The LDA has been widely used in the physics of condensed matter field and provides good results for many systems. However, the LDA approach presents low accuracy for several systems where the density homogeneity is unfavorable.

Generalized gradient approximation (GGA)

To improve the agreement with experimental results and to better describe correlated systems, we also must consider the density in neighboring volumes, i.e., consider the dependence of the exchange-correlation potential on the density gradient. This approach is called the Generalized Gradient Approximation (GGA), such as the one suggested by Perdew, Burke, and Ernzerhof (PBE) [41].

The PBE considers that the exchange-correlation contribution of an infinitesimal volume depends on the local density of that volume and includes the dependence on the gradient of the density $\nabla n(\mathbf{r})$ [41]. Therefore, the exchange-correlation energy combines a local function dependent on the electron density and on the intensity of

its gradient

$$E_{XC}^{GGA}[n(\mathbf{r})] = \int n(\mathbf{r}) \, \epsilon_{xc}(n(\mathbf{r}), \nabla n(\mathbf{r})) d\mathbf{r}. \tag{2.12}$$

Although the LDA and GGA exchange-correlation functionals provide good results, they poorly describe non-local effects, such as the van der Waals (vdW) interactions [45]. Since we are working with 2D materials, vertical heterostructures, and the adsorption of atoms, we must consider the vdW interactions in our calculations.

van der Waals approximation (vdW)

In this thesis, we used the van der Waals approximation with the Dion *et al.* scheme [42] optimized by Klimeš *et al.* (optB88-vdW) [43]. To include the vdW forces, the exchange-correlation energy is rewritten as

$$E_{XC} = E_X^{GGA} + E_C^{LDA} + E_C^{nl}. \tag{2.13}$$

The first two terms are semi-local, where the exchange energy E_X^{GGA} uses the Becke88 functional [46] that was optimized by Klimeš *et al.* [43], and the correlation energy E_C^{LDA} uses the LDA [45, 47]. The non-local term E_C^{nl} is given by

$$E_C^{nl} = \frac{1}{2} \iint n(\mathbf{r}) \Phi(\mathbf{r}, \mathbf{r}') n(\mathbf{r}') d\mathbf{r} d\mathbf{r}', \tag{2.14}$$

where $\Phi(\mathbf{r}, \mathbf{r}')$ depends on the electron density n, its derivative ∇n, and the inter-electronic distance $|\mathbf{r} - \mathbf{r}'|$ [43, 45, 47].

Hybrid Heyd-Scuseria-Ernzerhof (HSE) functional

Due to a strong delocalization of electrons, the DFT generally underestimates gap values with respect to the experiment. Accordingly, the hybrid Heyd-Scuseria-Ernzerhof (HSE) functional can be used to accurately predict the energy band gaps [44, 48].

The HSE functional is a range-separated hybrid functional as it uses the Coulomb potential screened by an error function to define short-range (SR) and long-range (LR) interactions:

$$\frac{1}{r} = SR + LR = \frac{1 - erf(\omega r)}{r} + \frac{erf(\omega r)}{r}. \qquad (2.15)$$

The exchange-correlation energy is calculated as

$$E_{XC}^{HSE} = \alpha E_X^{HF,SR}(\omega) + (1 - \alpha)E_X^{PBE,SR}(\omega) + E_X^{PBE,LR}(\omega) + E_C^{PBE}, \qquad (2.16)$$

where $E_X^{HF,SR}$ is the SR Hartree-Fock exchange energy, $E_X^{PBE,SR}$ and $E_X^{PBE,LR}$ are, respectively, the SR and LR PBE exchange terms, and E_C^{PBE} is the PBE correlation energy. The Hartree-Fock mixing constant parameter α is 0.25 and the screening parameter ω is ≈ 0.106 for Hartree-Fock term and ≈ 0.189 for the PBE part [44,48].

2.2.3   Projector augmented wave (PAW) method

In 1994, Peter E. Blöchl developed the Projector Augmented Wave (PAW) method [49], which is a generalization of the pseudopotential [50] and Linearized Augmented Plane Wave (LAPW) [51] approach. In this thesis, the DFT calculations are performed based on the PAW method implemented by Kresse and Joubert [52].

The PAW is an all-electron method that divides the total electronic wavefunction in terms of a localized contribution, that varies rapidly in the ionic region (core) and a smooth wavefunction in the remaining crystalline region. Accordingly, the PAW turns the total wavefunction $|\Psi\rangle$ into a smooth and computationally suitable one: the auxiliary wavefunction $|\tilde{\Psi}\rangle$, that is recovered through a linear transformation τ

$$|\Psi\rangle = \tau|\tilde{\Psi}\rangle, \qquad (2.17)$$

in which the transformation τ is given by

$$\tau = 1 + \sum_R \tau_R, \qquad (2.18)$$

where R is the atomic site and τ_R is a local linear transformation operator, acting only within some augmented region (core) around an atom, i.e., τ_R is always zero outside that region. Therefore, we can treat core wavefunctions separately as they do

not spread to neighboring atoms. Each pseudo-wavefunction $|\tilde{\Psi}\rangle$ will be expanded into partial wavefunctions $|\tilde{\phi}_i\rangle$

$$|\tilde{\Psi}\rangle = \sum_{i \in R} c_i |\tilde{\phi}_i\rangle, \tag{2.19}$$

where the index i refers to the atomic site R and c_i are expansion coefficients. Accordingly, considering that the region of oscillations is delimited by spheres of radius r_c centered on each atom, and that the auxiliary partial wavefunctions $|\tilde{\phi}_i\rangle$ are linear transformations of smooth partial waves $|\phi_i\rangle$ given by

$$|\phi_i\rangle = (1 + \tau_R)|\tilde{\phi}_i\rangle \quad \text{for} \quad i \in R, \tag{2.20}$$

it follows that the τ_R vanishes for $|\mathbf{r} - \mathbf{R}| > r_c$, i.e.,

$$\phi_i(\mathbf{r}) \equiv \tilde{\phi}_i(\mathbf{r}) \quad \text{if} \quad i \in R \quad \text{and} \quad |\mathbf{r} - \mathbf{R}| > r_c, \tag{2.21}$$

while for $|\mathbf{r} - \mathbf{R}| < r_c$

$$|\tilde{\Psi}(\mathbf{r})\rangle = \sum_i |\tilde{\phi}_i(\mathbf{r})\rangle \langle \tilde{p}_i |\tilde{\Psi}(\mathbf{r})\rangle, \tag{2.22}$$

where the projected wavefunctions $|\tilde{p}_i\rangle$ satisfies the completeness and the orthonormality relations

$$\sum_i |\tilde{\phi}_i\rangle \langle \tilde{p}_i| = 1 \quad \text{and} \quad \langle \tilde{p}_i |\tilde{\phi}_j\rangle = \delta_{ij}. \tag{2.23}$$

The total valence electron wavefunction $|\Psi\rangle$ is obtained by using

$$|\Psi\rangle = |\tilde{\Psi}\rangle + \sum_i (|\phi_i\rangle - |\tilde{\phi}_i\rangle)\langle \tilde{p}_i |\tilde{\Psi}\rangle. \tag{2.24}$$

In summary, the PAW method writes the total valence wavefunction Ψ in terms of three components

$$|\Psi\rangle = |\tilde{\Psi}\rangle + |\Psi^1\rangle - |\tilde{\Psi}^1\rangle, \tag{2.25}$$

where $|\tilde{\Psi}\rangle$ is smooth throughout the crystalline region, being accurate outside the augmented region ($|\mathbf{r} - \mathbf{R}| > r_c$); $|\Psi^1\rangle$ is accurate in the augmented region ($|\mathbf{r} - \mathbf{R}| < r_c$), incorporating the entire nodal structure of the exact wavefunction, and

is a smooth function, tending to zero in the region outside the augmented region (interstitial region); and $|\tilde{\Psi}^1\rangle$ is smooth throughout the region, being identical to $|\tilde{\Psi}\rangle$ in the augmented region and to $|\Psi^1\rangle$ in the interstitial region.

Figure 2.1 presents the bonding p-σ orbital of the Cl_2 molecule obtained by the PAW method [53], illustrating the behavior of each of the three wavefunctions that make up the all-electron (AE) total valence wavefunction.
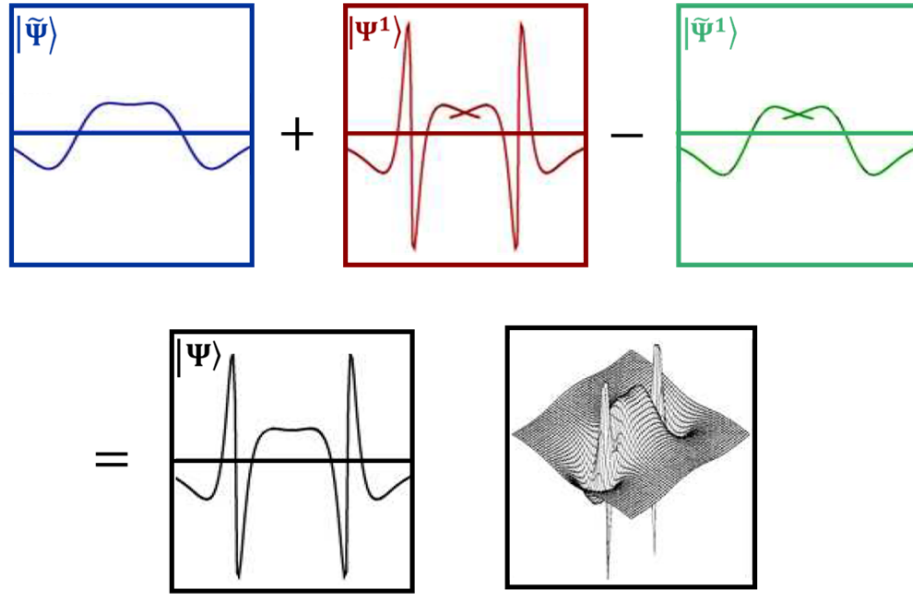
Figure 2.1: Representation of the three valence wavefunctions that make up the AE wavefunction in the PAW method, where $|\Psi\rangle = |\tilde{\Psi}\rangle + |\Psi^1\rangle - |\tilde{\Psi}^1\rangle$. Figure adapted from reference [53].

The core states $|\Psi\rangle^c$ are also decomposed in terms of three components

$$|\Psi\rangle^c = |\tilde{\Psi}\rangle^c + |\phi\rangle^c - |\tilde{\phi}\rangle^c, \tag{2.26}$$

where $|\tilde{\Psi}\rangle^c$ is a core pseudo-wavefunction, identical to the true states outside the augmented region, with a smooth continuation inside; $|\phi\rangle^c$ is a partial AE wave function identical to the core states, expressed as radial functions multiplied by spherical harmonics; and a partial core pseudo-wave identical to the pseudo-state

$|\tilde{\phi}^c\rangle$, which is also represented as radial functions multiplied by spherical harmonics.

2.3 Density functional perturbation theory

Several physical properties, such as structural stability, superconductivity, and thermal and electrical conductivity, depend on the quantum mechanical description of lattice vibrations. Herein, the vibrational-normal modes (phonons) of the systems were computed by the phonon dispersion dynamic matrix by using the density functional perturbation theory (DFPT) that is presented in this section and described in detail in the following references: [54–56].

To determine the lattice-dynamical properties of a system, we first use the Born-Oppenheimer approximation (section 2.1), which allows decoupling the vibrational from the electronic degrees of freedom in a solid. Accordingly, the Schrödinger equation that describes the nuclei motion is given by

$$\left(-\frac{1}{2} \sum_I \frac{1}{M_I} \frac{\partial^2}{\partial \mathbf{R}_I^2} + E(\mathbf{R}) \right) \phi(\mathbf{R}) = \mathcal{E}\phi(\mathbf{R}), \qquad (2.27)$$

where $\mathcal{E}$ are the eigenvalues and ϕ are the eigenfunctions. $\mathbf{R}_I$ and M_I are the spatial coordinates and the mass of the Ith nucleus, respectively. $E(\mathbf{R})$ is the *Born-Oppenheimer energy surface*, i.e., the ground-state energy of a system, whose interacting electrons are moving in the field of fixed nuclei.

The equilibrium geometry of a system occurs when the forces acting on an individual nucleus vanish ($\mathbf{F}_I = 0$),

$$\mathbf{F}_I \equiv -\frac{\partial E(\mathbf{R})}{\partial \mathbf{R}_I} = 0, \qquad (2.28)$$

and the phonon frequencies ω are obtained solving the following eigenvalue problem

$$\det \left| \frac{1}{\sqrt{M_I M_J}} \frac{\partial^2 E(\mathbf{R})}{\partial \mathbf{R}_I \mathbf{R}_J} - \omega^2 \right| = 0. \qquad (2.29)$$

The equilibrium geometry and the phonon frequencies depend on the first and

second derivatives of the Born-Oppenheimer energy surface ($E(\mathbf{R})$), respectively. We can compute both using the Hellmann-Feynman theorem

$$\mathbf{F}_I = -\int n_{\mathbf{R}}(\mathbf{r}) \frac{\partial V_{\mathbf{R}}(\mathbf{r})}{\partial \mathbf{R}_I} d\mathbf{r} - \frac{\partial E_N(\mathbf{R})}{\partial \mathbf{R}_I}; \quad \text{and} \tag{2.30}$$

$$\frac{\partial^2 E(\mathbf{R})}{\partial \mathbf{R}_I \mathbf{R}_J} \equiv -\frac{\partial \mathbf{F}_I}{\partial \mathbf{R}_J} = \int \frac{\partial n_{\mathbf{R}}(\mathbf{r})}{\partial \mathbf{R}_J} \frac{\partial V_{\mathbf{R}}(\mathbf{r})}{\partial \mathbf{R}_I} d\mathbf{r} + \int n_{\mathbf{R}}(\mathbf{r}) \frac{\partial^2 V_{\mathbf{R}}(\mathbf{r})}{\partial \mathbf{R}_I \partial \mathbf{R}_J} d\mathbf{r} + \frac{\partial^2 E_N(\mathbf{R})}{\partial \mathbf{R}_I \partial \mathbf{R}_J}, \tag{2.31}$$

where $V_{\mathbf{R}}(\mathbf{r})$ is the electron-nucleus interaction, $E_N(\mathbf{R})$ is the electrostatic interaction between different nuclei, and $n_{\mathbf{R}}(\mathbf{r})$ is the ground-state electron charge density.

2.3.1 Linear response

To solve equations (2.29) and (2.30), we can calculate the $n_{\mathbf{R}}(\mathbf{r})$ and its linear response to a distortion of the nuclear geometry ($\partial n_{\mathbf{R}}(\mathbf{r})/\partial \mathbf{R}_I$) within DFT and DFPT. The wavefunctions and the ground state electronic energy of a crystal are determined by solving the following set of KS one-electron equations

$$H_{KS}\psi_n(\mathbf{r}) = \left(-\frac{1}{2}\nabla_i^2 + V_{KS}(\mathbf{r})\right)\psi_n(\mathbf{r}) = \epsilon_n\psi_n(\mathbf{r}), \tag{2.32}$$

$$V_{KS}(\mathbf{r}) = V(\mathbf{r}) + \int \frac{n(\mathbf{r}')}{|\mathbf{r}-\mathbf{r}'|} d\mathbf{r}' + \frac{\delta E_{XC}}{\delta n(\mathbf{r})}, \tag{2.33}$$

$$n(\mathbf{r}) = \sum_{n=1}^{N} |\psi_n(\mathbf{r})|^2. \tag{2.34}$$

For phonon calculations, we need to linearize these three mentioned equations. Accordingly, we consider a perturbation on external potential $V \to \Delta V(\mathbf{r})$ and use first-order perturbation theory to obtain the variation of the KS orbitals $\psi_n(\mathbf{r}) \to \Delta\psi_n(\mathbf{r})$ and the electron charge-density response $n(\mathbf{r}) \to \Delta n(\mathbf{r})$. Therefore, we write

the self-consistent set of linear equations as

$$\left(H_{KS} - \epsilon_n\right)\left|\Delta\psi_n\right\rangle = -\left(\Delta V_{KS} - \Delta\epsilon_n\right)\left|\psi_n\right\rangle, \tag{2.35}$$

$$\Delta V_{KS}(\mathbf{r}) = \Delta V(\mathbf{r}) + \int \frac{\Delta n(\mathbf{r}')}{|\mathbf{r} - \mathbf{r}'|}d\mathbf{r}' + \Delta n(\mathbf{r})\left[\frac{d}{dn}\left(\frac{\delta E_{XC}}{\delta n(\mathbf{r})}\right)\right]_{n=n(\mathbf{r})}, \tag{2.36}$$

$$\Delta n(\mathbf{r}) = 2\ \mathrm{Re}\sum_{\mathrm{n}=1}^{\mathrm{N}} \psi_{\mathrm{n}}^*(\mathbf{r})\Delta\psi_{\mathrm{n}}(\mathbf{r}), \tag{2.37}$$

where $\Delta\epsilon_n = \left\langle\psi_n|\Delta V_{KS}|\psi_n\right\rangle$ is the first-order variation of the KS eigenvalue ϵ_n.

2.3.2 Monochromatic perturbations

To make equation (2.35) non-singular, we can introduce the projector onto the empty-state manifold P_c and a multiple of the projector onto the occupied-state manifold P_v

$$\left(H_{KS} + \alpha P_v - \epsilon_n\right)\left|\Delta\psi_n\right\rangle = -P_c\,\Delta V_{KS}\left|\psi_n\right\rangle. \tag{2.38}$$

Moreover, the responses to perturbations of different wavelengths are decoupled, which allows the calculation of phonon frequencies at arbitrary wave vectors $\mathbf{q}$ and avoid the use of supercells. Therefore, we can rewrite the last equation using translational invariance $P^{\mathbf{k+q}}P_v = P_v^{\mathbf{k+q}}$ and $P^{\mathbf{k+q}}P_c = P_c^{\mathbf{k+q}}$, i.e.,

$$\left(H_{KS} + \alpha P_v^{\mathbf{k+q}} - \epsilon_v^{\mathbf{k}}\right)\left|\Delta\psi_v^{\mathbf{k+q}}\right\rangle = -P_c^{\mathbf{k+q}}\,\Delta V_{KS}\left|\psi_v^{\mathbf{k}}\right\rangle, \tag{2.39}$$

where $\mathbf{k}$ is the wavevector, $\psi_v^{\mathbf{k}}$ is the unperturbed wavefunction, and $\left|\Delta\psi_v^{\mathbf{k+q}}\right\rangle = P^{\mathbf{k+q}}\left|\psi_v^{\mathbf{k}}\right\rangle$. Taking into account that the Fourier components of any real function with wavevectors $\mathbf{q}$ and $\mathbf{-q}$ are complex conjugates of each other, we can write a set of self-consistent linear response to a perturbation of a wavevector $\mathbf{q}$:

$$\left(H_{KS}^{\mathbf{k+q}} + \alpha\sum_{v'}\left|u_{v'}^{\mathbf{k+q}}\right\rangle\left\langle u_{v'}^{\mathbf{k+q}}\right| - \epsilon_v^{\mathbf{k}}\right)\left|\Delta u_v^{\mathbf{k+q}}\right\rangle =$$
$$-\left[1 - \sum_{v'}\left|u_{v'}^{\mathbf{k+q}}\right\rangle\left\langle u_{v'}^{\mathbf{k+q}}\right|\right]\Delta v_{KS}^{\mathbf{q}}\left|u_v^{\mathbf{k}}\right\rangle, \tag{2.40}$$

$$\Delta v_{KS}^{\mathbf{q}}(\mathbf{r}) = \Delta v^{\mathbf{q}}(\mathbf{r}) + \int \frac{\Delta n^{\mathbf{q}}(\mathbf{r}')}{|\mathbf{r} - \mathbf{r}'|} e^{-i\mathbf{q}\cdot(\mathbf{r}-\mathbf{r}')} d\mathbf{r}' +$$
$$+ \Delta n^{\mathbf{q}}(\mathbf{r}) \left[\frac{d}{dn} \left(\frac{\delta E_{XC}}{\delta n(\mathbf{r})} \right) \right]_{n=n(\mathbf{r})}, \tag{2.41}$$

$$\Delta n_v^{\mathbf{q}}(\mathbf{r}) = 2 \sum_{\mathbf{k}v} u_v^{\mathbf{k}*}(\mathbf{r}) \Delta u_v^{\mathbf{k}+\mathbf{q}}(\mathbf{r}), \tag{2.42}$$

where $u_v^{\mathbf{k}}$ are the periodic parts of the unperturbed wavefunction, $\Delta u_v^{\mathbf{k}+\mathbf{q}}$ are the Fourier component of the first-order correction, and v' runs over the occupied states at $\mathbf{k} + \mathbf{q}$.

2.3.3 Phonons in crystalline solids

In crystalline solids, phonon frequencies $\omega(\mathbf{q})$ are solutions of the secular equation

$$\det \left| \frac{1}{\sqrt{M_s M_{s'}}} \tilde{C}_{ss'}^{\alpha\beta}(\mathbf{q}) - \omega^2(\mathbf{q}) \right| = 0, \tag{2.43}$$

where $\tilde{C}_{ss'}^{\alpha\beta}(\mathbf{q})$ is the second derivative of the Born-Oppenheimer energy surface:

$$\tilde{C}_{ss'}^{\alpha\beta}(\mathbf{q}) = \frac{1}{N_c} \frac{\partial^2 E}{\partial u_s^{*\alpha}(\mathbf{q}) \partial u_{s'}^{\beta}(\mathbf{q})}. \tag{2.44}$$

Herein, the index I appearing in equation (2.29) is now defined by the positions of the atom within the unit cell, $\alpha(\beta)$ represents Cartesian components, $s(s')$ indicates the sth$(s'$th) atom of the unit cell, N_c is the number of unit cells in the crystal, and the vector $\mathbf{u}_s(\mathbf{q})$ is given by the distortion

$$\mathbf{R}_I\left[\mathbf{u}_s(\mathbf{q})\right] = \mathbf{R} + \tau_s + \mathbf{u}_s(\mathbf{q})e^{i\mathbf{q}\cdot\mathbf{R}}, \tag{2.45}$$

where $\mathbf{R}$ is the position of a given unit cell in the Bravais lattice and τ_s is the equilibrium position of the atom in the unit cell. Therefore, the dynamical matrix

related to the interatomic force constants via Fourier transform is

$$\tilde{D}_{ss'}^{\alpha\beta}(\mathbf{q}) = \frac{1}{\sqrt{M_s M_{s'}}} \sum_{\mathbf{R}\mathbf{R'}} \frac{\partial^2 E}{\partial u_s^{*\alpha}(\mathbf{R}) \partial u_{s'}^{\beta}(\mathbf{R'})} e^{-i\mathbf{q}\cdot(\mathbf{R'}-\mathbf{R})}, \qquad (2.46)$$

and the phonon frequencies are

$$\omega^2(\mathbf{q}) u_s^{\alpha}(\mathbf{q}) = \sum_{\beta s'} u_{s'}^{\beta}(\mathbf{q}) \tilde{D}_{ss'}^{\alpha\beta}(\mathbf{q}). \qquad (2.47)$$

In this thesis, we used the phonon theory to study the dynamical stability of the structures. The system is dynamically stable if all phonon modes have positive frequencies for all wavevectors in the first Brillouin zone.

2.4 Strain-energy method

In the previous section, we presented the phonon theory that allows for studying the dynamical stability of the systems in the DFT framework. To improve the results regarding crystalline structure stability, we also investigated the elastic stability of the structures with the method presented in this section. Herein, we computed the elastic properties of the systems using the strain-energy method, described in detail in the following references: [57, 58].

For small deformations (ϵ) near the equilibrium positions, the elastic energy equation of a 2D crystal has the following form

$$E(\epsilon) = E(0) + \frac{1}{2} E^{(2)} \epsilon^2 + \mathcal{O}(\epsilon^3), \qquad (2.48)$$

where $E(\epsilon)$ and $E(0)$ are the total energies of strained and unstrained configurations, respectively, and the expansion coefficient $E^{(2)}$ allows to obtain the elastic constants after fitting a second-order polynomial to the data.

We should apply in-plane deformations to obtain all the relevant elastic constants for a 2D material. For isotropic structures, we employ only two in-plane strains: the axial deformation along the zigzag direction and the hydrostatic planar deformation. Consequently, $E^{(2)} = C_{11}$ is the elastic constant for a zigzag axial deformation and

$E^{(2)} = 2(C_{11} + C_{12})$ is the expression for a biaxial planar deformation. On the other hand, for anisotropic systems, we should apply, besides the ones already described, two more in-plane strains: the axial deformation along the armchair direction and the shear deformation. Accordingly, we obtain the four independent elastic constants by fitting a second-order polynomial to the data. Therefore, $E^{(2)} = C_{11}$ is, again, the elastic constant for a zigzag axial deformation, $E^{(2)} = C_{11} + C_{22} + 2C_{12}$ is the expression for a biaxial planar deformation, $E^{(2)} = C_{22}$ is for an armchair axial deformation, and $E^{(2)} = 4C_{44}$ is for shear deformation.

Using the calculated elastic constants, we can investigate the elastic stability of the 2D anisotropic systems by obtaining the Young modulus (Y^{2D}) and the Poisson ratio (ν). Moreover, according to the Born criteria, a mechanically stable 2D systems must satisfy $C_{11}C_{22} - C_{12}^2 > 0$ and $C_{44} > 0$.

The Young modulus Y^{2D}, which is the ratio between the applied traction and the longitudinal extension, is obtained as

$$Y^{2D} = \frac{C_{11}C_{22} - C_{12}^2}{C_{11}\sin^4\theta + C_{22}\cos^4\theta + \left(\dfrac{C_{11}C_{22} - C_{12}^2}{C_{44}} - 2C_{12}\right)\cos^2\theta\sin^2\theta}, \qquad (2.49)$$

where θ is the angle between the zigzag direction and an arbitrary direction giving by $\mathbf{n} = \cos\theta\,\mathbf{e}_x + \sin\theta\,\mathbf{e}_y$, $\mathbf{e}_x$ and $\mathbf{e}_y$ being the unit vectors along the zigzag and the armchair directions, respectively.

The Poisson ratio ν, which is the ratio between the lateral contraction and the longitudinal extension, is obtained as

$$\nu = -\frac{\left(C_{11} + C_{22} - \dfrac{C_{11}C_{22} - C_{12}^2}{C_{44}}\right)\cos^2\theta\sin^2\theta - C_{12}(\cos^4\theta + \sin^4\theta)}{C_{11}\sin^4\theta + C_{22}\cos^4\theta + \left(\dfrac{C_{11}C_{22} - C_{12}^2}{C_{44}} - 2C_{12}\right)\cos^2\theta\sin^2\theta}. \qquad (2.50)$$

For isotropic 2D systems the mechanical stability is given by $C_{11} > C_{12}$, since the linear elastic constants obey the relations $C_{11} = C_{22}$ and $2C_{44} = C_{11} - C_{12}$. Consequently, the Young modulus is reduced to $Y^{2D} = \left(C_{11}^2 - C_{12}^2\right)/C_{11}$ and the Poisson ratio to $\nu = C_{12}/C_{11}$.

2.5   Enthalpy of formation

To investigate the thermal stability of the structures, we can use the enthalpy of formation [59–61]. The standard enthalpy of formation, ΔH_f^0, of a certain compound is given by

$$\Delta H_f^0 = E_t - \sum_i n_i \mathcal{E}_i, \tag{2.51}$$

where E_t is the total energy of the compound, $\mathcal{E}_i$ is the total energy of element i in its standard state, and n_i is the number of elements i.

Within this definition, a negative ΔH_f^0 indicates the amount of energy for breaking bonds of an element i is smaller than the amount of energy released when making the compound bonds (exothermic reaction). Accordingly, $\Delta H_f^0 < 0$ is a necessary but not sufficient condition for thermodynamic stability, meaning that the system is stable or metastable. Nevertheless, we find some 2D synthesized materials with $\Delta H_f^0 > 0$ (endothermic reaction) due to uncertainty on the DFT energies, substrate interactions, and other external effects.

2.6   Molecular dynamics

In this section, we present the basic idea of molecular dynamics (MD) that is a method to investigate the trajectories of moving atoms [37,62,63]. In this thesis, we performed *ab-initio* molecular dynamics (AIMD) simulations with a Nose-Hoover thermostat (NVT ensemble) to evaluate the thermal stability of some structures, as implemented in the Vienna *ab-initio* simulation package (VASP) [64].

2.6.1 Classical molecular dynamics

In the classical MD, we consider that N atoms in a volume V are described by the total kinetic energy (K) and the total potential energy (U), which are given by

$$K \quad = \quad \frac{1}{2}\sum_{i=1}^{3N} m_i v_i^2\,; \tag{2.52}$$

$$U \quad = \quad \sum_{i=1}^{3N} U(r_i), \tag{2.53}$$

where v_i, m_i, and r_i are the velocity, the mass, and the position of the ith atom. Herein, the atoms are moving within the framework of classical mechanics and the equations of motion can be defined in terms of the Lagrangian (L) of the system:

$$\frac{d}{dt}\left(\frac{\partial L}{\partial v_i}\right) - \frac{\partial L}{\partial r_i} = 0, \tag{2.54}$$

where L is given in terms of the kinetic and potential energies

$$L = \frac{1}{2}\sum_{i=1}^{3N} m_i v_i^2 - \sum_{i=1}^{3N} U(r_i). \tag{2.55}$$

2.6.2 *Ab-initio* molecular dynamics (AIMD)

The primary difference between classical molecular dynamics and *ab-initio* molecular dynamics is how we obtain the potential energy $U(r_1, ..., r_{3N})$. In this thesis, we used Born-Oppenheimer molecular dynamics (BOMD) based on DFT, where the Lagrangian is given by

$$L = K - U = \frac{1}{2}\sum_{i}^{3N} m_i v_i^2 - E\left[\varphi\left(r_1, ..., r_{3N}\right)\right], \tag{2.56}$$

where $\varphi\left(r_1, ..., r_{3N}\right)$ is the Kohn-Sham wavefunctions, as discussed in section 2.2. In this BOMD approach, the nuclei move classically on the BO potential-energy surface (see section 2.1 for details) and, hence, we used the Hellman-Feynman theorem to

compute the force in each atom of the system

$$F_i = -\left\langle \varphi_0 \left| \frac{\partial H_e}{\partial r_i} \right| \varphi_0 \right\rangle \tag{2.57}$$

where φ_0 is the ground-state wavefunction and H_e is the electronic Hamiltonian as defined in section 2.1. Accordingly, the equations of motions are

$$m_i \frac{dr_i^2}{dt^2} = -\left\langle \varphi_0 \left| \frac{\partial H_e}{\partial r_i} \right| \varphi_0 \right\rangle; \tag{2.58}$$

$$E_0 \varphi_0 = H_e \varphi_0. \tag{2.59}$$

Herein, using an interactive method, the electronic information from a previous MD step is used to update the momenta and atomic positions and then compute the energy and forces for a new time step.

2.6.3   Nose-Hoover thermostat

The *canonical ensemble* is defined by a constant number of particles, volume, and temperature (NVT ensemble). In this situation, the velocities follow the Maxwell-Boltzmann distribution and the average kinetic energy is

$$\overline{K} = \frac{3}{2} N k_B T, \tag{2.60}$$

where k_B is the Boltzmann constant. In order to simulate the NVT ensemble, we used the method developed by Nosé and Hoover [62,65–67], in which the Lagrangian has a fictitious coordinate s for the heat bath:

$$L = \frac{1}{2} \sum_{i=1}^{3N} m_i s^2 v_i^2 - \sum_{i=1}^{3N} U(r_i) + \frac{Q}{2} \left(\frac{ds}{dt} \right)^2 - g k_B T \ln(s) \tag{2.61}$$

where the third and fourth terms are the kinetic and potential energies, respectively, of the fictitious coordinate s, Q being an effective "mass" of s and g the number of degrees of freedom of the system.

2.7 Equilibrium voltage

We can use DFT to obtain some battery properties, such as voltage and theoretical capacity, which is described in the following references: [68, 69]. The equilibrium voltage of an alkali-metal M (M = Li, Na, K) ion battery is proportional to the difference in the chemical potential values of the metal M when incorporated to the anode, $\mu_{\text{M}}^{\text{anode}}$, or to the cathode, $\mu_{\text{M}}^{\text{cathode}}$, which is given by the following Nernst equation

$$V = -\frac{\mu_{\text{M}}^{\text{cathode}} - \mu_{\text{M}}^{\text{anode}}}{ze}, \tag{2.62}$$

where e is the electron's charge and z is the M oxidation state ($z = 1$ for Li, Na and K). The average voltage $\overline{V}$ during the ion intercalation process can be written in terms of the Gibbs free energy G_f

$$\overline{V} = -\frac{\Delta G_f}{ne}, \tag{2.63}$$

where the change in Gibbs free energy during the adsorption process is defined as

$$\Delta G_f = \Delta E_f + P\Delta V_f - T\Delta S_f. \tag{2.64}$$

Since $P\Delta V_f \approx 10^{-5}$ eV and $T\Delta S_f \approx 26$ meV at room temperature, the $P\Delta V_f$ and $T\Delta S_f$ terms can be neglected and, under these circumstances, ΔG_f is approximately equal to the adsorption energy ΔE_f involved in the process, i.e.,

$$\Delta G_f \approx \Delta E_f(\text{M}) = \left[E_t\big(\text{HM}_n\big) - E_t(\text{H}) - nE_t(\text{M})\right]\Big/n, \tag{2.65}$$

where $E_t\big(\text{HM}_n\big)$ is the total DFT energy of the host with nM alkali-metal adatoms, $E_t(\text{H})$ is the total DFT energy of the host material, and $E_t\big(\text{M}\big)$ is the total DFT energy, per atom, of the alkali-metal M in its standard ground state.

The theoretical capacity C, which is the maximum amount of ions that can be stored in the host, can be obtained using the formula

$$C = \frac{n_{max} \times z \times \text{F} \times 10^3}{A_{\text{H}}}, \tag{2.66}$$

where F = 26.810 Ah/mol is the Faraday constant, n_{max} is the maximum number of M alkali adatoms that the host can store, and A_H is the atomic mass of the host.

2.8 Nudged elastic band (NEB) method

Diffusion event is a relevant problem in condensed matter physics and theoretical chemistry. This kind of problem needs to identify how the position of a group of atoms changes between two stable configurations. In this thesis, to investigate the intercalation process of the ions in electrode materials, we used the Nudged Elastic Band (NEB) method [37] to find the minimum energy pathway (MEP) between an initial and a final configuration. This method was developed by H. Jónsson *et al.* [70, 71], and implemented in Quantum Espresso [72, 73].

The NEB method defines a set of $N-1$ intermediate images, that are geometric configurations of the system, at $\mathbf{R}_0, \cdots, \mathbf{R}_N$ positions, assuming each image connected through spring, where $\mathbf{R}_0$ and $\mathbf{R}_N$ are the initial and the final states of the MEP, respectively. Accordingly, we fixed the initial and the final images and optimize the positions of the remaining ones, in which the quasi-Newton Broyden's second method was the optimization algorithm applied in Quantum Espresso to relax the images down towards the MEP. In the NEB method, the force acting on each image, $\mathbf{F}_i^{\mathrm{NEB}}$, contains two components: the one that is the parallel component of the spring force, $\mathbf{F}_i^{S\|}$, and the one that is the perpendicular component of the true force, $\mathbf{F}_i^\perp = -\nabla E\left(\mathbf{R}_i\right)\big|_\perp$. Figure 2.2 illustrates the $\mathbf{F}_i^{\mathrm{NEB}}$, which is given by the following equation

$$\mathbf{F}_i^{\mathrm{NEB}} = \mathbf{F}_i^{S\|} - \nabla E\left(\mathbf{R}_i\right)\Big|_\perp, \tag{2.67}$$

where the projections are expressed by

$$\mathbf{F}_i^{S\|} = \kappa\Big(\big|\mathbf{R}_{i+i} - \mathbf{R}_i\big| - \big|\mathbf{R}_i - \mathbf{R}_{i-1}\big|\Big)\hat{\tau}_i\,; \tag{2.68}$$

$$\nabla E\left(\mathbf{R}_i\right)\Big|_\perp = \nabla E\left(\mathbf{R}_i\right) - \nabla E\left(\mathbf{R}_i\right)\cdot\hat{\tau}_\|\hat{\tau}_\|. \tag{2.69}$$

$\nabla E\left(\mathbf{R}_i\right)$ is the gradient of the system's energy as a function of atomic coordinates

at image i, $\hat{\tau}_i$ is the normalized local tangent vector at image i, and κ is the spring constant. The NEB is an iterative minimization method, the program performs a DFT calculation to compute the force acting on the system for each image, where each image is simultaneously optimized to find the MEP.
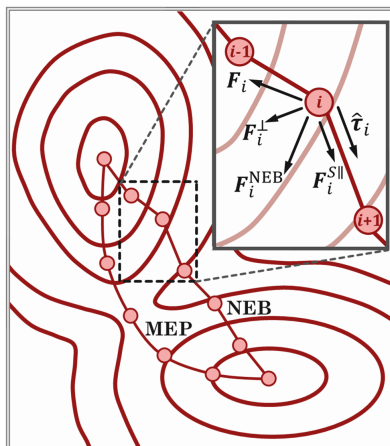
Figure 2.2: Representation of $\mathbf{F}_i^{\mathrm{NEB}}$: the spring force $\mathbf{F}_i^{S\parallel}$, along the tangent $\hat{\tau}_i$, and the perpendicular force due to the potential $\mathbf{F}_i^{\perp} = -\nabla E\left(\mathbf{R}_i\right)\big|_{\perp}$. Figure adapted from reference [71].

2.9 Bader charge analysis

In Bader's theory, the atomic regions are divided based on zero flux surfaces, i. e., the normal component of the charge density gradient is zero for any point on that surface ($\nabla \rho(\mathbf{r}) \cdot \hat{\mathbf{n}} = 0$), as shown in figure 2.3 (a). In this thesis, we used an algorithm for partitioning the charge density grid into Bader volume, which is a good approximation of the total electronic charge of an atom. Therefore, it is an effective method for charge analysis, described in detail in the following references: [74–77].

Figure 2.3 (b) presents the near-grid method, where space is divided so that each grid point and volume is allocated to a Bader volume for density integration. However, this grid-based partition would bring numerical integration errors due to finite grid sizes. Accordingly, M. Yu and D. R. Trinkle [77] introduced a weight function to improve the integration accuracy, where the weight represented the vol-

ume fractions of the cell. Figure 2.3 (c) illustrated the grid-based weight, where the grid points begin with a weight of 1 (red color) closer to atom A, decreasing to the weight of 0 (white color) as grid points became far away from atom A.
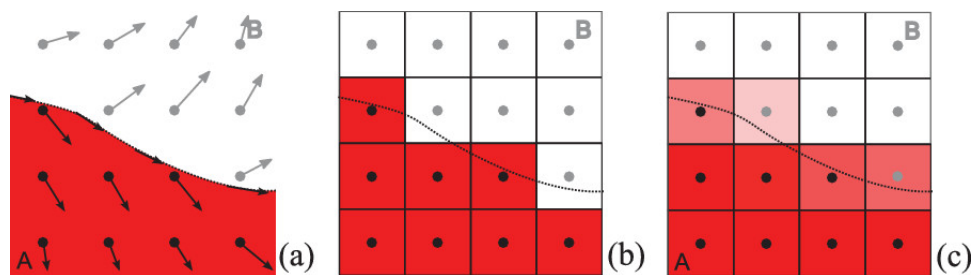
Figure 2.3: (a) Zero flux surface dividing volumes A (red) and B (white), where arrows denote charge density gradients ($\nabla \rho(\mathbf{r}) \cdot \hat{\mathbf{n}} = 0$ for any point on the surface); (b) grid-based partition from the near-grid algorithm; (c) weighted integration with fractional atomic contribution. Figure reproduced from reference [77].

2.10 Computational Details

We performed first-principles calculations, based on the Density Functional Theory (section 2.2), using the plane-wave basis set and projector augmented-wave (PAW) method (section 2.2.3), as implemented in the Quantum ESPRESSO computational package [72, 73]. The valence electronic configurations of the atoms were described by: Li $[1s^2\, 2s^1]$, B $[2s^2\, 2p^1]$, C $[2s^2\, 2p^2]$, N $[2s^2\, 2p^3]$, Na $[2s^2\, 2p^6\, 3s^1]$, Al $[3s^2\, 3p^1]$, Si $[3s^2\, 3p^2]$, P $[3s^2\, 3p^3]$, and K $[3s^2\, 3p^6\, 4s^1]$. For the exchange-correlation functional (section 2.2.2), we utilized the generalized gradient approximation of Perdew-Burke-Ernzerhof (GGA-PBE) and the Dion *et al.* scheme optimized by Klimeš *et al.* (optB88-vdW) to adequately describe the effects of the dispersive van der Waals (vdW) interaction. For an accurate description of the energy band gap values, we employed the hybrid Heyd-Scuseria-Ernzerhof (HSE) functional at the relaxed structures obtained from the optB88-vdW approximation. We calculated the phonon dispersion curves through the Density Functional Perturbation Theory

(section 2.3) with an $8 \times 8 \times 1$ q-point mesh. The *ab-initio* molecular dynamics simulations (section 2.6) were carried out using the Vienna *ab initio* simulation package (VASP) [64].

The 2D structures were simulated with a hexagonal cell, considering periodic boundary conditions. The lattice parameter in the direction perpendicular to the sheets (z-axis) was set at 25 Å, to prevent interactions among cell images, and in the xy-plane the cells contained 2, 4, and 6 atoms for the monolayers, bilayers, and trilayers, respectively. We used a plane-wave energy cutoff of 1100 eV with a convergence threshold of 0.1 meV/atom for the total energy. Moreover, we used a $16 \times 16 \times 1$ k-point mesh to describe the irreducible Brillouin zone [78] of the cell. During structural optimization, relaxations and distortions were considered in all ions, the cell parameters in the xy-plane were obtained using a variable-cell optimization with BFGS quasi-newton algorithm, and the forces on atoms were converged down to 1 meV/Å.

3. 2D diamond-like functionalized graphene nanosheets

> É sempre nessa violação do que é considerado certo que nasce o novo e há a criação. (It is always in this violation of what is considered right that the new is born and there is the creation).
>
> *Mário Schenberg*

The discovery of graphene has created a new field in Science, the 2D materials, leading to many 2D structures with considerably different physical properties to be predicted and synthesized. The 2D diamonds, for instance, can be built out of bilayer graphene (BLG) or few-layer graphene (FLG) through different techniques, and it is often required to functionalize its surface with functional groups to stabilize the 2D diamond [24, 79]. Those 2D systems are potential candidates for applications in many areas, and hence it is of great interest to investigate and understand their properties. In this chapter, we explore the physical properties of 2D diamond-like graphene nanosheets functionalized with nitrogen and/or boron atoms. Accordingly, this chapter includes a summary of Paper I: *Carbon-Related Bilayers: Nanoscale Building Blocks for Self-Assembly Nanomanufacturing* [21] and Paper II (Manuscript): *Physical properties of functionalized 2D diamond.* The computational details are in section 2.10 of chapter 2.

3.1   Carbon-related bilayers

Herein, we discuss the properties of graphene-like functionalized monolayers/bilayers and the possibility of their use as two-dimensional building blocks. It is necessary to point out here that we called graphene-like bilayers the vertical covalent bonding of two monolayers in our paper. However, these structures are minimal building blocks, in other words, monolayers with two atomic layers (2D diamond-like). The readers are encouraged to read the original paper for more details of the methods and discussions [21].

3.1.1   Stability of monolayers and bilayers

We first investigated a graphene sheet 50% doped with substitutional nitrogen (h-CN) or boron (h-CB) atoms, as shown in figure 3.1 (a). However, they were dynamically unstable, presenting phonon spectra with imaginary frequencies in some branches, in accordance with results from other theoretical investigations [80, 81]. Therefore, to overcome the dynamic instability of these monolayers and still obtain an ordered and stable 50% N- or B-doped graphene-like systems, we explored the stability and properties of graphene-like bilayers, with both the AA-stacking and AB-stacking configurations, doped with substitutional N and B atoms. A schematic representation of these structures are displayed in figures 3.1 (b) and (c), along with the labels given for the interatomic distances and bond angles.

To check the structural stability, we have obtained the phonon dispersion curves of these bilayers, which results are shown in figure 3.2 for the dynamically stable ones. The primitive cell structure contains 4 atoms and, hence 12 phonon branches presenting only positive frequencies, indicating structural stability. The in-plane acoustic modes, labeled as transverse (TA) and longitudinal (LA), exhibited linear variation at q for $q \to 0$ in the Γ point, while the out-of-plane transverse acoustic mode (ZA) mode showed a quadratic dispersion at q close to the Γ point, which was similar to the theoretical and experimental results for graphene and graphite [82, 83]. It is worth mentioning that we have also explored the bilayers formed by stacking
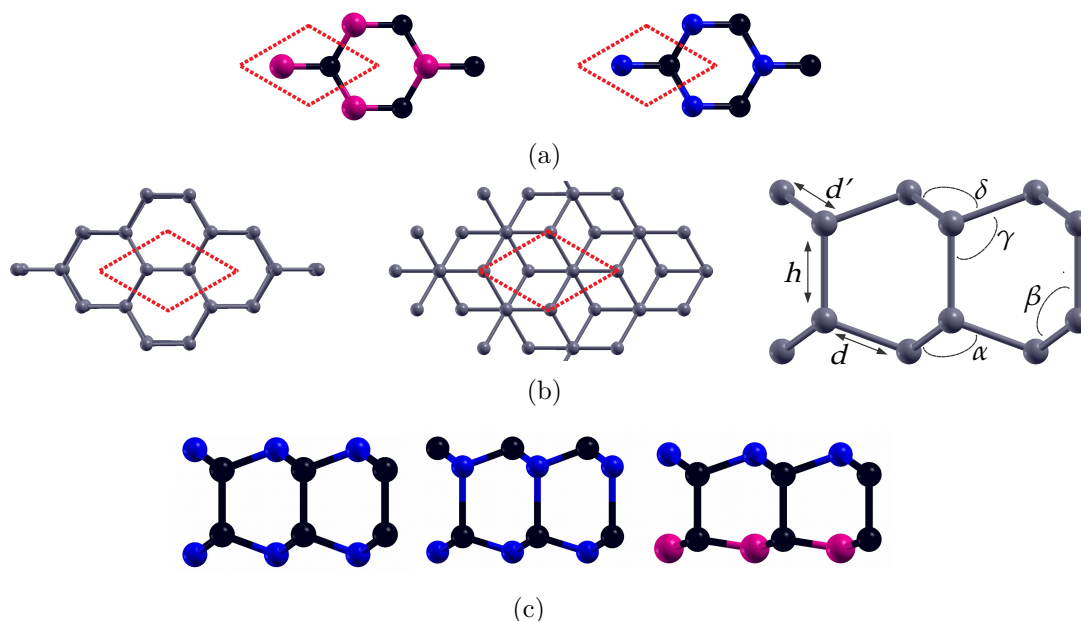
Figure 3.1: Schematic representation of (a) the top view of the monolayers 50% doped graphene with B or N atoms; (b) the top view of a bilayer in the AA-stacking (left) and AB-stacking (middle), and the side view of a bilayer (right); (c) the NCCN (left), the NCNC (middle) and the NCCB (right) bilayers investigated here. The black, pink, and blue spheres represent carbon, boron, and nitrogen atoms, respectively. The red dashed lines represent the limits of the unit cells in all structures. The right side of the panel (b) shows the labels given for the inter-layer distance h, the interatomic distances d, and d' between atoms in each layer of the system. α, β, γ, and δ are the bond angles. Reproduced from Paper I [21].

two h-CB monolayers with 50% B-doped graphene-like bilayers (BCCB) in both stacking configurations and found no dinamically stable structure.

According to a previous investigation, the two-dimensional hexagonal lattice of carbon nitride structures should be unstable with an N concentration exceeding 37.5% [80]. However, we found stable systems formed by stacking two h-CN monolayers with 1:1 stoichiometry, i.e., a 50% N-doped graphene-like bilayer. The stable 50% N-doped graphene-like bilayers named AA-NCCN, AB-NCCN, AA-NCNC, and AB-NCNC are presented in figure 3.1. The AA-NCCB and AB-NCCB systems formed by stacking an h-CN layer with an h-CB one, with 25% N- and 25% B-doped graphene-like bilayers, are also dynamically stable according to the phonon spectra.
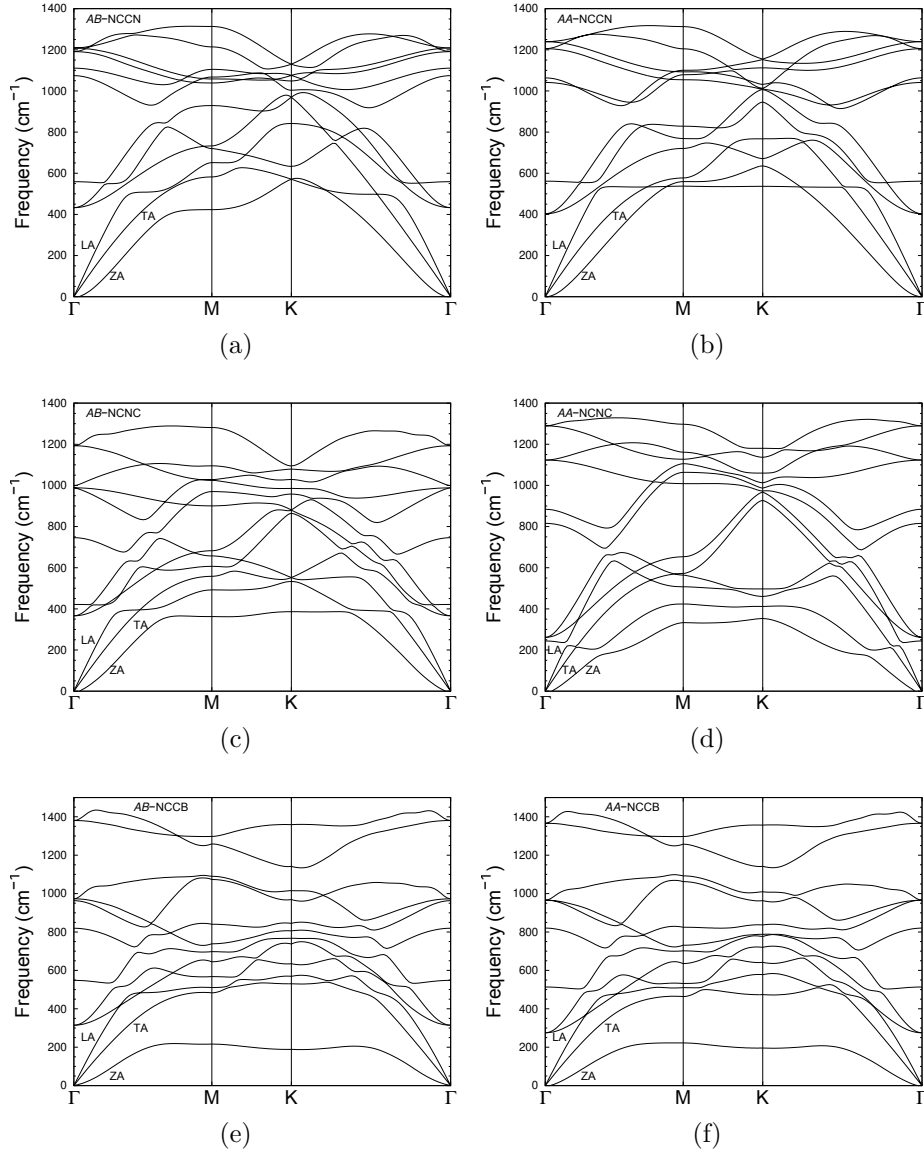
Figure 3.2: Phonon dispersion of (a) AB-NCCN, (b) AA-NCCN, (c) AB-NCNC, (d) AA-NCNC, (e) AB-NCCB, and (f) AA-NCCB in the main high-symmetry directions of the BZ for the hexagonal lattice. Reproduced from Paper I [21].

3.1.2 Formation energy

The formation energy E_f, described in chapter 2, section 2.5, of any bilayer, was computed by

$$E_f = E_{\text{tot}}(\text{C}_2\text{N}_x\text{B}_y) - 2E(\text{C}) - xE(\text{N}) - yE(\text{B}), \qquad (3.1)$$

where $E_{\text{tot}}(\text{C}_2\text{N}_x\text{B}_y)$ is the total energy of the bilayer, per formula unit, with two carbon, x nitrogen, and y boron atoms. The $E(\text{C})$, $E(\text{N})$, and $E(\text{B})$ are the total energies, per atom, of respectively carbon, nitrogen, and boron, in their standard reference states, which are graphite, the N_2 isolated diatomic molecule and the β-boron trigonal crystalline structure.

Table 3.1 presents the properties of the NCCN, NCNC, and NCCB dynamically stable bilayers in the AA- and AB-stacking configurations. Among those structures, the AB-NCCN bilayer was the energetically most favorable one, and then we chose its formation energy as the reference value. Energetically, this configuration was followed by the AA-NCCN one, whose formation energy was only 35 meV higher than that with the AB-stacking. Although, the NCNC bilayers were also dynamically stable in both stackings, they presented energies of formation much higher than the AB-NCCN reference system. The AA-NCNC bilayer is energetically more stable than the AB-NCNC one by only 13 meV, with slightly different structural properties. The formation energy of the AA-NCCB and AB-NCCB systems were, respectively, 0.687 eV and 0.486 eV higher than the reference value (AB-NCCN).

3.1.3 Structural properties

Table 3.1 presents the properties of NCCN, NCNC, and NCCB bilayers in AA- and AB-stacking configurations. In the energetically most favorable AB-NCCN bilayer, the C-N interatomic distances, d and d', the distance h between layers, and the bond angles α, β, γ, and δ indicated that the interlayer bonding was primarily covalent with sp^3 character. This hybridization differs substantially from a graphite-like sp^2 bonding found in fullerenes, nanotubes, and graphene. All results were in good

Table 3.1: Properties of NCCN, NCNC, and NCCB bilayers in AA- and AB-stackings: lattice parameter (a), inter-layer distances (h) and interatomic distances within the layers (d and d'), and bond angles (α, β, γ, and δ), as defined in figure 3.1. E_g is the bilayer band-gap and ΔE_f is the relative formation energy, with respect to the AB-NCCN system. Distances, angles, and energies are given in Å, degrees, and eV, respectively. Results of another theoretical investigation [84], given in parenthesis, were obtained for a graphite-like bulk system by using the PBE-GGA functional to describe the exchange-correlation term within the DFT, without considering the dispersive vdW interaction. Reproduced from Paper I [21].

stacking	AA			AB		
struture	NCCN	NCNC	NCCB	NCCN	NCNC	NCCB
a	2.379	2.375	2.557	2.392(2.395)	2.394(2.394)	2.557
h	1.635	1.914	1.672	1.576	1.599	1.659
d	1.465	1.436	1.564	1.471(1.475)	1.461(1.455)	1.559
d'	1.465	1.462	1.495	1.471(1.475)	1.507(1.508)	1.494
α	108.6	111.5	109.6	108.8	110.0	110.2
β	110.3	107.3	109.3	110.2(110.3)	108.9(108.2)	108.7
γ	110.3	110.3	99.0	110.2(110.3)	113.3(113.5)	98.8
δ	108.6	108.6	117.6	108.8	113.6	117.7
E_g	3.910	1.114	1.771	4.637(3.638)	2.299(1.948)	1.641
ΔE_f	0.035	2.218	0.687	0.000	2.346	0.486

agreement with the ones obtained by another investigation for the graphite-like NCCN crystal [84], as indicated in table 3.1. In the NCNC structures, the C-N interatomic distances (d and d'), the bond angles, and the distance between layers (h) were strongly affected when we compared to the values of the NCCN structures.

Replacing N atoms with B ones on one side of an NCCN bilayer, an NCCB bilayer is formed. Although boron and nitrogen atoms have similar atomic sizes, the incorporation of the boron atoms led to important changes in the properties of the resulting structures. The C-N interatomic distances are 1.564 Å and 1.559 Å for AA- and AB-stacking, respectively, which are larger than in the NCCN and NCNC structures. The inter-layer distance h (C-C interatomic distance) for both stackings, 1.672 Å (AA-NCCB) and 1.659 Å (AB-NCCB), are larger than the one in the diamond crystal. However, both of them still have a strong covalent inter-layer

bond.

Regarding interatomic distance h, we minimized the system's total energy by relaxing the positions of each atom. For example, the calculation of the relative total energies as a function of the interplanar carbon-carbon distance h_{C-C} for the AB-NCCN bilayer led to minimum energy with $h_{C-C} = 1.576$ Å, as presented in figure 3.3. We applied the same procedure to the other stable bilayers presented in this section to find the equilibrium interplanar distance between two monolayers.
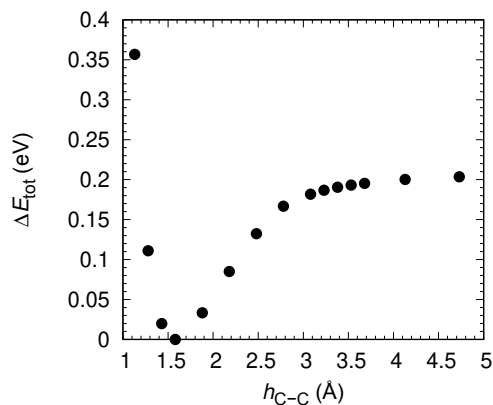
Figure 3.3: Relative total energy (ΔE_{tot}) as a function of the interplanar carbon-carbon distance h_{C-C} for the AB-NCCN bilayer.

3.1.4 Electronic properties

Figure 3.4 (a) shows the AB-NCCN system electronic band structure and the total (DOS) and projected (PDOS) density of states on the C and N atomic orbitals. It presented an indirect electronic gap of 4.637 eV, with the highest occupied state (E_v) at the Γ-point and the lowest unoccupied state (E_c) at the M-point. This gap value is larger than that of the crystalline diamond of 4.356 eV, computed using the same methodology. The valence band top has a prevailing p-N character with some contributions from the s-N, p-C, and s-C states. The conduction band bottom has contributions mainly from the p-C related states and some from the p-N states. In figure 3.4 (b), the AA-NCCN bilayer, which has a formation energy 35 meV higher
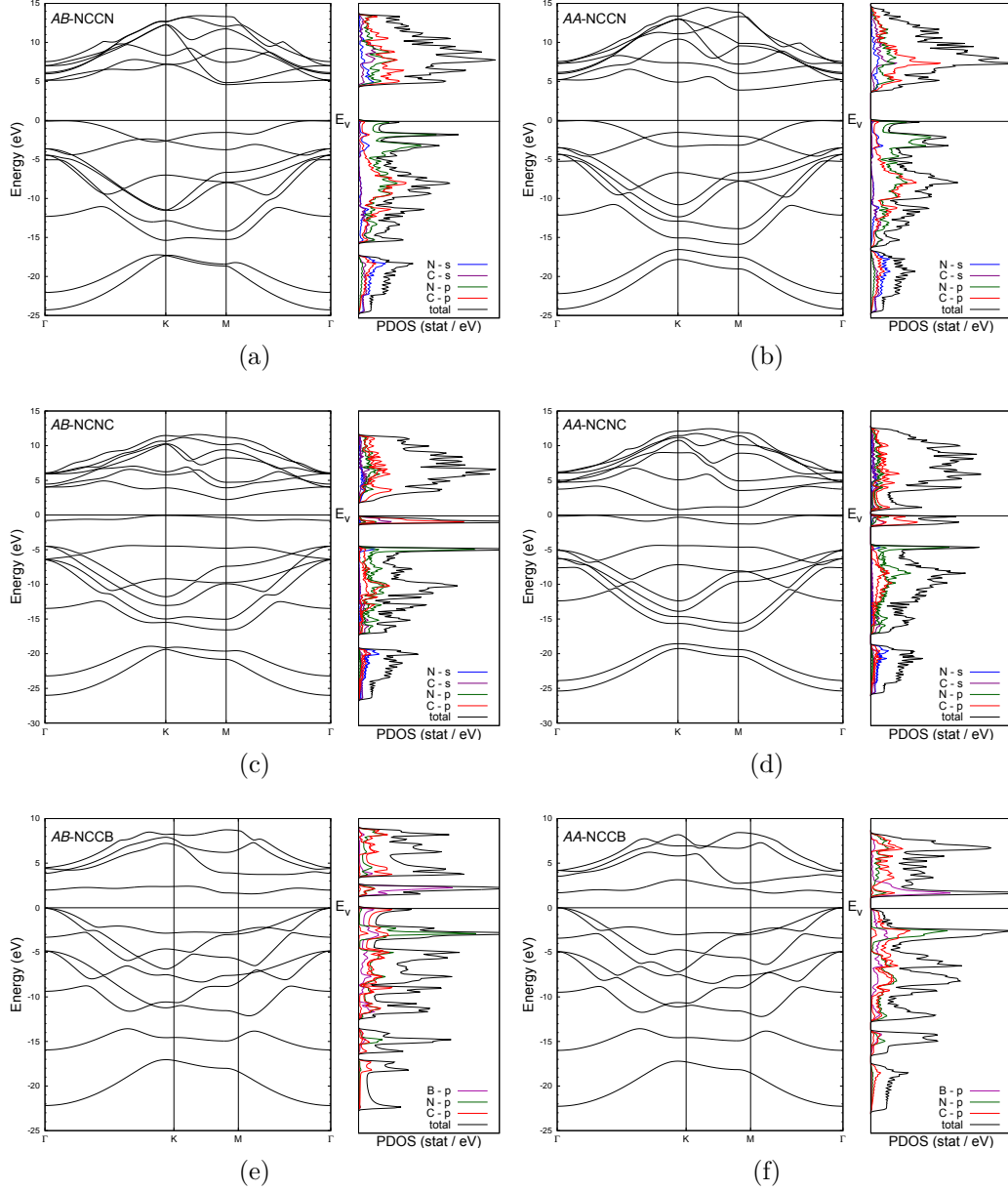
Figure 3.4: Electronic band structures of (a) AB-NCCN, (b) AA-NCCN, (c) AB-NCNC, (d) AA-NCNC, (e) AB-NCCB, and (f) AA-NCCB configurations, in the high-symmetry directions of the BZ. The figure also shows the total (black) and projected density of states on the s orbitals of C (purple) and N (blue) atoms, and on the p orbitals of C (red), N (green), and B (pink) atoms, in units of the number of states/eV. E_v represents the valence band top. Reproduced from Paper I [21].

than the AB-NCCN one, has a smaller gap value of 3.910 eV with similar physical properties, as can be noticed in table 3.1 and figure 3.4.

Figures 3.4 (c) and 3.4 (d) show respectively the AB-NCNC and AA-NCNC electronic band structure, DOS and PDOS on the C and N atomic orbitals. Additionally, the indirect electronic gap was 2.299 eV for the AB stacking and 1.114 eV for the AA, with the AA stacking having the smallest gap among the stable structures studied in this section. According to figure 3.4 (c), the valence band top has a prevailing p-C character with some contribution from the p-N and s-C states, while the conduction band bottom has mainly contributions from the p-C states and some from the p-N states. Moreover, the atomic orbitals of the valence band top and conduction band bottom of the AA-NCNC have a similar composition to the AB-NCNC one. The results for AB-NCCN and AB-NCNC structures are in good agreement with values obtained by another investigation in the literature for the graphite-like NCCN and NCNC bulk [84] (see parenthesis in table 3.1).

The replacement of nitrogen (in NCCN) with boron to build the NCCB structures reduced the energy gap from 4.637 eV to 1.641 eV for the AB-stacking and from 3.910 eV to 1.771 eV for the AA-stacking. Figures 3.4 (e) and (f) show, respectively, the AB- and AA-NCCB electronic band structure, the DOS, and the PDOS on the C, B, and N atomic orbitals. Near the valence band top, atomic orbitals have mainly contributions from the p-C and p-B states and some of the p-N one. However, those near the conduction band bottom have primarily contributions from the p-B state and some from the p-C and p-N ones. All those theoretical gap values presented in this section are lower limits for the real ones since the DFT/vdW generally underestimates gap values.

Figure 3.5 displays the density distributions probability on the region around E_v and E_c. For AA- and AB-NCCN, the states near E_v are associated with the C-C interatomic bonds plus the N-lone pairs (non-bonding), while the states around E_c are associated with the C-C plus the C-N bonds, as shown in figures 3.5 (a)-(d). Regarding NCCB bilayers exhibited in figures 3.5 (e)-(h), the density around E_v is related mainly to the C-C and C-B interatomic bonds. However, around E_c it is due

to the C-N bonds with an antibonding character, distributed in the backbond of the N atoms. These density distributions probability provided complementary information for weight contributions analysis of each s and p orbitals on band structures, DOS, and PDOS shown in figure 3.4.
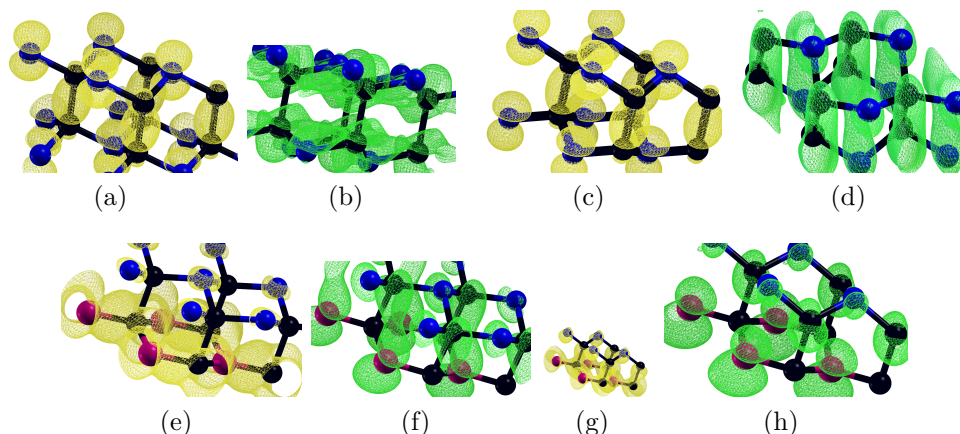
Figure 3.5: Electronic charge density distributions of the bilayers in the region around E_v for (a) AB- and (c) AA-NCCN, and for (e) AB- and (g) AA-NCCB. It is also shown the distributions in the region around E_c for (b) AB- and (d) AA-NCCN, and for (f) AB- and (h) AA-NCCB. Reproduced from Paper I [21].

3.1.5 NCCB 3D crystals

As exposed previously, we found a set of stable bilayers that could be used as 2D building blocks for nanostructure self-assembly, providing strong bonding between different bilayers. Although the NCNC bilayers have distinct atomic edges (associated with carbon or nitrogen atoms), which could help self-assembly growth, we discarded them as potential building blocks since their formation energies are much larger than the other bilayers. Regarding NCCN bilayers, the ideal building block partner would be a BCCB bilayer, which was dynamically unstable and, therefore, unsuitable to serve as a building block. Even if a BCCB bilayer were dynamically stable, there would still be a challenge in placing an NCCN bilayer over a BCCB one, self-assembled, due to a lattice mismatch between them. Therefore, the NCCN bilayers do not seem appropriate to serve as a 2D building block

for self-assembly. However, they could still find applications in other fields since nitrogen-doped graphene has also been widely investigated and proposed as supercapacitors [85], semiconducting devices [86], hydrogen storage [87] and battery anodes [88, 89].

To explore the possibility of an NCCB serving as a 2D building block, we investigated the properties of 3D crystals made from stacking these building blocks. The first crystal has optimized lattice parameters of $a = 2.590$ Å and $c = 8.417$ Å. The boron atoms from one AB-NCCB bilayer are located above the nitrogen atoms from the adjacent AB-NCCB bilayer, as shown in figure 3.6 (a). The C-C intra-bilayer distance (h) is 1.439 Å, which is smaller than the one in the diamond crystal but close to the in-plane graphite and graphene bond lengths, indicating a covalent bond between those carbon atoms. Additionally, the B-N inter-bilayers distance of 1.645 Å is similar to the B-N dative bonding found in several other structures [90, 91]. The C-C covalent bond and B-N dative one could guarantee the stability and rigidity of the resulting crystalline structure.

Moreover, the self-assembly could be facilitated by the ionic-like driving force between N and B atoms from neighboring building blocks since N has a donor character while B has an acceptor one. The binding energy ($E_b = 0.16$ eV/atom) and the bulk modulus of the crystal ($K_0 = 328.9$ GPa) indicate that this structure presents characteristics of hard material with covalent bonding [92]. We obtained the K_0 by fitting the third-order finite strain Birch-Murnaghan equation of state to the energy vs. volume relation [93]. Additionally, the crystal has a small indirect electronic gap of 0.65 eV, shown in figure 3.6 (c), where the valence band top has mainly contributions from the p-C and p-N states (C-N bond), whereas the conduction band bottom has from the p-C and p-B states (C-B bond).

The second crystal built in a graphite-like structure has optimized lattice parameters of $a = 2.563$ Å and $c = 5.090$ Å. In this structure, the B and N atoms are above/below the hexagonal hollow site of the adjacent bilayer, as shown in figure 3.6 (b). The C-C intra-bilayer distance is 1.587 Å, close to the diamond crystal and in the same order as in graphite and graphene, indicating a covalent bond between
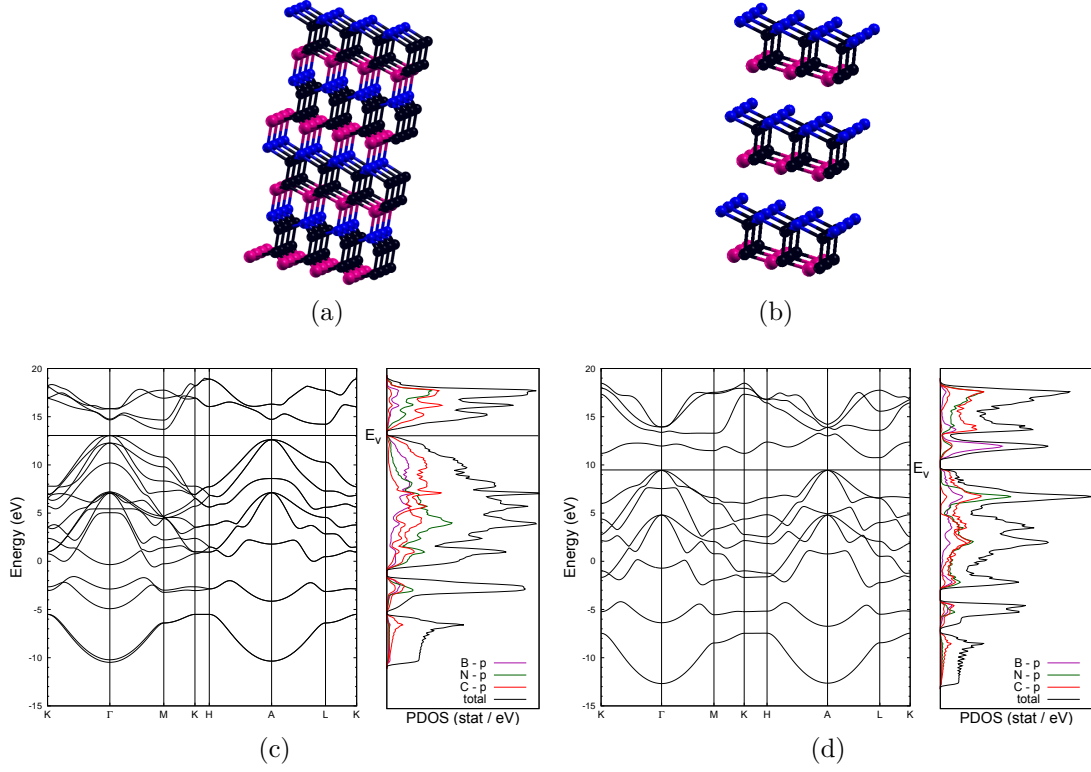
Figure 3.6: Schematic representation of (a) NCCB covalent crystal and (b) NCCB graphite-like one, where the black, pink, and blue spheres represent carbon, boron, and nitrogen atoms, respectively. Electronic band structures of the (c) covalent-like and (d) graphite-like crystal configurations, in the main high-symmetry directions of the BZ. The figure also presents the total (black) and projected density of states on the p orbitals of C (red), N (green), and B (pink) atoms, in units of the number of states/eV. E_v represents the valence band top. Reproduced from Paper I [21].

the carbon atoms.

Additionally, the inter-bilayer distance is 2.685 Å and the bulk modulus is 79.3 GPa. The value of 70 meV/atom obtained for the average binding energy was close to that found for graphite in our calculation. These values suggest that this crystal could be classified as a layered material since it presented strong and covalent intra-bilayer bonds with weak (van der Waals-like) inter-bilayer bonds. Regarding electronic properties, the crystal exhibited an indirect gap of 1.246 eV, as shown in figure 3.6 (d), where the valence band top has contributions primarily from the p-C

and p-B states and the conduction band bottom has from the p-B states with some from the p-C and p-N ones.

3.1.6 Conclusion

In summary, we have investigated the properties of graphene-like carbon mono and bilayers functionalized with nitrogen and boron atoms. All functionalized graphene monolayers were dynamically unstable according to their phonon spectra. Accordingly, we analyzed the functionalized graphene-like bilayers (NCCN, NCNC, BCCB, and NCCB) regarding stability, structural, and electronic properties, finding some semiconductor and insulator dynamically stable systems. Among the resulting stable structures explored, we studied three-dimensional crystals formed by stacking NCCB bilayers and found they are energetically stable. Therefore, the NCCB bilayer is a potential candidate as a nanoscale two-dimensional building block for the self-assembly of macroscopic systems.

3.2 Functionalized 2D diamond

The 2D diamond has received considerable attention in the last few years, with promising applications in several fields, such as batteries, quantum computing, nano-optics, and nanoelectronics [24]. Herein, we initially explored the physical properties of pristine 2D diamond in $AA'A''$ and ABC stacking structural configurations, composed of three graphene layers, in the diamond-like form, with the C atoms between layers covalently bonded. After full atom position relaxations, the simulations showed the nanosheets converge to trilayer graphene systems with vdW interactions between layers (graphite-like). This behavior has also been found in a previous theoretical investigation of 2D diamonds, starting the simulations with two graphene layers. These results occur due to the absence of an external pressure-induced or surface passivation to transform sp^2 bonds into sp^3 ones [94]. Accordingly, those structures represent the chosen reference systems such that we can explore the changes in the properties of the systems with functionalization.

3.2.1 Structural properties

We explored the properties of C_4X_2 (X = B or N) systems, described as three graphene sheets where four C atoms are bonded covalently (2D diamond-like) in each unit cell. Moreover, the two external layers are 50% doped with substitutional X atoms, where each X atom is bonded to three C atoms. In figure 3.7, we presented the schematic representation of the optimized and relaxed C_4X_2 (X = B or N) systems, in both AA'A'' and ABC stacking configurations, as well as the respective labels given to the intraplanar bond angle (θ), intralayer (d_{C-X}) and interlayer (h_{C-X})
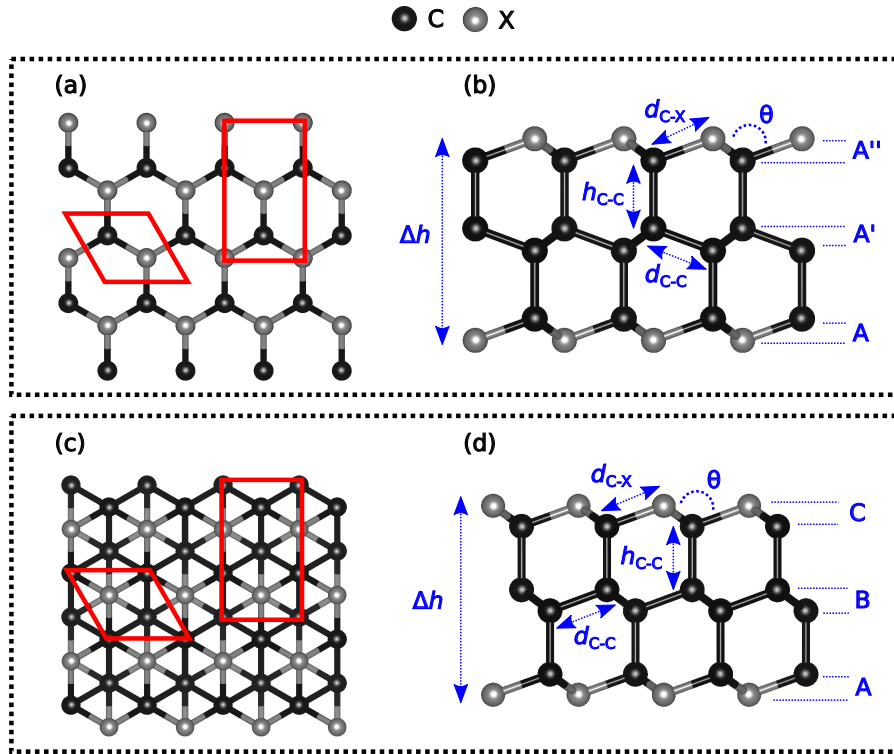
Figure 3.7: Schematic illustration of the C_4X_2 (X = B or N) system. (a) top and (b) side view of AA'A''-C_4X_2, (c) top and (d) side view of ABC-C_4X_2. The black and gray spheres represent the C and X atoms, respectively. The red lines denote the simulation unit cell limits, with the rectangle cells used only to determine the elastic properties. The labels given to the intralayer (d_{C-X}) and interlayer (h_{C-X}) distances, structures' thickness (Δh), and the intraplanar bond angle (θ) are also displayed.

distances, and systems' thickness (Δh).

The optimized structural parameters of C_4X_2 (X = B or N) are shown in table 3.2, where the distance labels are consistent with the ones defined in figure 3.7.

We observed that all the nanosystems functionalized with N atoms kept the lattice constants almost unchanged if we compared them to the PD ones. Moreover, the values of C_4N_2 intraplanar bond angles (θ) are close to the sp^3 hybridization angle (109.47°), leading to a thickness of $\approx$ 4.7 Å for both stacking structures. Nevertheless, the C_4B_2 nanosheets lattice parameters are slightly greater than the HD and FD systems, with θ close to the value of 120°. The B atoms bonded to three adjacent C atoms present a sp^2-type hybridization, and hence we observed a shorter thickness of $\approx$ 4.2 Å if compared to the N-functionalized structures.

Table 3.2: Structural properties of C_4X_2 (X = B or N): the lattice parameters (a), intralayer (d) and interlayer (h) distances, thickness (Δh), and the intraplanar bond angle (θ) are labeled according to figure 3.7. The distances are given in Å and angle in degrees. The table also gives the standard enthalpy of formation (ΔH_f^0) at 0 GPa, in units of meV/atom. For PD, HD, and FD, X = C.

System	a	d_{C-X}	d_{C-C}	h_{C-C}	Δh	θ	ΔH_f^0
AA'A''-C_4N_2	2.42	1.49	1.49	1.60	4.74	108.9	348
ABC-C_4N_2	2.44	1.50	1.50	1.57	4.66	109.0	333
AA'A''-C_4B_2	2.66	1.55	1.62	1.66	4.25	118.4	424
ABC-C_4B_2	2.67	1.55	1.63	1.65	4.18	118.5	365
PD[a]	2.43	Y[a]	1.54	1.65	—	Y[a]	300
HD[b]	2.53	1.56	—	1.56	—	—	—
FD[b]	2.56	1.55	—	1.55	—	—	—
NCCN	2.39[c]	1.47[c]	—	1.58[c]	2.59[d]	108.8[c]	211[d]

[a]Reference [95] - the ($\bar{2}$110)-oriented h-diamane exibits two d_{C-X} and θ values → Y = 1.35 Å and 1.54 Å with sp^3 and sp^2 hybridizations. [b]Reference [96]. [c]Reference [21]. [d]Reference [97].

3.2.2 Thermodynamic stability

We now discuss the thermodynamic stability of C_4X_2 nanosheets. First, we computed the standard enthalpy of formation ΔH_f^0, displayed also in table 3.2, using equation (described in section 2.5 of chapter 2)

$$\Delta H_f^0 = \frac{E_t(C_4X_2) - 4E_t(C) - 2E_t(X)}{6}, \qquad (3.2)$$

where $E_t(C_4X_2)$ is the total energy of the 2D system, with 4 C atoms and 2 X atoms (X = B or N) in the primitive cell. $E_t(C)$ and $E_t(X)$ are the total energies, per atom, of the respective C and X standard ground states, i.e., of graphite, crystalline boron in the trigonal structure (β-boron), and isolated N_2 molecule.

We found positive values of ΔH_f^0 of 348 meV, 333 meV, 424 meV, and 365 meV for AA'A''-C_4N_2, ABC-C_4N_2, AA'A''-C_4B_2, and ABC-C_4B_2, respectively, as displayed in table 3.2, indicating a possible thermodynamic instability. However, there are 2D materials synthesized by endothermic process ($\Delta H_f^0 > 0$) reported in the literature, as shown in table 3.2. Moreover, de positive values found could be due to uncertainty on the DFT energies and likely due to the lack of interactions between the 2D materials and substrate in the simulations.

Finally, we explored the thermodynamic stability of the systems as a function of temperature. Accordingly, we used *ab-initio* molecular dynamics (AIMD) simulations, as implemented in the Vienna *ab-initio* simulation package (VASP) [64], using a 216-atom ($6 \times 6 \times 1$) hexagonal supercell, in order to allow possible structural reconstructions. A Nose-Hoover thermostat (NVT) ensemble was employed to carry out the calculations at several temperatures (from 0 to 1000K) for 5 ps, with a simulation time step of 1 fs. The AIMD simulations exhibited a small variation of total energy during 5 ps at 300K, as shown in figure 3.8, indicating that the structural integrity of those systems is maintained. Although we observed the same behavior for the C_4N_2 systems at 1000K, the C_4B_2 nanosheets presented some broken bonds at that high temperature, suggesting a structural degradation.
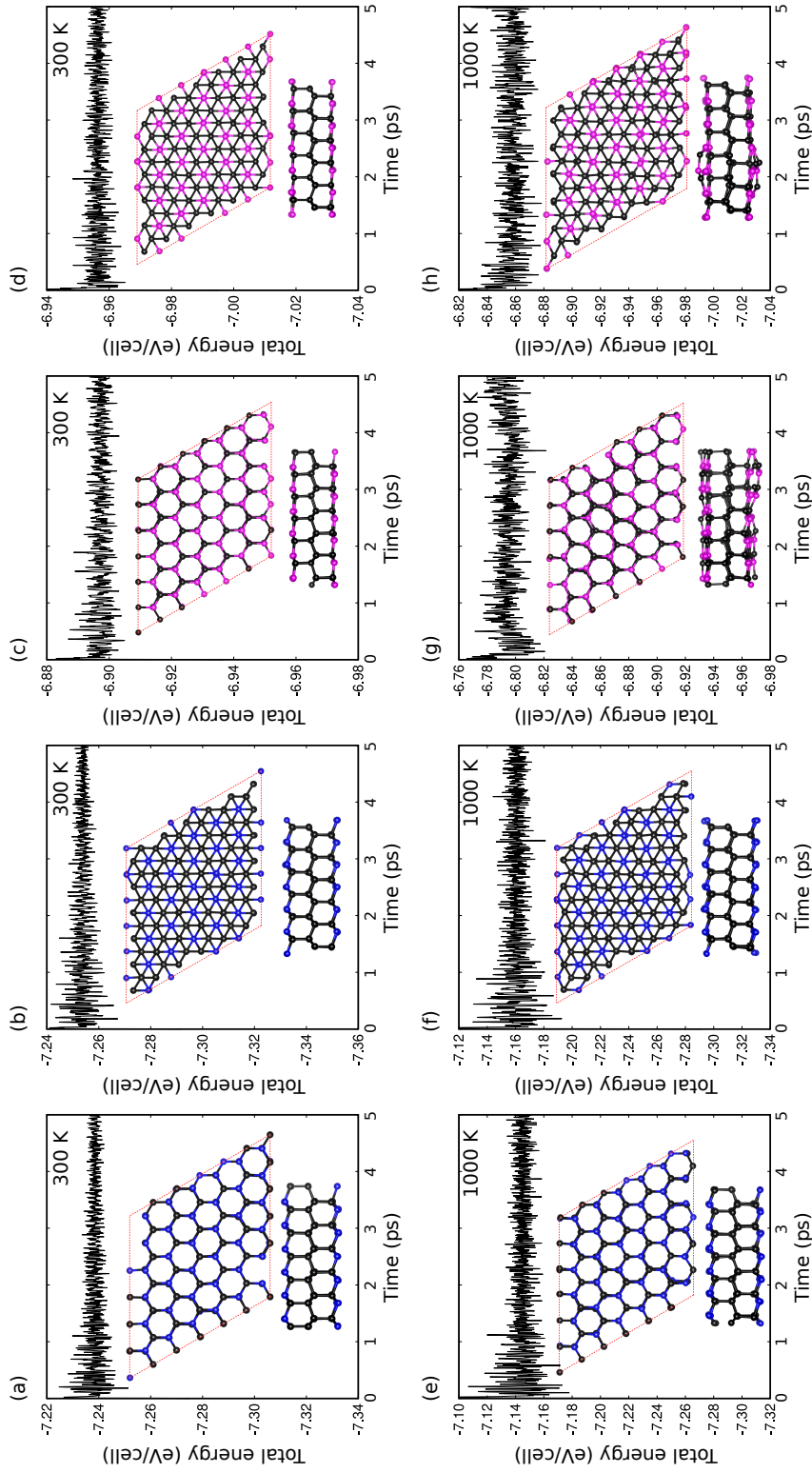
Figure 3.8: Variation in total energy during 5 ps of the *ab-initio* molecular dynamic simulation. At 300K of (a) AA′A″-C₄N₂, (b) AA′A″-C₄N₂, (c) AA′A″-C₄B₂ and (d) ABC-C₄B₂. At 1000K of (e) AA′A″-C₄N₂, (f) AA′A″-C₄N₂, (g) AA′A″-C₄B₂ and (h) ABC-C₄B₂.

3.2.3 Dynamic and mechanical stability

We next used the phonon theory to investigate dynamic stability, in which a system is considered stable when its vibrational spectra contain only positive frequencies. The phonon dispersion curves of C_4B_2 and C_4N_2 compounds, in both $AA'A''$ and ABC stacking configurations, are presented in figure 3.9. All spectra show 18 phonon branches since the primitive cell contains 6 atoms. We can observe that these systems are dynamically stable since there are only positive frequencies.

Furthermore, we computed the elastic constants of the systems with equation (2.48) to verify their mechanical stability, in which the Born stability criteria $C_{11} > 0$ and $C_{12} < C_{11}$ must be satisfied [58]. Herein, we built a rectangular cell with 12 atoms and used the strain-energy method described in section 2.4. Table 3.3 presents the elastic constants C_{11}, C_{22}, and $C_{44} = (C_{11} - C_{12})/2$, the Young modulus $Y^{2D} = (C_{11}^2 - C_{12}^2)/C_{11}$, and the Poisson ratio $\nu = C_{12}/C_{11}$ of C_4X_2 trilayers, as well as
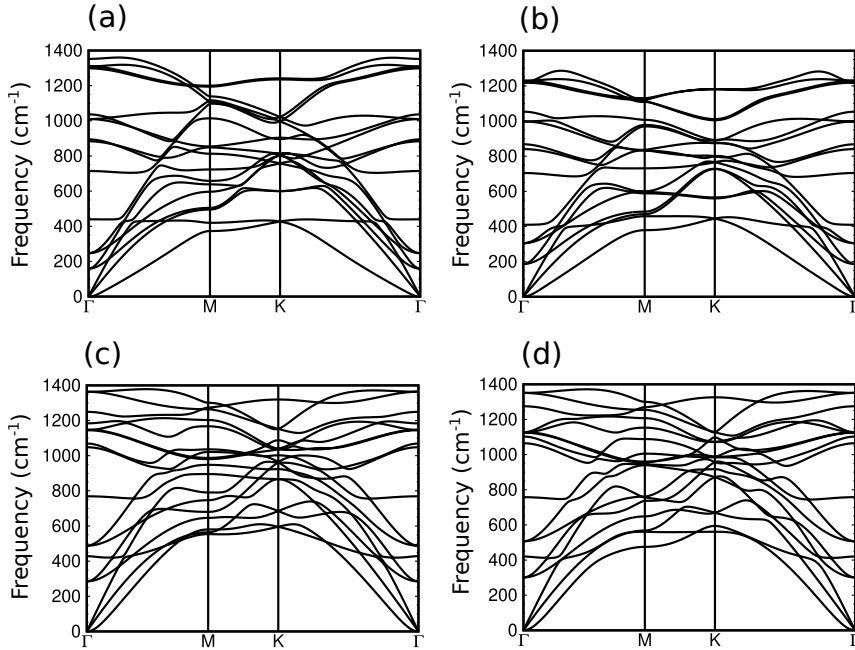
Figure 3.9: Phonon dispersion branches of (a) $AA'A''$-C_4B_2, (b) ABC-C_4B_2, (c) $AA'A''$-C_4N_2, and (d) ABC-C_4N_2 along the main high symmetry directions of the irreducible BZ of the hexagonal lattice.

of several other 2D materials for comparison. Accordingly, the C_4X_2 structures are mechanically stable since they satisfy the Born criteria, agreeing with the phonon dispersion spectra shown in figure 3.9. The C_4X_2 nanosheets present high Young modulus values and characteristics of isotropic systems since their Poisson ratio σ values are lower than 0.5 [100, 101]. Additionally, we estimated the longitudinal and the transversal acoustic velocities, given, respectively, by

$$v_{\text{LA}} = \left(\frac{C_{11}}{\rho_{\text{2D}}}\right)^{1/2} \quad \text{and} \quad v_{\text{TA}} = \left(\frac{C_{44}}{2\rho_{\text{2D}}}\right)^{1/2}, \tag{3.3}$$

where ρ_{2D} is a formal density in kg/m^2, allowing comparison between systems, independent of their thickness [24]. The velocity values, listed in table 3.3, suggest that the stiffness of the C_4X_2 systems is comparable with that of diamond.

Table 3.3: Elastic constants C_{11}, C_{12}, and C_{44}, Youngs modulus Y^{2D}, Poisson ratio σ, formal density ρ_{2D}, longitudinal v_{LA} and transverse v_{TA} acoustic velocities of C_4X_2 (X = B or N), graphene, and other 2D diamond-like systems. Elastic constants and Youngs modulus are given in N/m, Poisson ratio is dimensionless, formal density and velocities are given in 10^{-7} kg/m^2 and km/s, respectively.

System	C_{11}	C_{12}	C_{44}	Y^{2D}	σ	ρ_{2D}	v_{LA}	v_{TA}
AA′A″-C_4N_2	816	85	366	808	0.10	24.8	18.1	12.1
ABC-C_4N_2	777	82	348	769	0.11	24.5	17.8	11.9
AA′A″-C_4B_2	627	88	270	615	0.14	18.9	18.2	11.9
ABC-C_4B_2	609	92	259	595	0.15	18.7	18.0	11.7
Graphene	354[a]	60[a]	147*	340[b]	0.18[c]	7.55[c]	21.6*	13.9*
HD	474[c]	36[c]	219*	471*	0.08[c]	14.9[c]	17.8[c]	12.2[c]
ABC-HD	718[c]	58[c]	330	713*	0.08[c]	22.2[c]	18.0[c]	12.2[c]
FD	485[d]	49*	218*	480[d]	0.10*		14.0[1]	9.3[e]
NCCN	568[f]	66[f]	243[f]	560*	0.12*			
Diamond	1079[f]	124[f]	578[f]				18.3[c]	12.4[c]

[a]Reference [57]. [b]Reference [98] - experiment. [c]Reference [99]. [d]Reference [96]. [e]Reference [24]. [f]Reference [97]. *We calculated those values using the data from the table and the equations described in this section.

3.2.4 Electronic properties

Following, we studied the electronic band structures and the projected density of states (PDOS) of the C_4X_2 systems, displayed in figure 3.10 (a)-(d). The electronic band structures and PDOS of AA′A″-C_4N_2 and ABC-C_4N_2 nanosheets presented in figures 3.10 (a) and (b), despite their analogous PDOS with the N p-orbitals dominating at valence band maximum (VBM) and a mixture of N and C s- and p-orbitals at conduction band minimum (CBM), their band structures exhibit some differences. Although both systems exhibit the VBM around the Γ-point, the CBM is well defined at M-point for the ABC-C_4N_2, while in AA′A″-C_4N_2 the bottom of the conduction band is at K-point. On the other hand, for the AA′A″-C_4B_2 and ABC-C_4B_2 nanosheets the band structures are very similar, as shown in figures 3.10
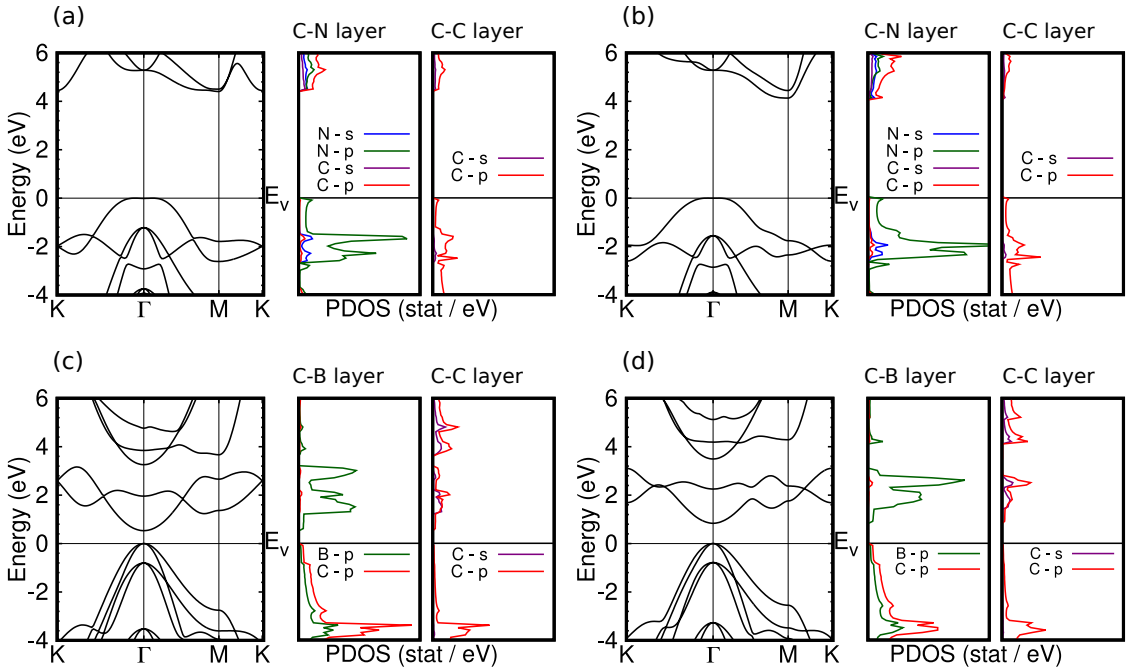
Figure 3.10: Electronic band structures along high-symmetry directions of the BZ and projected density of states (PDOS), using the optB88-vdW approach for the exchange-correlation energy: (a) AA′A″-C_4N_2, (b) ABC-C_4N_2, (c) AA′A″-C_4B_2 and (d) ABC-C_4B_2. The PDOS (states/eV) on the C and X s-orbitals are given in purple and blue, respectively, and on the C and X p-orbitals are given in red and green, respectively. E_v is the valence band maximum.

(c) and (d), with both systems presenting direct band gaps, where the VBM and the CBM are at the Γ-point, in which the B p-orbitals dominate at CBM, and in the VBM there is a combination of B and C p-orbitals.

The 2D diamond systems present a non-zero band gap with characteristics depending on several factors, such as doping with different functional groups. Herein, we are working with B and N atoms as X-doping elements. B atom belongs to group-III column of the periodic table, with valence electronic configuration $2s^2 2p^1$, and N atom to group-V, with valence electronic configuration $2s^2 2p^3$. As a result of the doping, we found a wide indirect band gap for the C_4N_2 nanosheets and a narrow direct band gap for the C_4B_2 ones, when compared to the PD value. Table 3.4 presents the band gap values of C_4X_2 nanosheets, obtained with the optB88-vdW approach [43] (E_g^{vdW}) and the hybrid HSE functional [44] (E_g^{HSE}) for the exchange-correlation energy, as well as the band gap of PD with three graphene layers. The band gap of PD, using hybrid HSE functional, is 2.70 eV, while for the functionalized AA'A''-C_4N_2, ABC-C_4N_2, AA'A''-C_4B_2, and ABC-C_4B_2 compounds the values are 5.56, 5.42, 1.64 eV, and 1.97 eV, respectively.

Table 3.4: Electronic band gap width values of C_4X_2 nanosheets (X = B or N), obtained with two different approximations for the exchange-correlation functional: optB88-vdW [43] (E_g^{vdW}) and HSE [44] (E_g^{HSE}). The PD band gap value is also displayed.

System	E_g^{vdW} (eV)	E_g^{HSE} (eV)
AA'A''-C_4N_2	4.40	5.56
ABC-C_4N_2	4.14	5.42
AA'A''-C_4B_2	0.53	1.64
ABC-C_4B_2	0.84	1.97
PD[a]		2.70

[a]Reference [95] - the ($\bar{2}$110)-oriented h-diamane with 3 graphene layers.

3.2.5   Future outlook

Herein, we investigated the physical properties of 2D diamond doped with substitutional N or B atoms. The systems consisted of three graphene sheets, one non-doped graphene layer between two 50% doped ones, and covalent C-C bonds between neighboring layers. The C_4X_2 (X = N or B) are dynamically, mechanically, and thermodynamically stable up to 300K. In particular, both stacking of the C_4N_2 nanosheets are also thermodynamically stable up to 1000K. According to the electronic structure, the C_4N_2 nanosheets are indirect band gap, while the C_4B_2 systems are direct band gap. Moreover, our results suggest that the stiffness of those systems is comparable to that of the diamond. Nevertheless, despite these interesting initial results, further investigations should explore the applicability of those systems, and we are currently studying their potential applications.

4. 2D diamond-like functionalized silicene nanosheets

> To succeed, planning alone is insufficient. One must improvise as well.
>
> *Isaac Asimov*

Silicene is a 2D material made of silicon atoms with a low-buckled hexagonal honeycomb structure due to the silicon sp^2-sp^3 hybridization. The single-layer and the few-layer silicene nanosheets are promising candidates for applications similar to those of graphene. Additionally, silicene's properties could be modified by, for instance, doping with different chemical elements and changing the stacking order [28, 102]. The 2D silicon-based materials have potential applications in several fields, particularly for energy storage systems. Therefore, this chapter explored the physical properties of 2D diamond-like silicene nanosheets functionalized with boron, nitrogen, aluminum, and phosphorus atoms. Furthermore, we studied the potential application of the aluminum functionalized few-layer silicene in alkali metal ion batteries. Accordingly, this chapter includes a summary of Paper III: *Functionalized few-layer silicene nanosheets: stability, elastic, structural, and electronic properties* [28] and Paper IV (Advance Article): *Aluminum functionalized few-layer silicene as anode material for alkali metal ion batteries* [30]. The computational details are in section 2.10 of chapter 2.

4.1   Functionalized silicene nanosheets

This section presents the results of *ab-initio* investigations on the properties of functionalized few-layer silicene (FLS) nanosheets, defined as Si_2X_2 bilayers and Si_4X_2 trilayers (X = B, N, Al, and P). Figure 4.1 shows schematic representations of those systems.
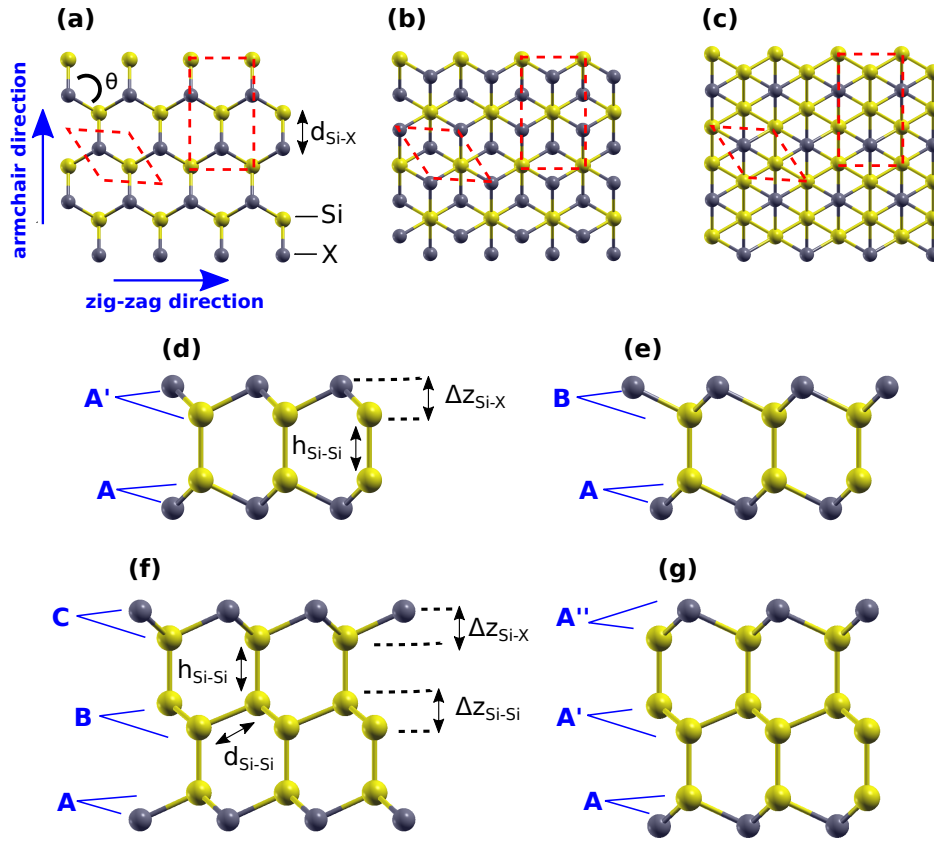
Figure 4.1:   Schematic representations of the Si_2X_2 bilayers and Si_4X_2 trilayers (X = B, N, Al, P). Herein, X = Si represents pristine silicene bilayer (Si_4) and trilayer (Si_6). Top view perspective of (a) AA′ and AA′A″, (b) AB, and (c) ABC stacking configurations; and side view perspective of (d) AA′, (e) AB, (f) ABC, and (g) AA′A″ configurations. For Si_6, the AA′A″ stacking is also known as AA′A. The yellow and gray spheres represent, respectively, Si and X atoms. The red dashed lines illustrate the hexagonal (rectangular) cells used to determine the dynamic, structural, and electronic (elastic) properties. The labels given to the d_{Si-Si} and d_{Si-X} intralayer, h_{Si-Si} interlayer, Δz_{Si-Si} and Δz_{Si-X} buckling distances, and the θ intraplanar bond angle are also displayed. Reproduced from Paper III [28].

The functionalized silicene bilayers consist of two 50% X-doped silicene nano-sheets, and the trilayers consist of three silicene nanosheets, one non-doped silicene layer between two 50% X-doped ones. It can be observed in figure 4.1, besides the schematic representations of the Si_2X_2 bilayers, in the AA$'$ and AB stacking configurations, and Si_4X_2 trilayers, in the AA$'$A$''$ or AA$'$A and ABC configurations, also the labels of the intralayer (d), interlayer (h), and buckling (Δz) distances, and the intraplanar bond angle (θ). Table 4.1, exhibited in next page, presents optimized structural parameters of the studied systems, as well as the respective values obtained for pristine silicene Si_2 monolayer, Si_4 bilayers, and Si_6 trilayers. The distances and angle labels are consistent with the ones defined in figure 4.1.

4.1.1 Structural properties

Regarding pristine FLS nanosheets, we found that the lattice constants for all the systems are very close, ranging from 3.847 Å (AB-Si_4) to 3.870 Å (Si_2). Moreover, the Si atoms prefer the sp^3 hybridization and, hence, the θ values decrease towards the tetrahedral value (109.47°) as the number of layers increases [101,103]. We also observed that the FLS nanosheets have covalent bonds, presenting interlayer h_{Si-Si} distances varying between 2.423-2.538 Å. Unlike the bilayer systems, the pristine silicene Si_6 trilayers have two additional structural parameters: the intralayer d_{Si-Si} and buckling Δz_{Si-Si} distances. The FLS systems exhibit structure parameter close to crystalline silicon, differing from the few-layer graphene and graphite that present weak interlayer van der Waals interactions.

In the functionalized FLS nanosheets, the Al substitution stretched the lattice parameter a and the intralayer distance d_{Si-Al}, while incorporating B, N, or P atoms reduced them. Moreover, the intraplanar bond angles of the systems functionalized with B and Al atoms are very close to the value of 120°, which is the expected value of the sp^2-type hybridization of B and Al atoms bonded to three adjacent Si atoms.

In the systems functionalized with N and P atoms, the intraplanar bond angles are smaller than in the pristine FLS, approaching the sp^3-type hybridization angle value. Although the buckling distances are greatly affected by the substitution,

Table 4.1: Structural properties of Si_2X_2 bilayers and Si_4X_2 trilayers (X = B, N, Al, P): lattice parameters (a), intralayer (d), interlayer (h), and buckling (Δz) distances, given in Å, and the intraplanar bond angle (θ), given in degrees, labeled according to figure 4.1. The standard enthalpy of formation (ΔH_f^0), obtained according to equation 4.1, is given in meV/atom. For pristine silicene Si_2 monolayer, Si_4 bilayers, and Si_6 trilayers, X = Si. The last column indicates the dynamic stability (DS) of the nanosheets. Reproduced from Paper III [28].

System	Structure	Stacking	a	d_{Si-X}	h_{Si-Si}	d_{Si-Si}	Δz_{Si-X}	Δz_{Si-Si}	θ	ΔH_f^0	DS
Monolayer	Si_2	—	3.870	2.285	—	—	0.482	—	115.67	751	Yes
	Si_4	AA'	3.854	2.325	2.470	—	0.676	—	111.89	609	Yes
		AB	3.847	2.322	2.538	—	0.676	—	111.89	570	Yes
	Si_2B_2	AA'	3.448	1.993	2.565	—	0.109	—	119.70	648	No
		AB	3.468	2.005	2.498	—	0.104	—	119.73	704	No
Bilayer	Si_2Al_2	AA'	4.231	2.457	2.572	—	0.271	—	118.79	446	No
		AB	4.242	2.457	2.514	—	0.200	—	119.34	404	No
	Si_2N_2	AA'	2.909	1.767	2.429	—	0.548	—	110.81	-743	Yes
		AB	2.921	1.771	2.393	—	0.541	—	111.08	-733	Yes
	Si_2P_2	AA'	3.544	2.286	2.380	—	1.019	—	101.65	-87	Yes
		AB	3.557	2.287	2.351	—	1.007	—	102.06	-84	Yes
	Si_6	AA'A	3.858	2.332	2.423	2.355	0.690	0.756	111.62	224	Yes
		ABC	3.858	2.333	2.435	2.355	0.695	0.764	111.51	220	Yes
	Si_4B_2	AA'A"	3.539	2.045	2.495	2.282	0.092	1.019	119.79	552	No
		ABC	3.568	2.061	2.403	2.272	0.086	0.900	119.82	529	Yes
Trilayer	Si_4Al_2	AA'A"	4.128	2.390	2.439	2.515	0.175	0.802	119.46	339	No
		ABC	4.143	2.399	2.419	2.516	0.185	0.782	119.40	309	Yes
	Si_4N_2	AA'A"	2.911	1.763	2.384	2.508	0.533	1.861	111.27	-156	No
		ABC	2.865	1.751	2.433	2.807	0.574	2.267	109.78	-188	No
	Si_4P_2	AA'A"	3.641	2.321	2.365	2.283	0.984	0.890	103.32	-6	Yes
		ABC	3.665	2.330	2.356	2.292	0.974	0.880	103.74	-7	Yes

the interlayer distances $h_{\mathrm{Si-Si}}$ are slightly greater/smaller than the ones of pristine systems, indicating that the Si-Si covalent bonds are maintained (see table 4.1). We now move to the discussion regarding the possibility of synthesizing the $\mathrm{Si_2X_2}$ and $\mathrm{Si_4X_2}$ nanosheets.

4.1.2 Enthalpy of formation

We now analyze the values of the standard enthalpy of formation ΔH_f^0, per atom, described in the methodology, section 2.5). The values are displayed in table 4.1 and they were computed by

$$\Delta H_f^0 = \frac{E_t(\mathrm{Si}_y\mathrm{X}_2) - yE_t(\mathrm{Si}) - 2E_t(\mathrm{X})}{y+2}, \tag{4.1}$$

where $E_t(\mathrm{Si}_y\mathrm{X}_2)$ is the total energy of the 2D system, with ySi atoms and 2X atoms (X = B, N, Al, P), y being 2 and 4 for bilayers and trilayers, respectively. The $E_t(\mathrm{Si})$ and $E_t(\mathrm{X})$ are the total energies, per atom, of the respective Si and X standard states: the total energy of crystalline silicon in a diamond lattice, boron in a trigonal crystalline structure (β-boron), aluminum in a face-centered cubic crystalline structure, nitrogen in an isolated $\mathrm{N_2}$ molecule, and phosphorus in its black puckered orthorhombic layered structure.

We found that only the FLS nanosheets doped with substitutional N or P atoms have negative ΔH_f^0, where the exothermic reaction is likely due to the high reactivity of the silicene surface [104]. However, there are examples of 2D materials synthesized by endothermic processes ($\Delta H_f^0 > 0$), such as silicene (751 meV/atom) and graphene (70 meV/atom [21]) monolayers. Additionally, it has been proposed that it is easier to experimentally produce free-standing 2D materials when the ΔH_f^0 is under the threshold value of 200 meV/atom [60, 61, 105].

The systems doped with substitutional B or Al atoms have positive ΔH_f^0, with energies values ranging between the threshold (200 meV/atom) and the silicene monolayer enthalpy of formation (751 meV/atom), which is in good agreement with the literature [60, 106]. Nevertheless, besides the enthalpy of formation showing the

functionalized systems are energetically more favorable than the pristine silicene monolayer, the dynamic stability of these structures should be studied to check the possibility of synthesizing the Si_2X_2 and Si_4X_2 nanosheets.

4.1.3 Dynamic stability and elasticity

To study the dynamic stability of the structures we obtained the phonon dispersion curves through the density functional perturbation theory (see section 2.3), with the irreducible BZ sampled by an $8 \times 8 \times 1$ q-point mesh. A system is dynamically stable when it has only positive frequencies in the phonon dispersion curves and, hence, we found the FLS functionalized with P atoms are dynamically stable. On the other hand, silicene structures functionalized with B, Al, or N are dynamically stable only in some stacking configurations. Table 4.1 presents the stability of all structures investigated here based on that criterion (DS).

Figure 4.2 exhibits the phonon dispersion curves of the systems, where some are dynamically unstable since they present larger negative frequency values. However, the small negative frequency around the Γ valley in the ABC-Si_4B_2 system, shown in figure 4.2 (j), does not necessarily indicate that this sheet is unstable. This behavior, which is found in other 2D materials, has been generally associated with the difficulty in converging the out-of-plane ZA transverse acoustic mode [107,108]. Accordingly, we next computed the elastic constants of the stable systems to verify their mechanical stability, in which the Born stability criteria $C_{11} > 0$ and $C_{12} < C_{11}$ must be satisfied [58].

We used the strain-energy method, described in section 2.4, to determine the elastic properties of the systems. The C_{11} and C_{12} constants were obtained fitting a second-order polynomial to the data, equation (2.48). Here, we built a rectangular supercell with 8 and 12 atoms for the bilayers and trilayers, respectively, and applied two in-plane strains (ϵ), ranging from -1.5% to 1.5% with respect to the optimized cell parameters: (i) uniaxial deformation along the zigzag direction and (ii) biaxial planar deformation [57]. Table 4.2 displays the elastic constants C_{11}, C_{12}, and $C_{44} = (C_{11} - C_{12})/2$, as well as the Young modulus $Y^{2D} = (C_{11}^2 - C_{12}^2)/C_{11}$, and
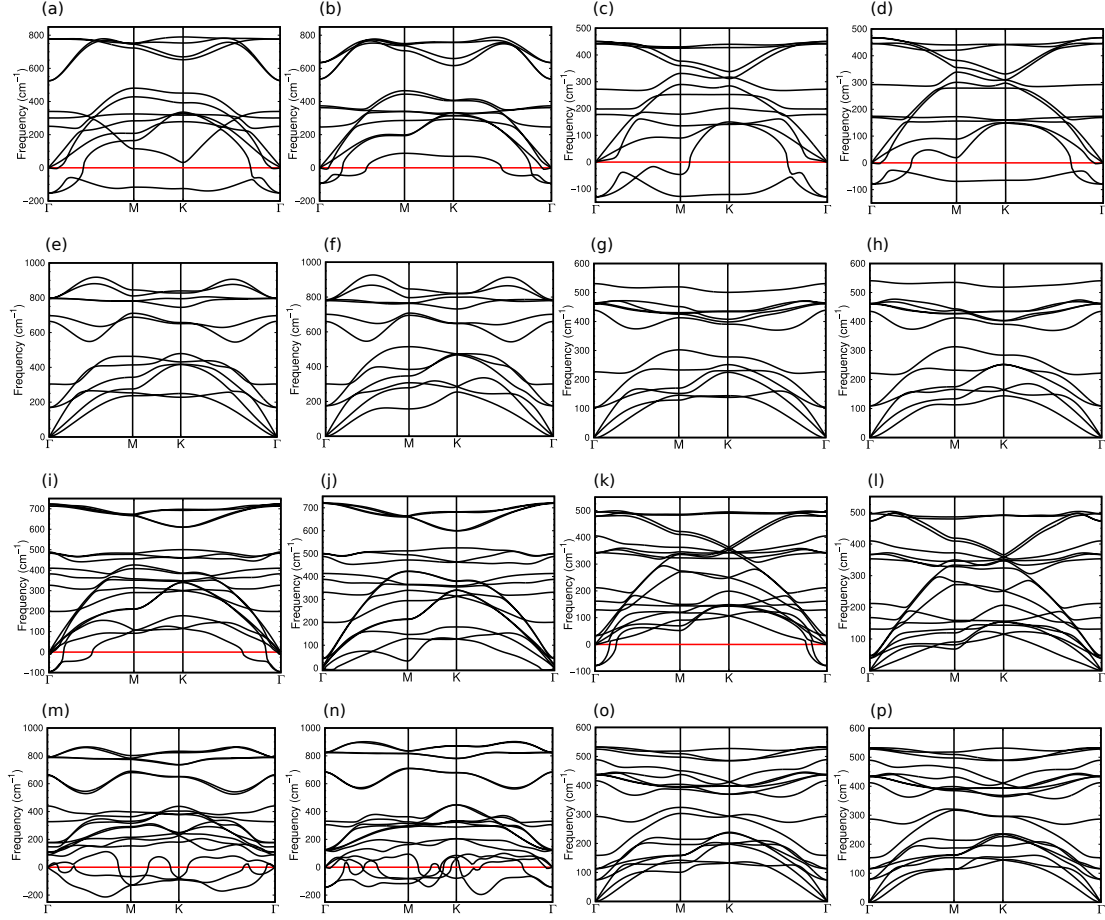
Figure 4.2: Phonon dispersion curves along the high symmetry directions of the irreducible BZ of the hexagonal lattice: (a) AA′-Si$_2$B$_2$, (b) AB-Si$_2$B$_2$, (c) AA′-Si$_2$Al$_2$, (d) AB-Si$_2$Al$_2$, (e) AA′-Si$_2$, (f) AB-Si$_2$N$_2$, (g) AA′-Si$_2$P$_2$, (h) AB-Si$_2$P$_2$, (i) AA′A″-Si$_4$B$_2$, (j) ABC-Si$_4$B$_2$, (k) AA′A″-Si$_4$Al$_2$, (l) ABC-Si$_4$Al$_2$, (m) AA′A″-Si$_4$N$_2$, (n) ABC-Si$_4$N$_2$, (o) AA′A″-Si$_4$P$_2$, (p) ABC-Si$_4$P$_2$. Reproduced from Paper III [28].

the Poisson ratio $\nu = C_{12}/C_{11}$.

Our results show that the dynamically stable systems also satisfy the Born criteria and, hence, are mechanically stable. We also observed that pristine FLS structures become more stable as they grow in thickness, i.e., the elastic constants and the Y^{2D} increase with the number of layers. Furthermore, all the systems investigated have a Poisson ratio ν lower than 0.5 except for the ABC-Si$_4$Al$_2$. Poisson ratio ν lower than 0.5 is a characteristic of isotropic systems [100] and has been observed

Table 4.2: Elastic constants C_{11}, C_{12}, and C_{44}, Youngs modulus Y^{2D}, and Poisson ratio ν of pristine FLS, Si_2X_2, and Si_4X_2 (X = B, N, Al, P) for the dynamically stable configurations. Elastic constants and Youngs modulus are given in N/m and the Poisson ratio is dimensionless. Reproduced from Paper III [28].

System	Structure	Stacking	C_{11}	C_{12}	C_{44}	Y^{2D}	ν
Monolayer	Si_2	—	69	19	25	64	0.28
Bilayer	Si_4	AA′	124	36	44	113	0.29
		AB	121	33	43	111	0.28
	Si_2N_2	AA′	296	83	106	273	0.28
		AB	278	83	97	252	0.30
	Si_2P_2	AA′	133	24	55	129	0.18
		AB	129	23	53	125	0.18
Trilayer	Si_6	AA′A	157	33	62	150	0.21
		ABC	167	43	62	156	0.25
	Si_4B_2	ABC	198	35	82	192	0.17
	Si_4Al_2	ABC	123	84	20	66	0.68
	Si_4P_2	AA′A″	182	38	72	174	0.21
		ABC	176	36	70	168	0.21

in 2D materials [101]. However, despite ABC-Si_4Al_2 presents ν value larger than 0.5 (0.68), this is close to values found in stretched silicene monolayer of 0.62 [109] and 0.75 [110].

Finally, we present the standard enthalpy of formation for all the dynamically stable structures in figure 4.3. The graphene is also included for comparison, where the enthalpy of formation was computed with respect to graphite using the optB88-vdW van der Waals density functional to describe the exchange-correlation energy [21]. Moreover, despite having enthalpies of formation greater than 200 meV, the pristine FLS nanosheets have been free-standing synthesized [33]. Accordingly, the comparison shows the feasibility of experimentally synthesizing, through different techniques, the dynamically stable systems investigated here.
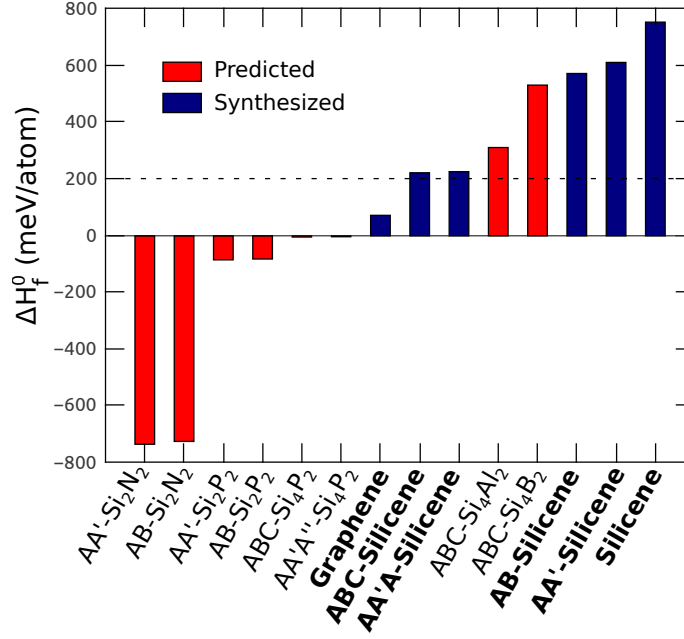
Figure 4.3: Standard enthalpy of formation, calculated using Eq. 4.1, for the dynamically stable systems. The horizontal dashed line illustrates the empirical threshold energy to experimentally synthesize free-standing 2D materials [60, 61, 105]. Reproduced from Paper III [28].

4.1.4 Electronic properties

The electronic band structures and the projected density of states (PDOS) of the dynamically stable Si_2X_2 and Si_4X_2 systems (X= B, N, Al, P), pristine silicene Si_2 monolayer, Si_4 bilayers, and Si_6 trilayers, are exhibit in figures 4.4 and 4.5. We can observe that the pristine silicene monolayer has zero band gap with a Dirac cone at the K-point in the BZ, and FLS nanosheets present metallic behavior. The results displayed in figure 4.4(a) for Si_2, figures 4.4(b) and (c) for Si_4, and figures 4.5(a) and (b) for Si_6, agree well with the ones reported in literature [25, 111–113]. Regarding functionalized FLS we found indirect band gap semiconductors and metallic systems. The indirect band gap semiconductors are the AA'-Si_2N_2, AB-Si_2N_2, AA'-Si_2P_2, and AB-Si_2P_2 doped bilayers, figures 4.4 (d)-(g), and the $AA'A''$-Si_4P_2 and ABC-Si_4P_2 doped trilayers, figures 4.5 (e) and (f). The metallic system are the ABC-Si_4B_2 and ABC-Si_4Al_2 trilayers, figures 4.5 (c) and (d).

79

Figure 4.4: Electronic band structures along the high-symmetry directions of the BZ (left panels) and projected density of states (PDOS) (right panels), obtained with the optB88-vdW approach for the exchange-correlation energy: (a) Si_2, (b) AA′-Si_4, (c) AB-Si_4, (d) AA′-Si_2N_2, (e) AB-Si_2N_2, (f) AA′-Si_2P_2, and (g) AB-Si_2P_2. The PDOS (states/eV) on the Si and X s-orbitals are in purple and blue, and on the Si and X p-orbitals are in red and green, respectively. E_v is the valence band top and E_F the Fermi energy. Reproduced from Paper III [28].

The B or Al (group-III) substitution keeps the metallic behavior of pristine silicene trilayers. However, the N and P (group-V) substitution transforms the pristine silicene bilayers and trilayers from metallic to semiconductor 2D materials. Accordingly, the number of valence electrons of the X atoms is the prevailing factor that determines the properties of the compounds. Moreover, the Dirac cone is not preserved in the Si_4X_2 systems, differing from the metallic pristine silicene trilayers, which is below the Fermi energy at the K-point for the AA′A stacking configuration,
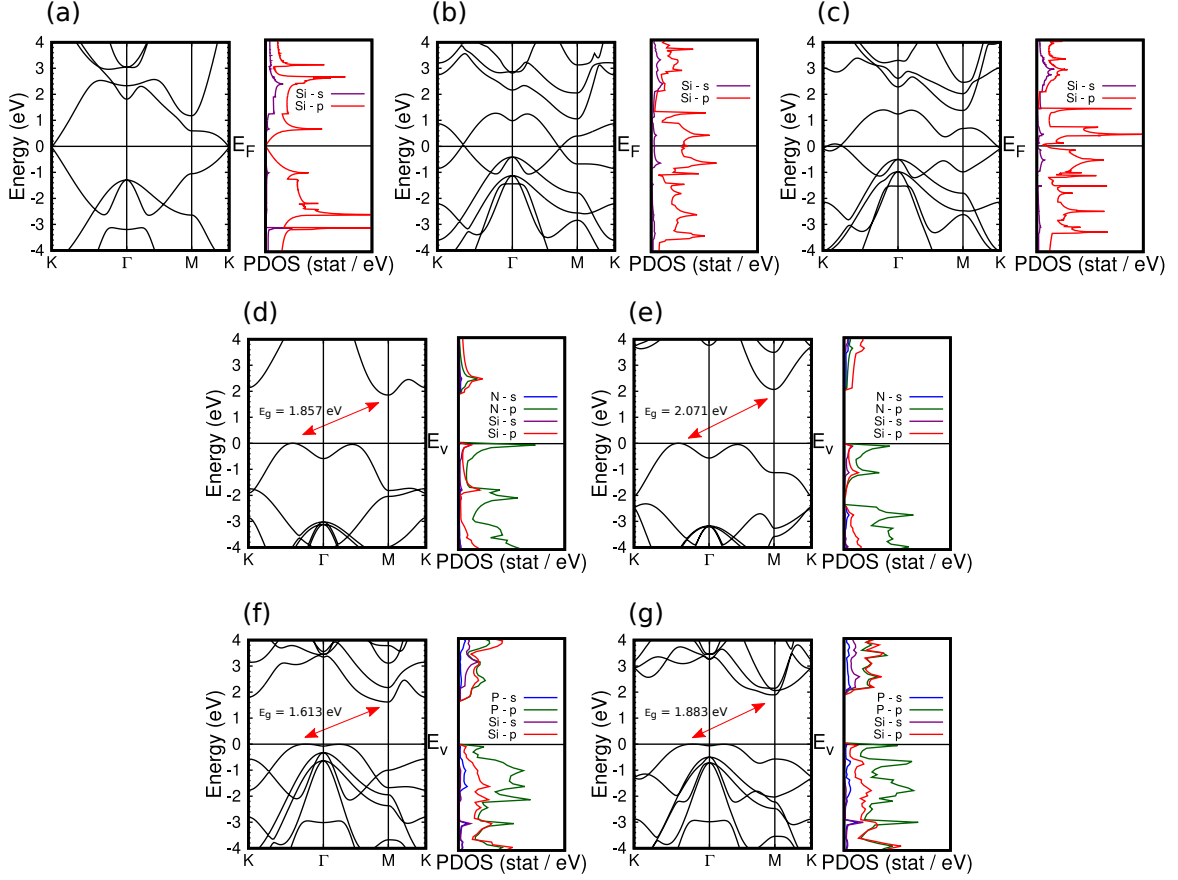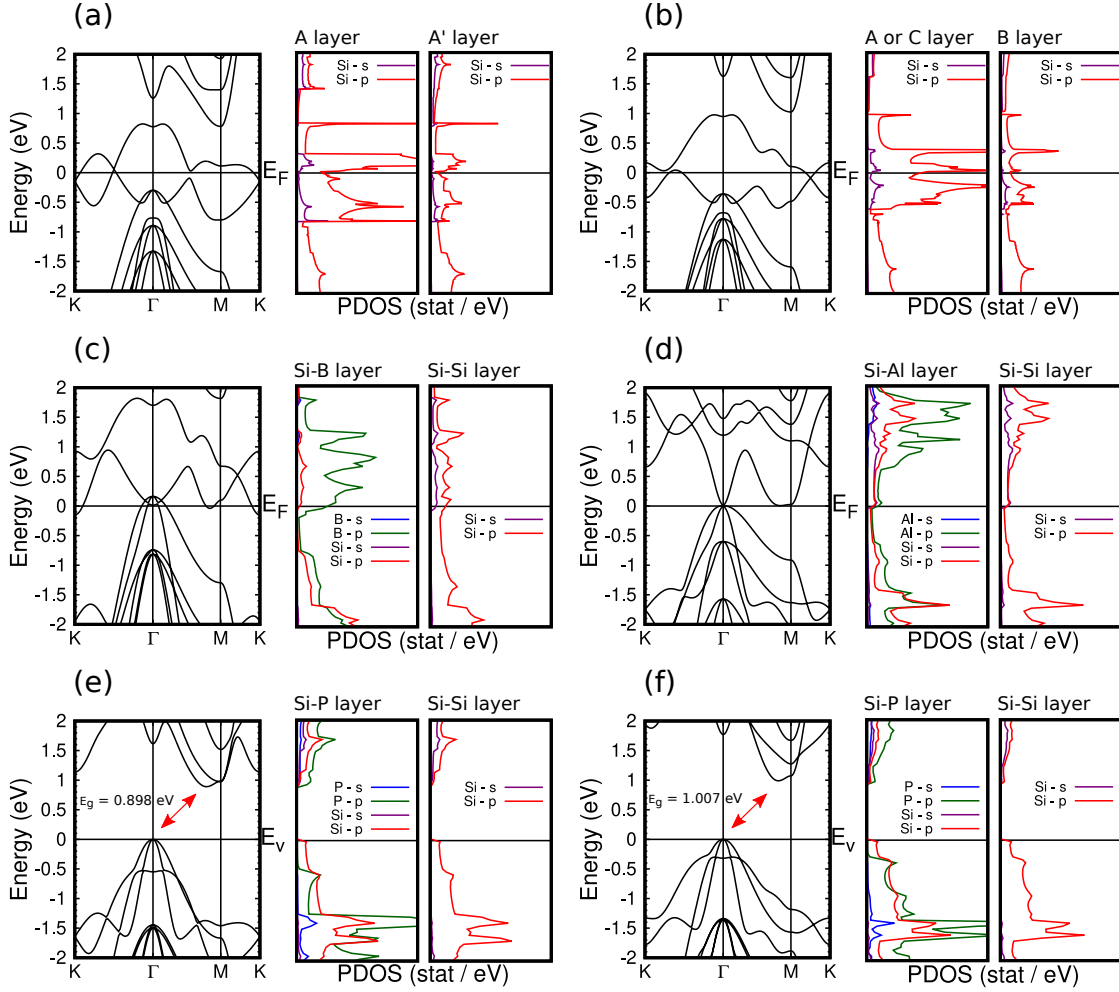
Figure 4.5: Electronic band structures along the high-symmetry directions of the BZ (left panels) and projected density of states (PDOS) (right panels), obtained with the optB88-vdW approach for the exchange-correlation energy: (a) AA′A-Si$_6$, (b) ABC-Si$_6$, (c) ABC-Si$_4$B$_2$, (d) ABC-Si$_4$Al$_2$, (e) AA′A″-Si$_4$P$_2$, and (f) ABC-Si$_4$P$_2$. The PDOS (states/eV) on the Si and X s-orbitals are in purple and blue, and on the Si and X p-orbitals are in red and green, respectively. E$_v$ is the valence band top and E$_F$ the Fermi energy. Reproduced from Paper III [28].

figure 4.5(a), and in the K-M direction for the ABC one, figure 4.5 (b) [111].

In table 4.3 we present the electronic band gaps E_g (E_g^{HSE06}) for AA′-Si$_2$N$_2$, AB-Si$_2$N$_2$, AA′-Si$_2$P$_2$, AB-Si$_2$P$_2$, AA′A″-Si$_4$P$_2$, and ABC-Si$_4$P$_2$. The gap values increased by about 1 eV (Si$_2$N$_2$), 0.6-0.7 eV (Si$_2$P$_2$), and 0.8 eV (Si$_4$P$_2$) when the

Table 4.3: Electronic properties of pristine and doped FLS, for the dynamically stable configurations: indirect electronic band gaps obtained with two different approximations for the exchange-correlation functional: optB88-vdW (E_g) and HSE06 (E_g^{HSE06}), given in eV. The table also displays the valence band maximum (VBM) and the conduction band minimum (CBM) high-symmetry point or direction (hexagonal BZ), and the atomic character of VBM and CBM. These parameters were obtained using the optB88-vdW approximation to describe the exchange-correlation energy. The systems with metallic behavior are also shown. Reproduced from Paper III [28].

System	Structure	Stacking	Classification	E_g	E_g^{HSE06}	VBM (character)	CBM (character)
Monolayer	Si$_2$	—	semimetal	0	—	—	—
	Si$_4$	AA'-Si$_4$	metal	—	—	—	—
		AB-Si$_4$	metal	—	—	—	—
Bilayer	Si$_2$N$_2$	AA'-Si$_2$N$_2$	semiconductor	1.857	2.905	K-Γ (Si-p, N-p)	M (Si-p, N-p)
		AB-Si$_2$N$_2$	semiconductor	2.071	3.091	K-Γ (Si-p, N-p)	M (Si-p)
	Si$_2$P$_2$	AA'-Si$_2$P$_2$	semiconductor	1.613	2.239	K-Γ (Si-p, P-p)	M (Si-p, P-p)
		AB-Si$_2$P$_2$	semiconductor	1.883	2.583	K-Γ (Si-p, P-p)	M (Si-p, P-p)
	Si$_6$	AA'A-Si$_6$	metal	—	—	—	—
		ABC-Si$_6$	metal	—	—	—	—
Trilayer	Si$_4$B$_2$	ABC-Si$_4$B$_2$	metal	—	—	—	—
	Si$_4$Al$_2$	ABC-Si$_4$Al$_2$	metal	—	—	—	—
	Si$_4$P$_2$	AA'A''-Si$_4$P$_2$	semiconductor	0.898	1.766	Γ (Si-p)	Γ-M (Si-p, P-p)
		ABC-Si$_4$P$_2$	semiconductor	1.007	1.837	Γ (Si-p)	Γ-M (Si-p, P-p)

HSE06 approach was used. We found the electronic band gap values of Si_2N_2 and Si_2P_2 functionalized bilayers are in good agreement with theoretical results reported in literature [114]. Table 4.3 also exhibits the high-symmetry point or direction of the valence band maximum (VBM) and conduction band minimum (CBM), and their atomic projected character.

Figures 4.4 (d)-(g) show that the bottom of the conduction band (M-point), and the top of the valence band (K-Γ direction) of the Si_2N_2 and Si_2P_2 semiconducting bilayers, have contributions mainly from the hybridization of the Si and X p-states (X = N, P), with prevailing X p-states character. Our results also agree with the literature since the top region of the valence band is highly degenerated with a Mexican-hat dispersion (quartic function) [114].

In figures 4.5 (e) and (f), we observe similar band structures and PDOS for the $AA'A''$-Si_4P_2 and ABC-Si_4P_2 semiconducting trilayers, with the VBM at the Γ-point and the CBM at the Γ-M direction. At the VBM the Si p-orbitals dominate and it is derived from the intermediate (non-doped) Si-Si layer and from the Si-P layer. However, there is also a contribution of the P p-states from the Si-P layer at the CBM. The PDOS exhibited in figures 4.5 (c) and (d) for the ABC-Si_4B_2 and ABC-Si_4Al_2 metallic systems, show that the Fermi level crosses three bands in the Γ-point region. Moreover, these band have contributions from the hybridization of the Si and X p-orbitals of the Si-X layer (X = B, Al), and from the Si s-states of the Si-Si layer. In the ABC-Si_4B_2, the Fermi level crossing around the K-point is mainly derived from the Si p-states of the Si-Si layer and from the B p-states of the Si-B layer.

Accordingly, these results suggest that it is possible to tune and control the FLS electronic structure by increasing the number of layers and, simultaneously, doping them to be used in specific applications, such as optoelectronic and thermoelectric devices.

4.1.5   Future outlook

Considering that functionalized nanostructures could serve as building blocks for the self-assembly of complex 3D systems [21, 23, 91, 115, 116], and van der Waals heterostructures based on silicon SiN were proposed for water oxidation applications and the SiP for photocatalytic water splitting [117], it is interesting to explore if those systems investigated in this thesis could be used as building blocks and how their properties would modify with different morphologies. Additionally, due to the wide band gap of the Si_2N_2 and Si_2P_2 bilayers, they have been considered for UV-light applications [114] and as thermoelectric materials at room temperature [118]. Therefore, we suggest futher investigation of the $AA'A''$-Si_4P_2 and ABC-Si_4P_2 trilayer nanosheets as thermoelectric materials and for UV-light applications, despite having narrower band gaps compared to Si_2P_2 bilayers.

Moreover, previous studies have shown that monolayer and few-layer silicene nanosheets are promising candidates for energy storage systems, such as lithium-ion batteries [33, 119]. Doping the silicene monolayer with different elements has also shown good performance for alkali metal ion batteries (AMIBs). In comparison to pristine silicene, for example, B/Al doped silicene has low diffusion barriers and a higher capacity for sodium-ion batteries (SIBs) and potassium-ion batteries (KIBs) [120]. Accordingly, the ABC-Si_4B_2 and ABC-Si_4Al_2 metallic trilayer structures are promising candidates for AMIBs applications since good electrical conductivity is one of the requirements for advantageous electrodes [121].

4.1.6   Conclusion

We performed an *ab initio* investigation on the structural, energetic, dynamic, elastic, and electronic properties of silicene bilayers and trilayers functionalized with group-III and group-V atoms in several stacking configurations. While group-III presented a metallic behavior on FLS, group-V maintained the semiconductor characteristics. Particularly, we found four new dynamically stable nanosheets. By analyzing the enthalpies of formation values and comparing them with the ones

of the pristine silicene and graphene, the best known 2D material, we show the feasibility of experimentally synthesizing them. We could identify several potential applications for those structures based on our results and previous studies of silicon-based nanosystems, such as in alkali-metal ion batteries, UV-light devices, and thermoelectric materials.

4.2 Al-functionalized few-layer silicene as ion battery anode material

In the previous section (Paper III), we investigated the few-layer silicene with several surface functionalizations and stacking configurations. We observed that the B and Al substitution keeps the metallic behavior of pristine silicene trilayers, making them good candidates to work as battery electrodes. Also, we noticed that the lattice parameter of the aluminum-doped silicene trilayer (ABC-Si_4Al_2) is larger than the pristine few-layer silicene and ABC-Si_4B_2. These properties can contribute to storing more ions and to a small volume expansion of the electrode material during the battery (re)charging, which are requirements for anodes with high specific capacity and cycling performance [121]. Therefore, we chose to study the ABC-
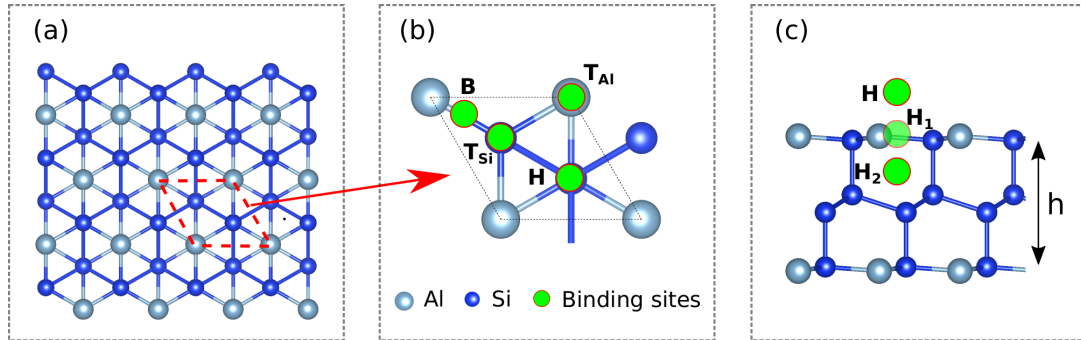
Figure 4.6: (a) Top view, (b) primitive cell, (c) side view of the ABC-Si_4Al_2 and the binding sites for Li-, Na-, and K-alkali metal atoms. The hollow, top, and bridge sites are represented respectively by H, T, and B symbols. The dashed lines indicate the unit cell limits. The blue and grey spheres represent respectively Si and Al atoms, while the green spheres represent the binding sites for adsorption of the alkali metal ions. Reproduced from Paper IV [30].

Si_4Al_2 nanolayer and its potential application as an AMIB anode. A schematic representation of the ABC-Si_4Al_2 structure is displayed in figure 4.6, where the optimized primitive cell parameters are $a = b = 4.143$ Å, with a thickness $h = 6$ Å.

4.2.1 Thermodynamic stability

Firstly, we explore the thermodynamic stability of this system as a function of temperature, showing that ABC-Si_4Al_2 system remains structurally stable up to 600 K. Accordingly, we used *ab-initio* molecular dynamics (AIMD) simulations, as implemented in the Vienna *ab-initio* simulation package (VASP) [64], using a 150-atoms supercell ($5 \times 5 \times 1$) with lattice parameters $a = b = 20.715$ Å, in order to allow possible structural reconstructions. The time step of the simulations was set to 1 fs and a Nose-Hoover thermostat (NVT) ensemble was employed to carry out the calculations at several temperatures (from 0 to 1000K) for 5 ps. Figures 4.7 (a) and (b) show, respectively, the total energy of the system at 300K and 600K during 5 ps. The system reaches thermal equilibrium and then the energy oscillates around an equilibrium value after about 1 ps. The figures also display a snapshot of the final structure, indicating that the system keeps its structural integrity with no broken bonds or defect formation. However, the system starts to present broken bonds at higher temperatures. Figure 4.7 (c) shows the total energy of the system at 1000K during 5 ps, as well as a snapshot of the final structure, indicating structural degradation.

In figure 4.7 (d), it is presented the average total energy, as a function of temperature, of the last 2 ps of the simulations. It can be observed that the average total energy increases linearly with temperature below 600K and, according to the virial theorem, the average kinetic and potential energies are very close, indicating structural integrity. Over 600K, the average total energy increases faster with temperature, showing that there are broken bonds, defects, and some atomic diffusion.

Those results demonstrate that the ABC-Si_4Al_2 structure is considerably stable for temperatures up to 600K, with the atoms oscillating around their crystalline equilibrium positions, without breaking bonds, and could be used as electrodes for
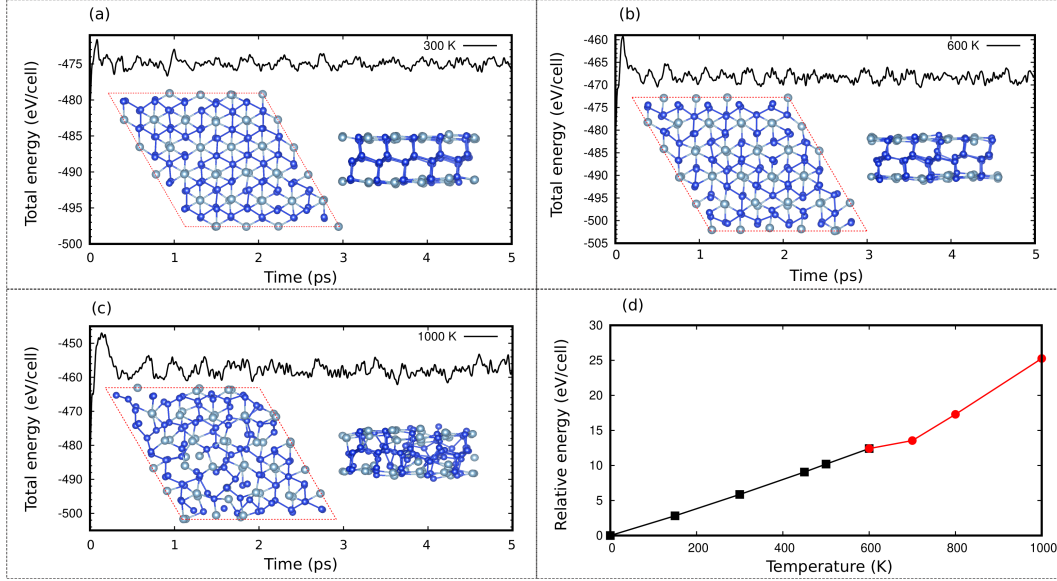
Figure 4.7: Total energy over 5 ps during AIMD simulations at (a) 300K, (b) 600K, (c) 1000K, and the respective final structures snapshots (top and side views) at the end of the simulation; (d) average total energy variation, relative to the value at $T = 0$K, of the last 2 ps of the simulations, as a function of temperature. The coloring of spheres is consistent with those in figure 4.6. Reproduced from Paper IV [30].

applications below that threshold. Nevertheless, the nanosheet suffers considerable structural degradation at higher temperatures, and close to 1000K, they are unsuitable for those applications.

4.2.2 Ion adsorption properties

After showing that the ABC-Si_4Al_2 compound preserves its structural stability up to 600K, the next step is to verify whether it can adsorb and incorporate the alkali metal ions (Li, Na, K). Therefore, a $3 \times 3 \times 1$ supercell was built, with optimized lattice parameters of $a = b = 12.429$ Å, corresponding to a chemical stoichiometry of ABC-$M_1Si_{36}Al_{18}$ (M = Li, Na, K). This supercell is large enough for simulating one alkali atom adsorbed/inserted in the system while avoiding interaction among images.

87

We started studying the adsorption of alkali metals in several high-symmetry binding sites on the trilayer surface, as shown in figure 4.6 (b), and subsequently in two sites inside the trilayer structure, as presented in figure 4.6 (c). We considered the hollow site (H) at the center of a hexagon, the top site (T) directly above each atom, and the bridge site (B) at the midpoint of a Si-Al bond. The bulk interstitial adsorption was also considered in two sites: the layer hollow site (H_1), at the center of a hexagonal ring, and the interstitial hollow site (H_2), inside the structure at the center of a hexagon, as presented in figure 4.6 (c).

The alkali atoms moved from the B to the T_{Al} site and from the H_1 to the H_2 one after performing structural optimization, indicating that the ions are unlikely to be adsorbed at the B and H_1 sites. Accordingly, we calculated the average adsorption energy (E_{ads}), described in section 2.7, at the remaining sites with the following equation

$$E_{ads}(\text{M}) = \Big[E_t\big(\text{Si}_4\text{Al}_2\text{M}_n\big) - E_t\big(\text{Si}_4\text{Al}_2\big) - nE_t\big(\text{M}\big)\Big]\Big/n\,, \qquad (4.2)$$

where $E_t\big(\text{Si}_4\text{Al}_2\text{M}_n\big)$ is the total energy of the host nanosheet with nM alkali ad-atoms, $E_t\big(\text{Si}_4\text{Al}_2\big)$ is the total energy of an isolated ABC-Si_4Al_2 trilayer, and $E_t\big(\text{M}\big)$ is the total energy, per atom, of the M alkali metal in a body-centered cubic crystalline structure. Herein, a negative E_{ads} value indicates that the site is energetically favorable for adsorption. The obtained E_{ads} are presented in table 4.4, in which the negative values are in the same range as those in silicene-based materials, previously reported in the literature as potential candidates for anodes in AMIBs [33, 120, 122].

Regarding adsorption sites with negative E_{ads}, the H site is the most energetically favorable to adsorb either Li-, Na-, or K-atoms with $E_{ads}(\text{K})$ (-0.681 eV) $< E_{ads}(\text{Li})$ (-0.483 eV) $< E_{ads}(\text{Na})$ (-0.291 eV). Some investigations have also observed that the H site is also the most favorable, as we found, however in pure single-layer silicene, for Li- and Na-ions adsorption [31, 123]. Considering the T sites, the average adsorption energies for both Li- and Na-ions are positive, indicating that they are not suitable for adsorption. However, we found negative E_{ads} for K-ion at T_{Al} and T_{Si}, with values of -0.481 eV and -0.279 eV, respectively, showing these sites are

Table 4.4: Adsorption properties of alkali metal atoms M (M = Li, Na, K) in ABC-$M_1Si_{36}Al_{18}$ host structure. The table displays the average adsorption energy E_{ads} (in eV), the charge transfer ΔQ (in $|e|$), and the equilibrium distances d_M (in Å) between the adatom and the closest surface atom in the system. Reproduced from Paper IV [30].

Atom	Site	E_{ads}	ΔQ	d_M
Li	H	-0.483	0.859	1.177
Li	T_{Al}	0.009	–	–
Li	T_{Si}	0.378	–	–
Li	H_2	-0.470	0.836	0.878
Na	H	-0.291	0.811	1.905
Na	T_{Al}	0.018	–	–
Na	T_{Si}	0.214	–	–
Na	H_2	0.871	–	–
K	H	-0.681	0.803	2.423
K	T_{Al}	-0.481	0.818	3.105
K	T_{Si}	-0.279	0.826	3.072
K	H_2	2.200	–	–

favorable positions for adsorption of K-atoms. Finally, we could observe that there is not enough space in H_2 site to host Na- or K-ions due to the alkali metal atomic (ionic) radius, hence this site is only energetically favorable for Li-ion adsorption, with $E_{ads} = -0.470$ eV. Among all the ABC-$M_1Si_{36}Al_{18}$ systems studied here, we found the K-ions can be adsorbed at several sites of the ABC-Si_4Al_2 host and presented the lowest values of E_{ads}, suggesting this system is the most promising to work in ion batteries, i.e., as an anode in KIBs.

In table 4.4, we also exhibited the vertical distance (in the z-direction) between the adatom and the closest neighboring surface atom (d_M) for the energetically favorable adsorption sites. We found $d_K > d_{Na} > d_{Li}$ for the adsorption sites on the surface, showing d_M increases with the increasing atomic (ionic) radius and mass of the adatoms. Additionally, we also computed the charge transfer (ΔQ) from the ions toward the ABC-Si_4Al_2 host, using the Bader analysis presented in section 2.9.

The valence charge of the ions is almost fully transferred to the Si_4Al_2 host, with ΔQ values around $+0.8\ |e|$, indicating the ionization of the adatoms.

4.2.3 Ion diffusion properties

The ion mobility is related to the charge/discharge rates of the AMIBs [35]. Therefore, we next investigate the diffusion of the alkali metal atoms on ABC-Si_4Al_2. Herein, we built a $3 \times 3 \times 1$ supercell and used the NEB method (section 2.8), where the initial and final configurations are the most energetically favorable sites (two H adjacent ones).

Figure 4.8 (a) illustrates the three different high-symmetry pathways considered on the ABC-Si_4Al_2 surface. Herein, a single alkali atom moves from an H site to another H site, passing through a B, a T_{Si}, or T_{Al} site for Path 1, Path 2, or Path 3, respectively. However, at the end of NEB calculations, we found the ions diffuse through the top of the aluminum/silicon sites (Path 2 and Path 3). Moreover, since the E_{ads} is negative in the H_2 site for the Li atom, we considered an additional path (Path 4) for the Li atom, moving it from the H to the H_2, as shown in figure 4.8 (b).

We present in figures 4.8 (c), (d), and (e) the energy profiles along different paths for Li, Na, and K ions, respectively. The diffusion coordination 4 corresponds to the T_{Si} site on Path 2, the T_{Al} site on Path 3, and the H_1 site on Path 4. In table 4.5 a comparison can be done among the Li, Na, and K ions diffusion barriers values in the ABC-Si_4Al_2 host with the values found in other materials, that have been proposed as potential candidates to work as AMIBs anodes. Regarding Path 3, we found migration energy barriers of 0.53, 0.32, and 0.22 eV for Li, Na, and K atoms, respectively. These values are similar to the ones in commercial anode materials based on graphite and TiO_2, as well as other silicon-based systems, showed in Table 4.5.

Furthermore, we estimated the diffusion constant (D) of an alkali metal atom using the following Arrhenius equation [124]

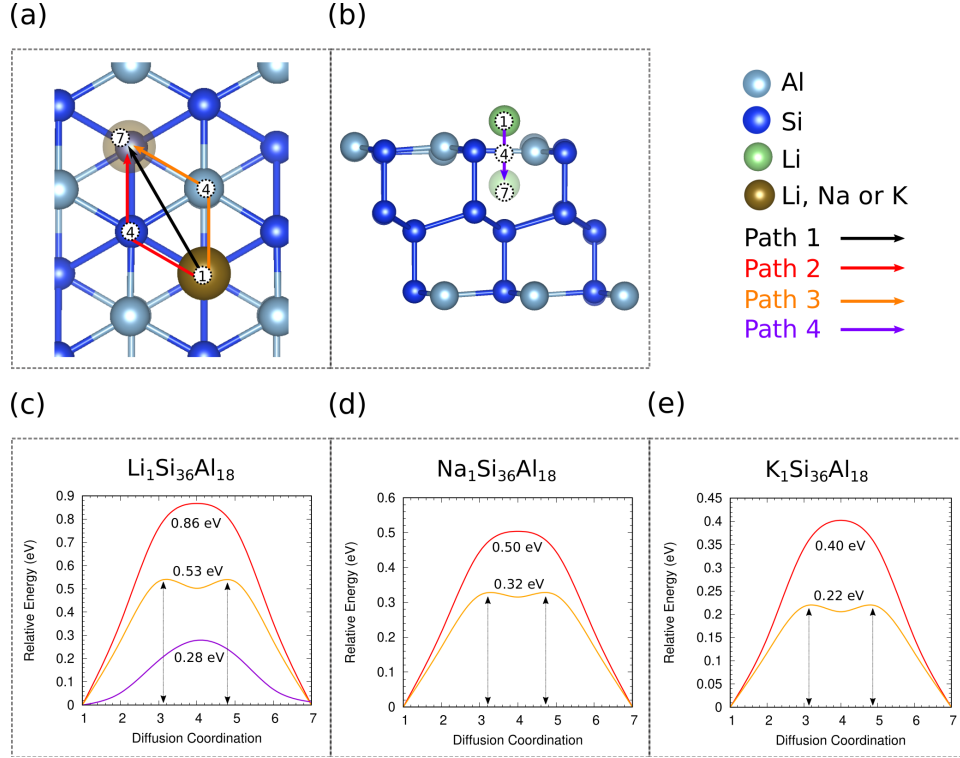$$D \sim exp\left(-\frac{E_b}{k_B T}\right),\qquad(4.3)$$

Figure 4.8: (a) Top and (b) side view of the ABC-Si_4Al_2 structure, indicating the binding sites (diffusion coordination 1, 4 and 7) and paths for Li/Na/K adatoms. The black, red, and orange arrows in (a) and the purple one in (b), represent the high-symmetry paths explored here (paths 1, 2, 3, and 4, respectively, as discussed in the text). The figure also shows the energy barriers associated with the diffusion of (c) Li, (d) Na, and (e) K in ABC-Si_4Al_2. The grey, blue, and brown spheres represent the Al, Si, and alkali metal ions (Li, Na, K), respectively. Moreover, in (b) the green spheres represent the Li ion. Reproduced from Paper IV [30].

where E_b and k_B are the diffusion barrier and the Boltzmann constant, respectively, and T is the environment temperature. At room temperature, the estimate diffusion constant of Path 3 are more than 10^3 times faster than that of Path 2 for Li, Na, and K ion. Additionally, we verify that the K mobility on ABC-Si_4Al_2, in Path 3, is as fast as in commercial graphite anodes, ensuring that we should expect good high-rate performance for the ABC-Si_4Al_2 as the anode material, primarily in KIBs.

Table 4.5: Diffusion barrier energy (E_b), in eV, specific theoretical capacity (C), in mAh/g, and average open-circuit voltage (OCV), in V, for Li, Na, K ions in ABC–Si$_4$Al$_2$ trilayer system, as compared to results reported in the literature for other potential candidates to work as AMIB anodes. Herein, the C and the average OCV values are computed for the Li$_4$Si$_4$Al$_2$, Na$_2$Si$_4$Al$_2$, and K$_2$Si$_4$Al$_2$ systems. Reproduced from Paper IV [30].

Anode material	Diffusion barrier energy (E_b)			Theoretical capacity (C)			Open-circuit voltage (OCV)		
	Li	Na	K	Li	Na	K	Li	Na	K
ABC-Si$_4$Al$_2$	0.53-0.86	0.32-0.50	0.22-0.40	645	322	322	0.49	0.16	0.14
Graphite	0.22-0.40[a]			372[b]		279[c]	0.11[d]		
TiO$_2$	0.35-0.65[d]	0.52[e]		200[f]			1.5-1.8[d]		
Silicene	0.23[g]	0.16[h]	0.14[i]	954[h]	954[i]			0.30-0.50[i]	
c-silicene				721[j]		180[k]			
VS$_2$	0.22[d]	0.62[l]		466[d]	233[l]		0.93[d]	1.32[l]	
AlSi$_3$ [120]		0.29	0.17		1928	964			
Si$_3$C [122]	0.47	0.34	0.18	1394	1115	836	0.58	0.50	0.71
Si$_2$BN [125]	0.48	0.32		1158	933	836	0.46	0.29	

[a]Reference [126]. [b]Reference [11]. [c]Reference [12]. [d]Reference [127]. [d]References [128–130]. [e]Reference [128]. [f]Reference [129]. [g]Reference [31]. [h]Reference [32]. [i]Reference [131]. [j]Reference [33]. [k]Reference [34]. [l]Reference [132].

4.2.4 Average open-circuit voltage and theoretical capacity

To estimate the maximum voltage available for a battery, i. e., open-circuit voltage (OCV), and the theoretical capacity (C), described in section 2.7, we explored the average adsorption energy (E_{ads}) as a function of the number of Li, Na, or K atoms adsorbed on ABC-Si$_4$Al$_2$.

We placed the adatoms in the most favorable adsorption positions and investigated the configurations: ABC-Li$_x$Si$_4$Al$_2$, ABC-Na$_y$Si$_4$Al$_2$, and ABC-K$_y$Si$_4$Al$_2$, with $x = 0.11, 1, 2, 3, 4$ and $y = 0.11, 1, 2$. The $x = 0.11$ concentration corresponds to single-side adsorption of M$_1$ alkali metal adatom in the H site of a 3×3×1 supercell (ABC-M$_1$Si$_{36}$Al$_{18}$). In figures 4.9 and 4.10 (a)-(h), we present the average adsorption energies and the corresponding optimized structures, respectively.

In the range explored here, figure 4.9 shows the average adsorption energies of all ions decrease in the $0 < x < 3$ interval due to the repulsion force between neighboring atoms. However, owing to the effects of the structural change, the average adsorption increases when $x > 3$ for the Li ion. [133]. Moreover, the figure presents the E_{ads} for Li, Na, and K remained negative, which indicates the ABC-
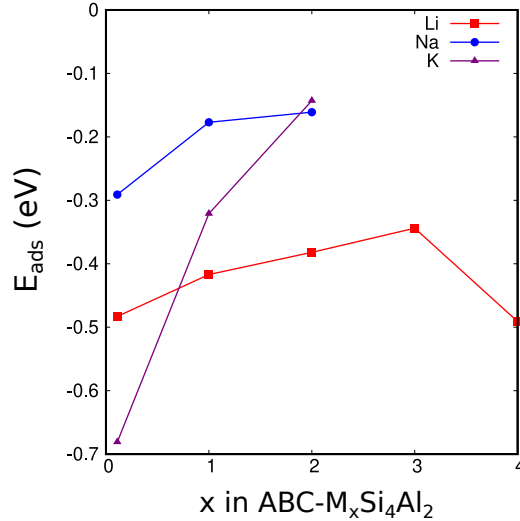

Figure 4.9: Average adsorption energies (E_{ads}) as function of alkali metal atom M concentration values (x) in ABC-M$_x$Si$_4$Al$_2$ (M = Li, Na, K). Reproduced from Paper IV [30].

Si_4Al_2 is a suitable anode material for AMIBs.

The single-side surface adsorption of M_1 adatom on the ABC-Si_4Al_2, with the H site fully covered by Li, Na, or K atoms (ABC-$M_1Si_4Al_2$), are exhibited in figures 4.10 (a), (e), and (g). The double-sided surface adsorption with the H site fully covered (ABC-$M_2Si_4Al_2$) are shown in figures 4.10 (b), (f), and (h). Additionally, figures 4.10 (c) and (d) report the resulting configurations of ABC-$Li_3Si_4Al_2$ and ABC-$Li_4Si_4Al_2$ systems, respectively. The ABC-$Li_3Si_4Al_2$ with all H_2 positions fully loaded and one surface side with all H sites fully covered by Li atoms is the most stable configuration.

| (a) | $Li_1Si_4Al_2$ | (b) | $Li_2Si_4Al_2$ | (c) | $Li_3Si_4Al_2$ | (d) | $Li_4Si_4Al_2$ |

| (e) | $Na_1Si_4Al_2$ | (f) | $Na_2Si_4Al_2$ | (g) | $K_1Si_4Al_2$ | (h) | $K_2Si_4Al_2$ |

● Si ○ Al ● Li ● Na ● K
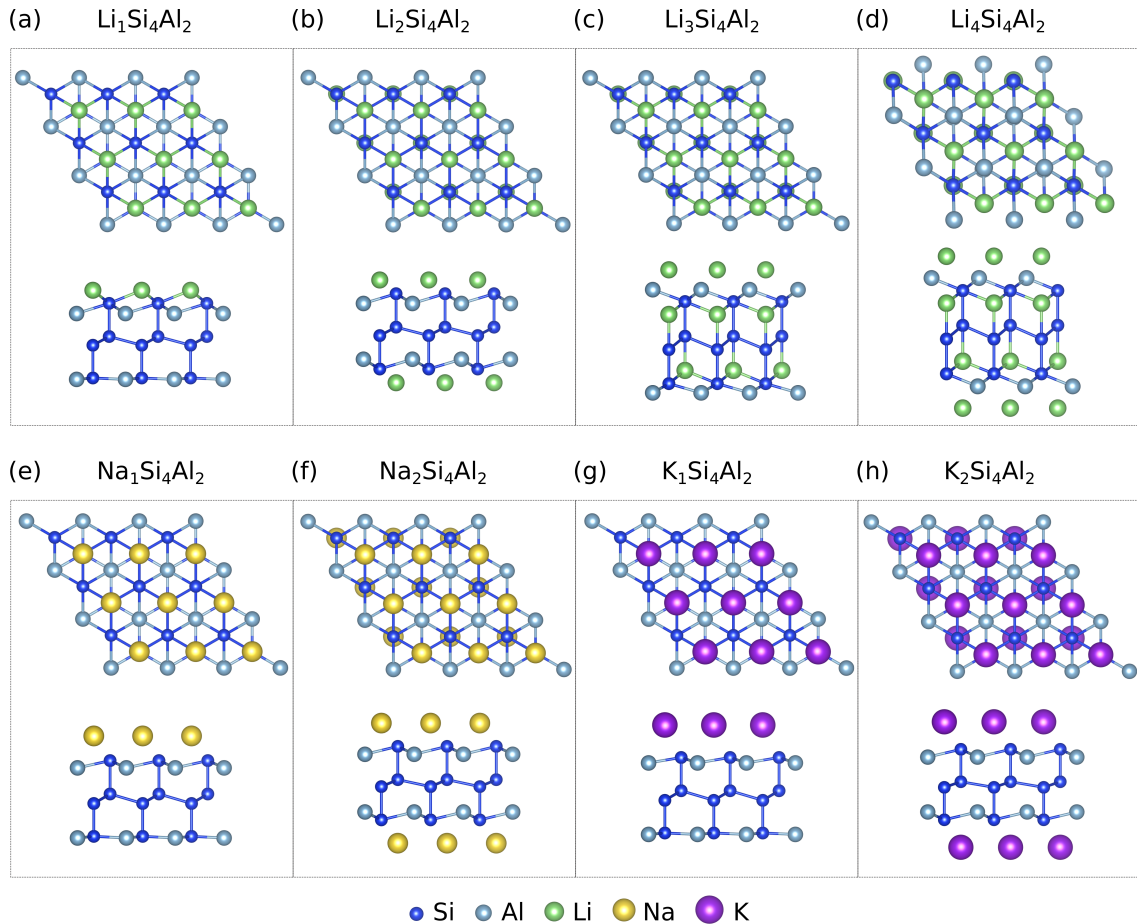
Figure 4.10: ABC-$M_xSi_4Al_2$ (M = Li, Na, K) optimized structures for several alkali metal ion concentration values (x). Reproduced from Paper IV [30].

Herein, we estimated the average OCV and the C for the full-loaded structure, i. e., the $Li_4Si_4Al_2$, $Na_2Si_4Al_2$, and $K_2Si_4Al_2$ systems. In Table 4.5, we compared our calculated average OCV with other candidates for anodes, in which the low voltage values that we found are desirable characteristics for anode electrodes [5]. We also presented the theoretical capacity of the ABC-Si_4Al_2 in Table 4.5. The Li capacity of 645 mAh/g for the ABC-Si_4Al_2 system is slightly smaller than an experimental value of 721 mAh/g for the pristine crystalline silicene as an anode for LIB [33]. Nevertheless, the K capacity of 322 mAh/g for the ABC-Si_4Al_2, which is the same value for Na one, is higher than pristine crystalline silicene as an anode for KIB (180 mAh/g) [34]. Moreover, the Li/Na/K capacity values of the ABC-Si_4Al_2 are higher than the commercial anode materials, such as graphite and TiO_2.

The crystalline silicene mentioned above appears structurally similar to the pristine silicene trilayers bonded covalently investigated in section 4.1. The crystalline silicene presents an experimental thickness of $\approx$ 6.5 Å and lattice parameter of $\approx$ 3.4 Å [33,34]. We obtained a value of $\approx$ 7.0 Å for the thickness and 3.858 Å for the lattice parameter [28]. Herein, the larger lattice parameter (4.143 Å) and the smaller thickness (6.0 Å) of the ABC-Si_4Al_2 could be the reason for the higher capacity of K when compared to crystalline silicene. Accordingly, the ABC-Si_4Al_2 exhibits a good theoretical capacity for alkali metal ion storage, primarily for KIBs.

4.2.5   Conclusion

In summary, we investigated the ABC-Si_4Al_2 as a potential anode material for Li, Na, and K ion batteries. In section 4.1, we found that this structure is dynamically and mechanically stable, and herein we showed that ABC-Si_4Al_2 is also thermodynamically stable up to 600K. The estimated surface diffusion barriers, average OCV, and specific capacity values are similar to the commercial anode materials, such as graphite and TiO_2. Moreover, we compared the estimated capacity with the experimental values of pristine crystalline silicene and found a slightly smaller capacity for LIBs and a higher one for KIBs. Therefore, the ABC-Si_4Al_2 provides good theoretical capacity and low average open-circuit voltage, suggesting aluminum-doped few-

layer silicene is a potential material for anode batteries, primarily for SIBs and KIBs. Finally, the few-layer silicon-based systems functionalized with different atomic elements could be a strategy for developing novel electrodes for AMIBs.

5. Concluding remarks

> Men make their own history, but they do
> not make it as they please.
>
> *Karl Marx*

To conclude, we performed an *ab initio* investigation on the physical properties of 2D diamond-like functionalized nanosheets to find novel materials for alkali metal ion batteries. In chapter 3, we studied carbon-based systems functionalized with nitrogen and boron atoms, identifying six dynamically stable structures made of two graphene layers (NCCN, NCNC, and NCCB) and four stable nanosheets built with three graphene layers (C_4N_2 and C_4B_2). According to their electronic structures, the discovered systems are semiconductors and insulators. Therefore, these nanosheets are not entirely suitable for applications associated with battery electrodes. Accordingly, we explored the potential use of NCCN, NCNC, and NCCB 2D structures as nanoscale two-dimensional building blocks for the self-assembly of 3D structures, where the NCCB bilayer appears as the best choice for a building block because of the resulting three-dimensional crystals. Moreover, the C_4X_2 (X = N or B) nanosheets presented stiffness similar to the diamond, a wide indirect band gap for the C_4N_2 and a narrow direct band gap for the C_4B_2 when compared with PD made of 3 graphene layers. We are currently investigating their potential application.

In chapter 4, we studied the few-layer silicene nanosheets made of two and three layers vertically combined, functionalized with boron, nitrogen, aluminum, or phosphorus atoms. Based on the results of the enthalpies of formation, phonon dis-

persion spectra, and Born stability criteria, we found four new types of systems that are dynamically stable and experimentally accessible, with enthalpy of formation lower than the one of pristine silicene monolayer. The predicted ABC-Si_4B_2 and ABC-Si_4Al_2 structures exhibited metallic behavior, while the AA′A″-Si_4P_2 and ABC-Si_4P_2 were semiconducting systems. Accordingly, we suggest that further investigations could explore both Si_4P_2 systems in thermoelectric and UV-light applications. Moreover, since good electrical conductivity is one of the requirements for advantageous electrodes and silicene is a promising candidate for energy storage systems, the ABC-Si_4B_2 and ABC-Si_4Al_2 metallic nanosheets are good candidates for AMIBs applications. Therefore, we investigated the ABC-Si_4Al_2 as a potential anode material for Li, Na, and K ion batteries.

Finally, we showed that the ABC-Si_4Al_2 is also thermodynamically stable up to 600K and investigated then the adsorption and diffusion properties of alkali metal ions (Li, Na, K) on it. The ABC-Si_4Al_2 exhibited surface diffusion barriers, average OCV, and specific capacity similar to the commercial anode materials, such as graphite and TiO_2. Moreover, we compared the calculated theoretical capacity values with the experimental ones of pristine crystalline silicene, which exhibits excellent performance as an anode in lithium-ion and potassium-ion batteries, finding a slightly smaller Li capacity and a higher one for KIBs. The aluminum-doped few-layer silicene is a potential material for anode batteries, with good high-rate performance and theoretical capacity for alkali metal storage (Li, Na, K), primarily for SIBs and KIBs. Furthermore, the functionalized few-layer silicon-based systems could be a route to developing novel electrodes for AMIBs.

The physical properties of 2D diamond-like nanosheets may vary considerably depending on the synthesis methods and functionalization, where the origin of all those different properties is still an open issue, despite recent experimental and theoretical investigations. Accordingly, we hope this thesis might contribute to and encourage future studies to explore this fascinating scientific field.

References

[1] Krista F Myers, Peter T Doran, John Cook, John E Kotcher, and Teresa A Myers. Consensus revisited: quantifying scientific agreement on climate change and climate expertise among earth scientists 10 years later. *Environmental Research Letters*, 16(10):104030, 2021.

[2] Mark Lynas, Benjamin Z Houlton, and Simon Perry. Greater than 99% consensus on human caused climate change in the peer-reviewed scientific literature. *Environmental Research Letters*, 16(11):114005, 2021.

[3] Tasso Rezende De Azevedo, Ciniro Costa Junior, Amintas Brandão Junior, Marcelo dos Santos Cremer, Marina Piatto, David Shiling Tsai, Paulo Barreto, Heron Martins, Márcio Sales, Tharic Galuchi, et al. Seeg initiative estimates of brazilian greenhouse gas emissions from 1970 to 2015. *Scientific Data*, 5(1):1–43, 2018.

[4] Hannah Ritchie, Max Roser, and Pablo Rosado. CO_2 and greenhouse gas emissions. *Our World in Data*, 2020. https://ourworldindata.org/co2-and-greenhouse-gas-emissions.

[5] Jianmin Ma, Yutao Li, Nicholas S Grundish, John B Goodenough, Yuhui Chen, Limin Guo, Zhangquan Peng, Xiaoqun Qi, Fengyi Yang, Long Qie, et al. The 2021 battery technology roadmap. *Journal of Physics D: Applied Physics*, 54(18):183001, 2021.

[6] Bo Xu, Danna Qian, Ziying Wang, and Ying Shirley Meng. Recent progress in cathode materials research for advanced lithium ion batteries. *Materials Science and Engineering R: Reports*, 73(5-6):51–65, 2012.

[7] Ekaterina Pomerantseva and Yury Gogotsi. Two-dimensional heterostructures for energy storage. *Nature Energy*, 2(7):17089, 2017.

[8] Jang-Yeon Hwang, Seung-Taek Myung, and Yang-Kook Sun. Sodium-ion batteries: present and future. *Chemical Society Reviews*, 46(12):3529–3614, 2017.

[9] Ranjusha Rajagopalan, Yougen Tang, Xiaobo Ji, Chuankun Jia, and Haiyan Wang. Advancements and challenges in potassium ion batteries: a comprehensive review. *Advanced Functional Materials*, 30(12):1909486, 2020.

[10] Nuria Tapia-Ruiz, A Robert Armstrong, Hande Alptekin, Marco A Amores, Heather Au, Jerry Barker, Rebecca Boston, William R Brant, Jake M Brittain, Yue Chen, et al. 2021 roadmap for sodium-ion batteries. *Journal of Physics: Energy*, 3(3):031503, 2021.

[11] Simon Schweidler, Lea de Biasi, Alexander Schiele, Pascal Hartmann, Torsten Brezesinski, and Jurgen Janek. Volume changes of graphite anodes revisited: a combined operando x-ray diffraction and in situ pressure analysis study. *The Journal of Physical Chemistry C*, 122(16):8829–8835, 2018.

[12] Zelang Jian, Wei Luo, and Xiulei Ji. Carbon electrodes for K-ion batteries. *Journal of the American Chemical Society*, 137(36):11566–11569, 2015.

[13] Chaoliang Tan, Xiehong Cao, Xue-Jun Wu, Qiyuan He, Jian Yang, Xiao Zhang, Junze Chen, Wei Zhao, Shikui Han, Gwang-Hyeon Nam, et al. Recent advances in ultrathin two-dimensional nanomaterials. *Chemical Reviews*, 117(9):6225–6331, 2017.

[14] Biao Chen, Dongliang Chao, Enzuo Liu, Mietek Jaroniec, Naiqin Zhao, and Shi-Zhang Qiao. Transition metal dichalcogenides for alkali metal ion batteries:

engineering strategies at the atomic level. *Energy & Environmental Science*, 13(4):1096–1131, 2020.

[15] Zhi-Qiang Wang, Tie-Yu Lü, Hui-Qiong Wang, Yuan Ping Feng, and Jin-Cheng Zheng. Review of borophene and its potential applications. *Frontiers of Physics*, 14(3):1–20, 2019.

[16] Kostya S Novoselov, Andre K Geim, Sergei V Morozov, D Jiang, Y Zhang, Sergey V Dubonos, Irina V Grigorieva, and Alexandr A Firsov. Electric field effect in atomically thin carbon films. *Science*, 306(5696):666–669, 2004.

[17] Andre K Geim and Konstantin S Novoselov. The rise of graphene. *Nature Materials*, 6(3):183–191, 2007.

[18] Yang Gao, Tengfei Cao, Filippo Cellini, Claire Berger, Walter A De Heer, Erio Tosatti, Elisa Riedo, and Angelo Bongiorno. Ultrahard carbon film from epitaxial two-layer graphene. *Nature Nanotechnology*, 13(2):133–138, 2018.

[19] Andre K Geim and Irina V Grigorieva. Van der Waals heterostructures. *Nature*, 499(7459):419, 2013.

[20] Yongji Gong, Junhao Lin, Xingli Wang, Gang Shi, Sidong Lei, Zhong Lin, Xiaolong Zou, Gonglan Ye, Robert Vajtai, Boris I Yakobson, et al. Vertical and in-plane heterostructures from WS_2/MoS_2 monolayers. *Nature Materials*, 13(12):1135, 2014.

[21] Bruno Ipaves, João F Justo, and Lucy V C Assali. Carbon-related bilayers: Nanoscale building blocks for self-assembly nanomanufacturing. *The Journal of Physical Chemistry C*, 123(37):23195–23204, 2019.

[22] Xinming Li, Li Tao, Zefeng Chen, Hui Fang, Xuesong Li, Xinran Wang, Jian-Bin Xu, and Hongwei Zhu. Graphene and related two-dimensional materials: Structure-property relationships for electronics and optoelectronics. *Applied Physics Reviews*, 4(2):021306, 2017.

[23] K S Novoselov, A Mishchenko, A Carvalho, and A H Castro Neto. 2D materials and van der Waals heterostructures. *Science*, 353(6298):aac9439, 2016.

[24] Pavel B Sorokin and Boris I Yakobson. Two-dimensional diamond-diamane: current state and further prospects. *Nano Letters*, 21(13):5475–5484, 2021.

[25] Seymur Cahangirov, Mehmet Topsakal, Ethem Aktürk, Hasan Şahin, and Salim Ciraci. Two- and one-dimensional honeycomb structures of silicon and germanium. *Physical Review Letters*, 102(23):236804, 2009.

[26] Joelson C Garcia, Denille B De Lima, Lucy V C Assali, and João F Justo. Group IV graphene-and graphane-like nanosheets. *The Journal of Physical Chemistry C*, 115(27):13242–13246, 2011.

[27] Leslie M Schoop, Florian Pielnhofer, and Bettina V Lotsch. Chemical principles of topological semimetals. *Chemistry of Materials*, 30(10):3155–3176, 2018.

[28] Bruno Ipaves, João F Justo, and Lucy V C Assali. Functionalized few-layer silicene nanosheets: stability, elastic, structural, and electronic properties. *Physical Chemistry Chemical Physics*, 24(15):8705–8715, 2022.

[29] Yongling An, Yuan Tian, Chuanliang Wei, Yuchan Zhang, Shenglin Xiong, Jinkui Feng, and Yitai Qian. Recent advances and perspectives of 2D silicon: synthesis and application for energy storage and conversion. *Energy Storage Materials*, 32:115–150, 2020.

[30] Bruno Ipaves, João F Justo, and Lucy V C Assali. Aluminum functionalized few-layer silicene as anode material for alkali metal ion batteries. *Molecular Systems Design & Engineering*, 8(3):379–387, 2023.

[31] Georgios A Tritsaris, Efthimios Kaxiras, Sheng Meng, and Enge Wang. Adsorption and diffusion of lithium on layered silicon for li-ion storage. *Nano Letters*, 13(5):2258–2263, 2013.

[32] Jiajie Zhu and Udo Schwingenschlögl. Silicene for Na-ion battery applications. *2D Materials*, 3(3):035012, 2016.

[33] Jingjing Liu, Yang Yang, Pengbo Lyu, Petr Nachtigall, and Yuxi Xu. Few-layer silicene nanosheets with superior lithium-storage properties. *Advanced Materials*, 30(26):1800838, 2018.

[34] Yuanhe Sun, Yuanxin Zhao, Zhaofeng Liang, Han Lin, Zhiguo Ren, Zeying Yao, Yaru Yin, Ping Huai, Ke Yang, Jinyou Lin, et al. Reversible potassium-ion alloying storage in crystalline silicene. *Chemical Engineering Journal*, 435:134961, 2022.

[35] Tie Lei Shao, Chunyi Liu, Wenjun Deng, Chang Li, Xusheng Wang, Mianqi Xue, and Rui Li. Recent research on strategies to improve ion conduction in alkali metal-ion batteries. *Batteries & Supercaps*, 2(5):403–427, 2019.

[36] Erlong Gu, Jingyi Xu, Yichen Du, Xufang Ge, Xiaoshu Zhu, Jianchun Bao, and Xiaosi Zhou. Understanding the influence of different carbon matrix on the electrochemical performance of $Na_3V_2(PO_4)_3$ cathode for sodium-ion batteries. *Journal of Alloys and Compounds*, 788:240–247, 2019.

[37] David S Sholl and Janice A Steckel. *Density functional theory: a practical introduction*. John Wiley & Sons, 2011.

[38] M Born and R Oppenheimer. Zur quantentheorie der molekeln. *Annalen der Physik*, pages 457–484, 1927.

[39] Pierre Hohenberg and Walter Kohn. Inhomogeneous electron gas. *Physical Review*, 136(3B):B864, 1964.

[40] Walter Kohn and Lu Jeu Sham. Self-consistent equations including exchange and correlation effects. *Physical Review*, 140(4A):A1133, 1965.

[41] John P Perdew, Kieron Burke, and Matthias Ernzerhof. Generalized gradient approximation made simple. *Physical Review Letters*, 77(18):3865, 1996.

[42] Max Dion, Henrik Rydberg, Elsebeth Schröder, David C Langreth, and Bengt I Lundqvist. Van der Waals density functional for general geometries. *Physical Review Letters*, 92(24):246401, 2004.

[43] Jiří Klimeš, David R Bowler, and Angelos Michaelides. Chemical accuracy for the van der Waals density functional. *Journal of Physics: Condensed Matter*, 22(2):022201, 2009.

[44] Jochen Heyd, Gustavo E Scuseria, and Matthias Ernzerhof. Hybrid functionals based on a screened coulomb potential. *The Journal of Chemical Physics*, 118(18):8207–8215, 2003.

[45] Fabien Tran, Leila Kalantari, Boubacar Traoré, Xavier Rocquefelte, and Peter Blaha. Nonlocal van der Waals functionals for solids: choosing an appropriate one. *Physical Review Materials*, 3(6):063602, 2019.

[46] Axel D Becke. Density-functional exchange-energy approximation with correct asymptotic behavior. *Physical Review A*, 38(6):3098, 1988.

[47] Jiří Klimeš, David R Bowler, and Angelos Michaelides. Van der Waals density functionals applied to solids. *Physical Review B*, 83(19):195131, 2011.

[48] Aliaksandr V Krukau, Oleg A Vydrov, Artur F Izmaylov, and Gustavo E Scuseria. Influence of the exchange screening parameter on the performance of screened hybrid functionals. *The Journal of Chemical Physics*, 125(22):224106, 2006.

[49] Peter E Blöchl. Projector augmented-wave method. *Physical Review B*, 50(24):17953, 1994.

[50] David Vanderbilt. Soft self-consistent pseudopotentials in a generalized eigenvalue formalism. *Physical Review B*, 41(11):7892, 1990.

[51] David J Singh and Lars Nordstrom. *Planewaves, Pseudopotentials, and the LAPW method*. Springer Science & Business Media, 2006.

[52] Georg Kresse and Daniel Joubert. From ultrasoft pseudopotentials to the projector augmented-wave method. *Physical Review B*, 59(3):1758, 1999.

[53] Peter E Blöchl, Clemens J Först, and Johannes Schimpl. Projector augmented wave method: ab initio molecular dynamics with full wave functions. *Bulletin of Materials Science*, 26(1):33–41, 2003.

[54] Paolo Giannozzi, Stefano De Gironcoli, Pasquale Pavone, and Stefano Baroni. Ab initio calculation of phonon dispersions in semiconductors. *Physical Review B*, 43(9):7231, 1991.

[55] Stefano Baroni, Stefano De Gironcoli, Andrea Dal Corso, and Paolo Giannozzi. Phonons and related crystal properties from density-functional perturbation theory. *Reviews of Modern Physics*, 73(2):515, 2001.

[56] Nicolas Mounet and Nicola Marzari. First-principles determination of the structural, vibrational and thermodynamic properties of diamond, graphite, and derivatives. *Physical Review B*, 71(20):205214, 2005.

[57] Emiliano Cadelano, Pier Luca Palla, Stefano Giordano, and Luciano Colombo. Elastic properties of hydrogenated graphene. *Physical Review B*, 82(23):235414, 2010.

[58] Félix Mouhat and François-Xavier Coudert. Necessary and sufficient elastic stability conditions in various crystal systems. *Physical Review B*, 90(22):224104, 2014.

[59] Bruno Bueno Ipaves Nascimento. Theoretical investigation of grephene-like nanostructures for application in lithium ion batteries. Master's thesis, University of Sao Paulo, 2018.

[60] Sten Haastrup, Mikkel Strange, Mohnish Pandey, Thorsten Deilmann, Per S Schmidt, Nicki F Hinsche, Morten N Gjerding, Daniele Torelli, Peter M Larsen, Anders C Riis-Jensen, and *et al.* The computational 2D materials database:

high-throughput modeling and discovery of atomically thin crystals. *2D Materials*, 5(4):042002, 2018.

[61] M N Gjerding, A Taghizadeh, A Rasmussen, S Ali, F Bertoldo, T Deilmann, UP Holguin, NR Knøsgaard, M Kruse, S Manti, and *et al.* Recent progress of the computational 2D materials database (C2DB). *2D Materials*, 8(4):044002, 2021.

[62] Daan Frenkel and Berend Smit. *Understanding molecular simulation: from algorithms to applications*, volume 1. Elsevier, 2001.

[63] Michael P Allen and Dominic J Tildesley. *Computer simulation of liquids.* Oxford University Press, 2017.

[64] Georg Kresse and Jürgen Furthmüller. Efficient iterative schemes for ab initio total-energy calculations using a plane-wave basis set. *Physical Review B*, 54(16):11169, 1996.

[65] Shuichi Nosé. A unified formulation of the constant temperature molecular dynamics methods. *The Journal of Chemical Physics*, 81(1):511–519, 1984.

[66] Nosé Shuichi. Constant temperature molecular dynamics methods. *Progress of Theoretical Physics Supplement*, 103:1–46, 1991.

[67] William G Hoover. Canonical dynamics: Equilibrium phase-space distributions. *Physical Review A*, 31(3):1695, 1985.

[68] Qiu He, Bin Yu, Zhaohuai Li, and Yan Zhao. Density functional theory for battery materials. *Energy & Environmental Materials*, 2(4):264–279, 2019.

[69] Anton Van der Ven, Zhi Deng, Swastika Banerjee, and Shyue Ping Ong. Rechargeable alkali-ion battery materials: theory and computation. *Chemical Reviews*, 120(14):6977–7019, 2020.

[70] Graeme Henkelman, Gísli Jóhannesson, and Hannes Jónsson. Methods for finding saddle points and minimum energy paths. In *Theoretical Methods in Condensed Phase Chemistry*, pages 269–302. Springer, 2002.

[71] Daniel Sheppard, Rye Terrell, and Graeme Henkelman. Optimization methods for finding minimum energy paths. *The Journal of Chemical Physics*, 128(13):134106, 2008.

[72] Paolo Giannozzi, Stefano Baroni, Nicola Bonini, Matteo Calandra, Roberto Car, Carlo Cavazzoni, Davide Ceresoli, Guido L Chiarotti, Matteo Cococcioni, Ismaila Dabo, et al. Quantum espresso: a modular and open-source software project for quantum simulations of materials. *Journal of Physics: Condensed Matter*, 21(39):395502, 2009.

[73] Paolo Giannozzi, Oliviero Andreussi, Thomas Brumme, Oana Bunau, M Buongiorno Nardelli, Matteo Calandra, Roberto Car, Carlo Cavazzoni, Davide Ceresoli, Matteo Cococcioni, et al. Advanced capabilities for materials modelling with quantum espresso. *Journal of Physics: Condensed Matter*, 29(46):465901, 2017.

[74] Graeme Henkelman, Andri Arnaldsson, and Hannes Jónsson. A fast and robust algorithm for bader decomposition of charge density. *Computational Materials Science*, 36(3):354–360, 2006.

[75] Edward Sanville, Steven D Kenny, Roger Smith, and Graeme Henkelman. Improved grid-based algorithm for bader charge allocation. *Journal of Computational Chemistry*, 28(5):899–908, 2007.

[76] W Tang, E Sanville, and G Henkelman. A grid-based bader analysis algorithm without lattice bias. *Journal of Physics: Condensed Matter*, 21(8):084204, 2009.

[77] Min Yu and Dallas R Trinkle. Accurate and efficient algorithm for bader charge integration. *The Journal of Chemical Physics*, 134(6):064111, 2011.

[78] Hendrik J Monkhorst and James D Pack. Special points for brillouin-zone integrations. *Physical Review B*, 13(12):5188, 1976.

[79] Guowen Qin, Lailei Wu, and Huiyang Gou. Diamane: design, synthesis, properties, and challenges. *Functional Diamond*, 1(1):83–92, 2021.

[80] Zhiming Shi, Alex Kutana, and Boris I Yakobson. How much N-doping can graphene sustain? *Journal of Physical Chemistry Letters*, 6(1):106–112, 2015.

[81] Jian Zhou, Qiang Sun, Qian Wang, and Puru Jena. High-temperature superconductivity in heavily N- or B-doped graphene. *Physical Review B*, 92(6):064505, 2015.

[82] Nicolas Mounet and Nicola Marzari. First-principles determination of the structural, vibrational and thermodynamic properties of diamond, graphite, and derivatives. *Physical Review B*, 71(20):205214, 2005.

[83] M Mohr, J Maultzsch, E Dobardžić, S Reich, I Milošević, M Damnjanović, A Bosak, M Krisch, and C Thomsen. Phonon dispersion of graphite by inelastic x-ray scattering. *Physical Review B*, 76(3):035439, 2007.

[84] Sergey V Bondarchuk and Boris F Minaev. Two isomeric solid carbon nitrides with 1:1 stoichiometry which exhibit strong mechanical anisotropy. *New Journal of Chemistry*, 41(21):13140–13148, 2017.

[85] Hyung Mo Jeong, Jung Woo Lee, Weon Ho Shin, Yoon Jeong Choi, Hyun Joon Shin, Jeung Ku Kang, and Jang Wook Choi. Nitrogen-doped graphene for high-performance ultracapacitors and the importance of nitrogen-doped sites at basal planes. *Nano Letters*, 11(6):2472–2477, 2011.

[86] Xinran Wang, Xiaolin Li, Li Zhang, Youngki Yoon, Peter K Weber, Hailiang Wang, Jing Guo, and Hongjie Dai. N-doping of graphene through electrothermal reactions with ammonia. *Science*, 324(5928):768–771, 2009.

[87] Ziwei Tang, Xiaowei Chen, Hao Chen, Limin Wu, and Xuebin Yu. Metal-free catalysis of ammonia–borane dehydrogenation/regeneration for a highly efficient and facilely recyclable hydrogen-storage material. *Angewandte Chemie International Edition*, 52(22):5832–5835, 2013.

[88] Yongsheng Fu, Junwu Zhu, Chong Hu, Xiaodong Wu, and Xin Wang. Covalently coupled hybrid of graphitic carbon nitride with reduced graphene oxide as a superior performance lithium-ion battery anode. *Nanoscale*, 6(21):12555–12564, 2014.

[89] Arava Leela Mohana Reddy, Anchal Srivastava, Sanketh R Gowda, Hemtej Gullapalli, Madan Dubey, and Pulickel M Ajayan. Synthesis of nitrogen-doped graphene films for lithium battery application. *ACS Nano*, 4(11):6337–6342, 2010.

[90] Tore Brinck, Jane S Murray, and Peter Politzer. A computational analysis of the bonding in boron trifluoride and boron trichloride and their complexes with ammonia. *Inorganic Chemistry*, 32(12):2622–2625, 1993.

[91] Joelson C Garcia, João F Justo, Wanda V M Machado, and Lucy V C Assali. Functionalized adamantane: building blocks for nanostructure self-assembly. *Physical Review B*, 80(12):125421, 2009.

[92] M Grimsditch, E S Zouboulis, and A Polian. Elastic constants of boron nitride. *Journal of Applied Physics*, 76(2):832–834, 1994.

[93] Francis Birch. Finite elastic strain of cubic crystals. *Physical Review*, 71(11):809, 1947.

[94] Teerachote Pakornchote, Annop Ektarawong, Björn Alling, Udomsilp Pinsook, Somchai Tancharakorn, Wutthikrai Busayaporn, and Thiti Bovornratanaraks. Phase stabilities and vibrational analysis of hydrogenated diamondized bilayer graphenes: A first principles investigation. *Carbon*, 146:468–475, 2019.

[95] Feng Ke, Lingkong Zhang, Yabin Chen, Ketao Yin, Chenxu Wang, Yan-Kai Tzeng, Yu Lin, Hongliang Dong, Zhenxian Liu, John S Tse, et al. Synthesis of atomically thin hexagonal diamond with compression. *Nano Letters*, 20(8):5916–5921, 2020.

[96] Ting Cheng, Zhongfan Liu, and Zhirong Liu. High elastic moduli, controllable bandgap and extraordinary carrier mobility in single-layer diamond. *Journal of Materials Chemistry C*, 8(39):13819–13826, 2020.

[97] T Pakornchote, A Ektarawong, W Busayaporn, U Pinsook, and T Bovornrata-naraks. Roles of nitrogen substitution and surface reconstruction in stabilizing nonpassivated single-layer diamond. *Physical Review B*, 102(7):075418, 2020.

[98] Changgu Lee, Xiaoding Wei, Jeffrey W Kysar, and James Hone. Measurement of the elastic properties and intrinsic strength of monolayer graphene. *Science*, 321(5887):385–388, 2008.

[99] Leonid A Chernozatonskii, Pavel B Sorokin, Alexander A Kuzubov, Boris P Sorokin, Alexander G Kvashnin, Dmitry G Kvashnin, Pavel V Avramov, and Boris I Yakobson. Influence of size effect on the electronic and elastic properties of diamond films with nanometer thickness. *The Journal of Physical Chemistry C*, 115(1):132–136, 2011.

[100] H Gercek. Poisson's ratio values for rocks. *International Journal of Rock Mechanics and Mining Sciences*, 44(1):1–13, 2007.

[101] Peter Hess. Bonding, structure, and mechanical stability of 2D materials: the predictive power of the periodic table. *Nanoscale Horizons*, 6:856–892, 2021.

[102] Yang Liu, Haibo Shu, Pei Liang, Dan Cao, Xiaoshuang Chen, and Wei Lu. Structural, electronic, and optical properties of hydrogenated few-layer silicene: size and stacking effects. *Journal of Applied Physics*, 114(9):094308, 2013.

[103] Y F Li, G H Tang, and B Fu. Hydrogenation: an effective strategy to improve the thermoelectric properties of multilayer silicene. *Physical Review B*, 99(23):235428, 2019.

[104] Yi Ding and Yanli Wang. Density functional theory study of the silicene-like SiX and XSi$_3$ (X= B, C, N, Al, P) honeycomb lattices: the various buckled structures and versatile electronic properties. *The Journal of Physical Chemistry C*, 117(35):18266–18278, 2013.

[105] Michael Ashton, Susan B Sinnott, and Richard G Hennig. Computational discovery and characterization of polymorphic two-dimensional IV–V materials. *Applied Physics Letters*, 109(19):192103, 2016.

[106] Benjamin C Revard, William W Tipton, Anna Yesypenko, and Richard G Hennig. Grand-canonical evolutionary algorithm for the prediction of two-dimensional materials. *Physical Review B*, 93(5):054117, 2016.

[107] Shoeib Babaee Touski and Nayereh Ghobadi. Structural, electrical, and rashba properties of monolayer janus Si$_2$XY (X, Y= P, As, Sb, and Bi). *Physical Review B*, 103(16):165404, 2021.

[108] Mohammad Ali Mohebpour, Shobair Mohammadi Mozvashi, Sahar Izadi Vishkayi, and Meysam Bagheri Tagani. Prediction of hydrogenated group IV–V hexagonal binary monolayers. *Scientific Reports*, 10(1):1–14, 2020.

[109] Baolin Wang, Jiangtao Wu, Xiaokun Gu, Hanqing Yin, Yujie Wei, Ronggui Yang, and Mildred Dresselhaus. Stable planar single-layer hexagonal silicene under tensile strain and its anomalous poisson's ratio. *Applied Physics Letters*, 104(8):081902, 2014.

[110] D K Das and Jit Sarkar. Comparison of mechanical properties of silicene estimated using different testing procedures: a molecular dynamics study. *Journal of Applied Physics*, 123(4):044304, 2018.

[111] Chen Qian and Zhi Li. Multilayer silicene: structure, electronics, and mechanical property. *Computational Materials Science*, 172:109354, 2020.

[112] Jose E Padilha and Renato B Pontes. Free-standing bilayer silicene: the effect of stacking order on the structural, electronic, and transport properties. *The Journal of Physical Chemistry C*, 119(7):3818–3825, 2015.

[113] Huixia Fu, Jin Zhang, Zijing Ding, Hui Li, and Sheng Meng. Stacking-dependent electronic structure of bilayer silicene. *Applied Physics Letters*, 104(13):131904, 2014.

[114] Burak Özdamar, Gözde Özbal, M Neşet Çınar, Koray Sevim, Gizem Kurt, Birnur Kaya, and Hâldun Sevinçli. Structural, vibrational, and electronic properties of single-layer hexagonal crystals of group IV and V elements. *Physical Review B*, 98(4):045431, 2018.

[115] J M Pacheco, G K Gueorguiev, and José Luís Martins. First-principles study of the possibility of condensed phases of endohedral silicon cage clusters. *Physical Review B*, 66(3):033401, 2002.

[116] G K Gueorguiev and J M Pacheco. Silicon and metal nanotemplates: Size and species dependence of structural and electronic properties. *The Journal of Chemical Physics*, 119(19):10313–10317, 2003.

[117] Radha Somaiya, Deobrat Singh, Yogesh Kumar Sonvane, Sanjeev Kumar Gupta, and Rajeev Ahuja. Potential SiX (X= N, P, As, Sb, Bi) homo-bilayers for visible-light photocatalysts application. *Catalysis Science & Technology*, 11:4996–5013, 2021.

[118] Radha N Somaiya, Yogesh Ashokbhai Sonvane, and Sanjeev K Gupta. Exploration of the strain and thermoelectric properties of hexagonal SiX (X= N, P, As, Sb, and Bi) monolayers. *Physical Chemistry Chemical Physics*, 22(7):3990–3998, 2020.

[119] Jincheng Zhuang, Xun Xu, Germanas Peleckis, Weichang Hao, Shi Xue Dou, and Yi Du. Silicene: a promising anode for lithium-ion batteries. *Advanced Materials*, 29(48):1606716, 2017.

[120] Jiajie Zhu, Appala Naidu Gandi, and Udo Schwingenschlögl. Potential of B/Al-doped silicene electrodes in Na/K-ion batteries. *Advanced Theory and Simulations*, 1(7):1800017, 2018.

[121] Chengzhi Zhang, Fei Wang, Jian Han, Shuo Bai, Jun Tan, Jinshui Liu, and Feng Li. Challenges and recent progress on silicon-based anode materials for next-generation lithium-ion batteries. *Small Structures*, 6(2):2170015, 2021.

[122] Yanning Wang and Yinshi Li. Ab initio prediction of two-dimensional Si_3C enabling high specific capacity as an anode material for Li/Na/K-ion batteries. *Journal of Materials Chemistry A*, 8(8):4274–4282, 2020.

[123] Bohayra Mortazavi, Arezoo Dianat, Gianaurelio Cuniberti, and Timon Rabczuk. Application of silicene, germanene and stanene for Na or Li ion storage: a theoretical investigation. *Electrochimica Acta*, 213:865–870, 2016.

[124] Svante Arrhenius. Über die dissociationswärme und den einfluss der temperatur auf den dissociationsgrad der elektrolyte. *Zeitschrift für Physikalische Chemie*, 4(1):96–116, 1889.

[125] Vivekanand Shukla, Rafael B Araujo, Naresh K Jena, and Rajeev Ahuja. The curious case of two dimensional Si_2BN: a high-capacity battery anode material. *Nano Energy*, 41:251–260, 2017.

[126] Kristin Persson, Yoyo Hinuma, Ying Shirley Meng, Anton Van der Ven, and Gerbrand Ceder. Thermodynamic and kinetic properties of the Li-graphite system from first-principles calculations. *Physical Review B*, 82(12):125416, 2010.

[127] Yu Jing, Zhen Zhou, Carlos R Cabrera, and Zhongfang Chen. Metallic VS_2 monolayer: a promising 2D anode material for lithium ion batteries. *The Journal of Physical Chemistry C*, 117(48):25409–25413, 2013.

[128] Sten Lunell, Arvids Stashans, Lars Ojamäe, Henrik Lindström, and Anders Hagfeldt. Li and Na diffusion in TiO_2 from quantum chemical theory versus electrochemical experiment. *Journal of the American Chemical Society*, 119(31):7374–7380, 1997.

[129] Henrik Lindström, Sven Södergren, Anita Solbrand, Håkan Rensmo, Johan Hjelm, Anders Hagfeldt, and Sten-Eric Lindquist. Li+ ion insertion in TiO_2 (anatase). 1. Chronoamperometry on CVD films and nanoporous films. *The Journal of Physical Chemistry B*, 101(39):7710–7716, 1997.

[130] Carol L Olson, Jenny Nelson, and M Saiful Islam. Defect chemistry, surface structures, and lithium insertion in anatase TiO_2. *The Journal of Physical Chemistry B*, 110(20):9995–10001, 2006.

[131] Hasan Sahin and Francois M Peeters. Adsorption of alkali, alkaline-earth, and 3d transition metal atoms on silicene. *Physical Review B*, 87(8):085423, 2013.

[132] Darwin Barayang Putungan, Shi-Hsin Lin, and Jer-Lai Kuo. Metallic VS_2 monolayer polytypes as potential sodium-ion battery anode via ab initio random structure searching. *ACS Applied Materials & Interfaces*, 8(29):18754–18762, 2016.

[133] H R Jiang, Wei Shyy, Ming Liu, Lei Wei, M C Wu, and T S Zhao. Boron phosphide monolayer as a potential anode material for alkali metal-based batteries. *Journal of Materials Chemistry A*, 5(2):672–679, 2017.